# Multifunctional optical surfaces for optoelectronic devices

## Juan Rombaut Segarra

# Multifunctional optical surfaces for optoelectronic devices

JUAN ROMBAUT SEGARRA

Thesis advisor: Prof. Valerio Pruneri

PhD Thesis - 2022

*A mi Familia.*

# Abstract

Highly transparent optical surfaces with anti-reflection (AR) and self-cleaning properties have the potential to increase performance in a wide range of applications, such as display screens, photovoltaic cells and sensors, among others. Nature has provided numerous examples of biological systems with interesting functionalities that have high commercial interest, from the broadband and omnidirectional anti-reflection effect created by the tiny nanopillars found on the corneas of moths' eyes, to the self-cleaning behaviour of lotus leaves generated by micro-and nanoprotuberances. However, despite intense academic research, replicating such elaborate nanostructures for mass-production remains a major challenge due to the limitations of the existing nanofabrication techniques based on classical optical and e-beam lithography processes.

This thesis is devoted to the study of bio-inspired multifunctional nanostructured surfaces with enhanced optical and wetting properties for use in optoelectronic devices. Novel and reliable manufacturing techniques are proposed for patterning organic and inorganic materials with high precision and throughput, aiming to bring this technology out of the laboratory and making it industrially viable.

The first part of this study has been centred on glass, as it is one of the most widely used materials for optoelectronic devices, such as display screens, solar panel protections, fenestration and optics. Chapter 3 presents a nanopillar structure created on glass substrates, which provides high anti-reflective properties, enhanced transmission, low scattering, superhydrophobicity, and high mechanical resistance against external agents. The proposed manufacturing method permits moderate tunability to adapt the structure to the requirements of different applications. The design and optimisation of the fabrication process and a full characterisation of the samples are reported.

Chapter 4 describes, for the first time, the combination of two different anti-reflective approaches, state-of-the-art multilayer (ML) anti-reflective coatings and self-cleaning biomimetic nanostructures (NS). The classical ML coating, relying on destructive interference from multiple reflections at layer interfaces

is capable of providing excellent AR properties, but with a limited wavelength range and angular acceptance. In addition, it has limited hydrophobicity and self-cleaning properties due to its flat surface. The NS coating can provide broad wavelength and angular AR properties, as well as superhydrophobicity. However, it suffers from mechanical durability issues. In this work, the combination of both methods is presented as an innovative solution, combining greater anti-reflective operational wavelength and angular acceptance, self-cleaning properties, and high mechanical durability.

A nanostructured design for transparent oleophobic surfaces is investigated and experimentally demonstrated in Chapter 5. Two new fabrication techniques to create nanocavities on glass are presented. The nanohole structure can repel oil and other low surface tension liquids, and a new wetting model is developed to theoretically explain the mechanism. The porous structure modifies the effective refractive index of the nanostructured layer between the air and the glass, creating an AR effect. The samples present higher transmission, as well as low scattering due to the subwavelength size of the cavities. In addition, the geometry of the surface offers higher mechanical resistance compared to nanopillars, widening the potential applications where it could be used.

Finally, in Chapter 6, a new method to nanostructure organic materials with high resolution is presented. Nanostructured thin polyimide films on top of glass surfaces can act as an anti-reflective coating, while adding protection and hydrophobicity. A practical example is demonstrated with transparent electrodes made of Indium Tin Oxide. By covering a surface with nanostructured polyimide, the overall optical response can be improved while its electric properties are protected by the polymeric film.

In summary, this thesis demonstrates some of the potential applications of multifunctional optical surfaces based on bio-inspired subwavelength nanostructures, as well as different methods to fabricate them with faster, cheaper, and scalable manufacturing methods.

# Resumen

Las superficies ópticas altamente transparentes con propiedades antirreflectantes (AR) y autolimpiantes tienen el potencial de aumentar el rendimiento de una amplia gama de aplicaciones, como pantallas de dispositivos móviles, células fotovoltaicas y sensores, entre otras. La naturaleza ha proporcionado numerosos ejemplos de sistemas biológicos con fascinantes funcionalidades que tienen un alto interés comercial, desde el efecto antirreflejante omnidireccional y de banda ancha creado por los diminutos nanopilares que se encuentran en las córneas de los ojos de las polillas, hasta el comportamiento de autolimpieza de las hojas de loto generadas por micro- y nanoprotuberancias. Sin embargo, a pesar de la intensa investigación académica, la replicación de nanoestructuras para la producción en masa sigue siendo un desafío importante debido a las limitaciones de las técnicas de nanofabricación existentes basadas en los procesos clásicos de litografía óptica y de haz electrónico.

Esta tesis está dedicada al estudio de superficies nanoestructuradas multifuncionales bioinspiradas con propiedades ópticas y humectantes mejoradas para su uso en dispositivos optoelectrónicos. Se proponen técnicas de fabricación novedosas y escalables para modelar materiales orgánicos e inorgánicos con alta precisión y rendimiento, con el objetivo de sacar esta tecnología del laboratorio y hacerla viable industrialmente.

La primera parte de este estudio se ha centrado en el vidrio, ya que es uno de los materiales más utilizados para dispositivos optoelectrónicos como pantallas, protecciones de paneles solares y lentes ópticas. El Capítulo 3 presenta una estructura nanopilar creada sobre sustratos de vidrio que proporciona altas propiedades antirreflectantes, transmisión mejorada, alta claridad, superhidrofobicidad y alta resistencia mecánica frente a agentes externos. El método de fabricación propuesto permite un ajuste moderado para adaptar la estructura a los requisitos de diferentes aplicaciones. Se expone el diseño y optimización del proceso de fabricación y una caracterización completa de las muestras.

El Capítulo 4 describe, por primera vez, la combinación de dos tecnologías antirreflectantes diferentes, recubrimientos antirreflectantes multicapa (MC) de última generación y nanoestructuras biomiméticas (NS) autolimpiantes. El recubrimiento MC clásico, que se basa en la interferencia destructiva de múltiples reflexiones en las interfaces de las capas, es capaz de proporcionar excelentes propiedades AR, pero con un rango óptimo de longitud de onda y un ángulo de incidencia limitados. Además, tiene propiedades de hidrofobicidad y autolimpieza limitadas debido a su superficie plana. El recubrimiento NS puede proporcionar propiedades AR de longitud de onda amplia y buena respuesta angular, así como superhidrofobicidad. Sin embargo, sufre problemas de durabilidad mecánica. En este trabajo, la combinación de ambos métodos se presenta como una solución innovadora, que combina mayor longitud de onda operativa antirreflectante y aceptación angular, propiedades de autolimpieza y alta durabilidad mecánica.

En el Capítulo 5 se investiga y se demuestra experimentalmente un diseño nanoestructurado para superficies oleofóbicas transparentes. Se presentan dos nuevas técnicas de fabricación para crear nanocavidades en vidrio. La estructura del nanoagujero puede repeler el aceite y otros líquidos de baja tensión superficial, y se desarrolla un nuevo modelo de humectación para explicar teóricamente el mecanismo. La estructura porosa modifica el índice de refracción efectivo de la capa nanoestructurada entre el aire y el vidrio, creando un efecto AR. Las muestras presentan mayor transmisión, así como baja dispersión debido al tener nanocavidades de un tamaño inferior a la longitud de onda incidente. Además, la geometría de la superficie ofrece una mayor resistencia mecánica en comparación con los nanopilares, lo que amplía las posibles aplicaciones donde podría utilizarse.

Finalmente, en el Capítulo 6, se presenta un nuevo método para nanoestructurar materiales orgánicos con alta resolución. Las películas delgadas de poliimida nanoestructuradas en la parte superior de las superficies de vidrio pueden actuar como un revestimiento antirreflectante, al tiempo que agregan protección e hidrofobicidad. Un ejemplo práctico se demuestra con electrodos transparentes hechos de óxido de indio y estaño. Al cubrir una superficie con poliimida nanoestructurada, la respuesta óptica general puede mejorarse mientras sus propiedades eléctricas están protegidas por la película polimérica.

En resumen, esta tesis demuestra algunas de las posibles aplicaciones de superficies ópticas multifuncionales bioinspiradas y de tamaño nanométrico, así como diferentes métodos para fabricarlas con métodos de fabricación más rápidos, económicos y escalables.

x

# Acknowledgments

In this section I would like to thank all the people who contributed in some way to the work described in this thesis.

First of all, I would like to express my most sincere gratitude to Dr. Pere Mir Puig, for his continuous guidance and support during my academic career and for encouraging me to do the PhD at ICFO. I really miss our long conversations and the physics and engineering challenges you were posing me together with my father at your place, they were truly inspiring and fun.  I would have loved to give you a copy of this thesis.

I also want to thank Mr. Jordi Segarra, Prof. Lluís Torner, Fundació Mir-Puig, Fundació Cellex and ICFO for granting me this incredible opportunity and their continuous support during the last years. I am extremely grateful to have worked at ICFO during the PhD and without any doubt this experience has changed my live professionally and personally.

I would like to say special thanks to my thesis supervisor Prof. Valerio Pruneri for giving me the chance to do the PhD in the Optoelectronics group and in this particular project, that completely fitted my interests. I really appreciate his guidance, support, and great ideas during the course of this thesis and all I have learnt from him.  Also, thanks to Prantik Mazumder, for the helpful collaboration in all the works we published together and in the correction of this thesis. Thanks for all your advices and for being so accessible.

During the last 5 years I have met great professionals at ICFO, but some of them have become great friends or my second family, and I would like to dedicate some words to them.

Vittoria, la *mia mamma* or my non-official postdoc. Definitely the person who has helped me the most with all my experiments. Thank you for everything you have taught me, for helping me, for taking care of me, but on top of that, thanks for your patience.  We have laughed a lot together during all this time and I really appreciate your help. Thanks for being a bright and solar person….

Juan Miguel, my brother from another mother. It has been a pleasure to share the office 270 with you and build this great friendship we have now. Thanks for all the great moments, your professional and personal advices, our beers together and your loud business calls, I miss them.

Marchena, another pillar for me at ICFO. Although you never introduced me properly to the OPTO group… I really appreciate all your support during my stay at ICFO. Thanks for your sense of humour and to make our hours in the lab more enjoyable, we had great and very funny moments!

Rubaiya, my gossip partner, the Khaleesi of the office. Thanks for all the interesting conversations we had…, it's been a pleasure to share this journey with you. Anita, my favourite chemist. Thanks for your patience solving all my doubts, our gym sessions, and your friendship. Seba, thanks for your permanent smile and good mood! and mis cubanitos Noslen and Alberto, we have spent a lot of time together and I really enjoyed every party/adventure with you.

Regarding my research group, the OPTO-family, I would like to thank all the people I have met during this period that at some point contributed to make my stay at ICFO even better.

First, my office mates not yet mentioned. Dani, my beloved hater, Tor, my crazy dancer, and Javi, the newest member, I have great memories working with you in the office and in all the labs we have shared. Miquel and Vahagn, my first office mates, thanks for all your help at the beginning of this journey and for all your advices. Also, my students Manu, Asier, Umberto and Goretti, thanks for all your help and contribution. Thanks to the Surfaces team, with Bruno, Ana, Rinu, Nestor, Rafaël, Christina and Dani, the LIM team with Roland, Luc, Sebastian and Alex, the Sixsenso team with Marc and now Alfredo and David, and the Quantum team… I don't really know what you are doing but I enjoyed really good moments in the cafeteria with you.

I would also like to thank all the ICFO team that contributed and helped me to develop my work. Starting with the NFL staff, for doing a great job keeping all our instruments working in perfect conditions and for all their help and support. Alastair from KTT, for his contribution with the patents and helping

us collaborating with different companies, and the rest of departments, purchasing, maintenance, logistics…

Finally, I would like to acknowledge a very special person for her unmeasurable support and love. Thanks, Sofía, for always motivating me and pushing me forward towards my goals.

Por último, a mi familia. Gracias a mis padres y mi hermana por su apoyo, ayuda y amor incondicional. Por haber hecho todo lo que estaba en sus manos para darme la mejor formación y motivarme siempre para desarrollar de la mejor manera mi carrera profesional. Esta tesis va dedicada a ellos.

# List of Publications

**Journal Papers**

- **J. Rombaut**, R.A. Maniyara, R.A. Bellman, D.F. Acquard, A.D. Baca, J. Osmond, W. Senaratne, M.A. Quesada, D. Baker, P. Mazumder, V. Pruneri. "Antireflective Transparent Oleophobic Surfaces by Noninteracting Cavities". *ACS Appl. Mater. Interfaces 2018, 10, 49, 43230-43235*.

- **J. Rombaut**, M. Fernandez, P. Mazumder, V. Pruneri. "Nanostructured Hybrid-Material Transparent Surface with Antireflection Properties and a Facile Fabrication Process". *ACS Omega 2019, 4, 22, 19840-19846.*

- **J. Rombaut**, S. Martínez, U.M. Matera, P. Mazumder, V. Pruneri. "Antireflective Multilayer Surface with Self-Cleaning Subwavelength Structures". *ACS Photonics 2021, 8, 3, 894-900.*

**Patents**

- **J. Rombat**, P. Mazumder, V. Pruneri. "ANTI-REFLECTIVE TRANSPARENT OLEOPHOBIC SURFACES AND METHODS OF MANUFACTURING THEREOF". WO2020210079A1 (2020)

- **J. Rombaut**, P. Mazumder, V. Pruneri. "ANTI-REFLECTIVE MULTILAYER SURFACE WITH SELF-CLEANING SUBWAVELENGTH STRUCTURES" (submitted 2021)

**Conference contributions**

Talks

- **J. Rombaut**, B. Paulillo, N. Bareza, D. Martinez, R. Maniyara, K.K. Gopalan, P. Mazumder, V. Pruneri. "Multifunctional nanostructured optical surfaces for industrial applications". Materials Research Society Fall Meeting 2019.

Posters

- **J. Rombaut**, P. Mazumder, V. Finazzi, V. Pruneri. "Omnidirectional antireflection biomimetic surfaces for display screens". 5th International Conference on Multifunctional, Hybrid and Nanomaterials, Lisbon, Portugal 2017

- O. Txoperena, A. Centeno, **J. Rombaut**, V. Pruneri. "Graphene for flexible and transparent conductive electrodes" Graphene Week 2017

Other relevant contributions

- B. Paulillo, R. Maniyara, **J. Rombaut**, K.K. Gopalan, N. Bareza, V. Pruneri. "Nano-structured optical surfaces base on ultrathin materials for displays and sensing". 10th International Conference on Metamaterials, Photonic Crystals and Plasmonics 2019.

- P. Mazumder, **J. Rombaut**, V. Pruneri. "Broadband, wide-angle, anti-reflection, superhydrophobic substrat". Conference on Nature Inspired Surface Engineering (NISE) 2019.

- K.K. Gopalan, M. Marchena, **J. Rombaut**, I. Gris, D. Rodrigo, V. Pruneri. "Graphene for transparent conductors and infrared sensing". CLEO-PR, OECC & PGC 2017.

- M.A. Noyan, K.K. Gopalan, R.A. Maniyara, M.Marchena, V. Mkhitaryan, **J. Rombaut**, M. Rude, R. Sibilo, I. Mannelli, J. Canet, V. Pruneri. "Multifunctional nano-structured optical surfaces for industrial applications". Nanometa 2017.

# Contents

# List of Figures

# List of Tables

# 1

# Introduction

## 1.1 Motivation

Transparent optical surfaces are essential components in a wide range of optoelectronic devices, including display screens, sensors and solar panels. Such applications belong to highly competitive and innovative industries, where much effort has been directed towards developing multifunctional optical surfaces. Anti-reflection (AR), light-absorption, liquid repellency or anti-fogging are examples of properties that could have a considerable impact on the optoelectronic industry. In recent years, a combination of enhanced optical properties and self-cleaning capabilities have been extensively studied for their applicability and scope.

Nature has provided numerous examples of functionalised surfaces with advanced properties to better adapt to the environment[1–4]. Many biological systems have developed sophisticated nanostructures that are of great industrial interest to tackle human problems. For instance, in the corneas of a moth's eyes, researchers found nanostructures that minimise light reflectivity over a broad range of wavelengths and angles of incidence, increasing visibility under difficult light conditions and reducing reflectivity, helping the moth to hide from predators[2,5–10]. The wings of some butterflies are composed of nanostructures that reflect specific bright colours for mating reasons or camouflage[11–13]. For self-cleaning purposes, lotus leaves possess elaborate micro-and nanostructures, which, combined with their chemistry, make their surface superhydrophobic and easy to clean[14–16].

Biomimetics or biomimicry is the science that tries to emulate these systems and develop manufacturing techniques to create bio-inspired synthetic structures that could add improved optical characteristics, self-cleaning capabilities, anti-microbial properties, or a combination of these to our daily devices. Many fabrication techniques have already been successful in creating such small structures, but implementing these methods at an industrial level remains one of the biggest challenges this technology is facing.

The main objective of this thesis is to find and develop new methods to overcome the principal drawbacks of state-of-the-art solutions, and to develop easier ways to create nanostructured multifunctional optical surfaces. The work focuses on transparent surfaces that combine improved optical properties with high transmission, low reflection, and low scattering, with the ability to remain clean under difficult environmental conditions by creating superhydrophobic and oleophobic surfaces.

## 1.2 Overview of Anti-Reflective Optical Surfaces

During the last century, different methods and strategies have been developed to reduce light reflection. This optical phenomenon occurs when light travels from one medium to another. Every medium (air, water, glass, etc.) can be optically characterised by its refractive index, which quantifies the speed of light in the medium with respect to that under vacuum. In 1821, Augustin-Jean Fresnel presented the basic preliminary mathematical model of reflection and refraction. According to his equations, when light interacts with an interface, a fraction is reflected (measured by reflectance), and the rest is transmitted (measured by transmittance). Reduction of the Fresnel reflection at optical interfaces is a topic of enormous interest for a wide range of applications, and solutions based on thin films, multilayer coatings and patterned surfaces have been proposed to eliminate such undesirable effects. Some of the most common anti-reflective systems are described below.

### 1.2.1 Optical Thin Film Theory

The first type and the purest form of AR coating was the index matching discovered by Lord Rayleigh in 1886. At that time, optical glass tended to develop a tarnish on its surface. Rayleigh found that slightly tarnished pieces of glass had better optical properties than new or clean glass. This is due to the effect of the tarnished layer between the air and the glass creating a

refractive index gradient that exhibits less reflection than the air-glass interface.

Since then, the technology of AR coatings has grown significantly, and many research groups have studied and proposed different methods to reduce the reflection of optical surfaces. The most straightforward interference AR coating can be created by using a single thin layer of a transparent material with an adequate refractive index and thickness[17–22]. According to the Fresnel laws, if the refractive index of the coating is equal to the square root of the substrate's refractive index, and the thickness is equivalent to a quarter-wave plate, the reflection of the substrate for a single wavelength can be suppressed. The AR effect comes from the destructive interference of the multiple reflected light rays eliminating each other, as shown in Figure 1.1.
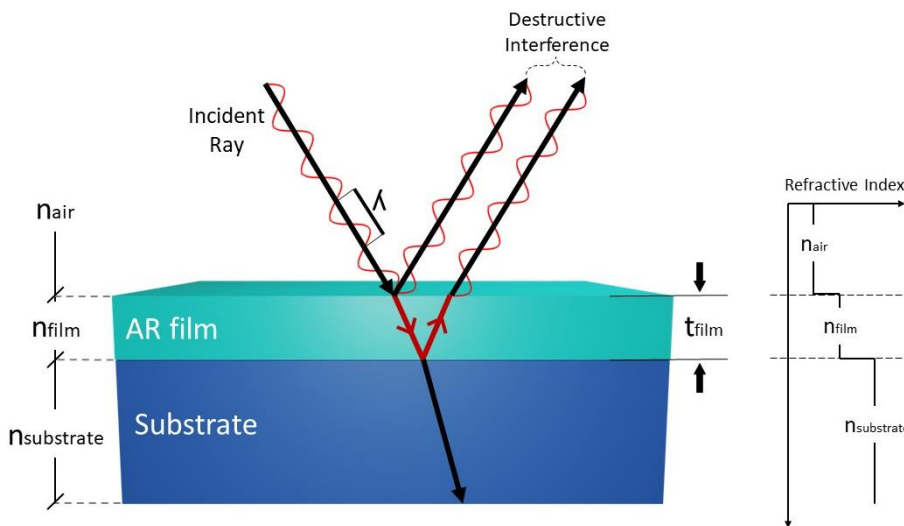


*Figure 1.1 Schematic drawing of the light interaction phenomenon with an anti-reflective single-layer coating.*

Fresnel's equations can calculate the reflection of a substrate for normal incidence as[22]:

$$R = \left(\frac{n_{air} - n_{substrate}}{n_{air} + n_{substrate}}\right)^2 \qquad (1)$$

where R is the total reflection, and $n_{air}$ and $n_{substrate}$ are the refractive indices of the air and the substrate material, respectively.

When a thin coating with refractive index nfilm is placed at the interface between medium 1 (air) and medium 2 (substrate), if the multiple reflected rays are completely out of phase (π-phase difference), all the light beams reflected backwards eliminate each other due to destructive interference, as represented in Figure 1.1.

In order to effectively create the destructive interference required to eliminate the reflection for a certain wavelength, the thickness of the film ($t_{film}$) can be calculated as:

$$t_{film} = \frac{\lambda}{4\,n_{film}} \qquad (2)$$

where λ is the wavelength at which the reflection will be suppressed and $n_{film}$ is the refractive index of the single-layer coating. Then, the combined reflection of the coated substrate for normal incidence can be resolved as:

$$R = \left(\frac{n_{air}n_{substrate} - n_{film}^2}{n_{air}n_{substrate} + n_{film}^2}\right)^2 \qquad (3)$$

The $n_{film}$ required for an optimal AR effect between the air and the substrate can be calculated by:

$$n_{film} = \sqrt{n_{air}\,n_{substrate}} \qquad (4)$$

In general, glass substrates have a refractive index of around 1.5 and an approximate reflection of 4% at each surface. A single layer of a material with a refractive index of around 1.2 would significantly reduce the reflection at a particular wavelength (depending on the $t_{film}$). The closest materials with good physical properties for coatings are magnesium fluoride[22,23], with n=1.38, and fluoropolymers with a refractive index of around 1.3. These materials are the best choices to reduce the reflection of transparent glass surfaces down to 1% per face with a single-layer AR coating. However, despite the simplicity and performance of this method, the optimal AR effect is limited to a single wavelength and normal incidence[24], and the number of available materials with adequate refractive index is greatly limited.

A better and well-established method to improve the AR effect of single-layer coatings is by using multilayer interference coatings[25–27]. Although these are more expensive, by alternating low-index and high-index materials, it is

possible to create destructive interference of the multiple reflected rays for a wider wavelength range, and to obtain reflections very close to 0% for normal incidence (Figure 1.2). Today, state-of-the-art AR coatings are most frequently based on these interference structures, and can be seen on optical lenses, solar cells and lasers. Unfortunately, such layer systems also tend to perform sub-optimally in many aspects. Designed for limited wavelength ranges and only for normal incidence, the thin-film coatings suffer from both adhesion problems and radiation damage if the optical device is used over a broad thermal range, or in high power laser applications. They are very sensitive to thickness variations and it is difficult to find suitable materials to create broadband anti-reflective coatings.
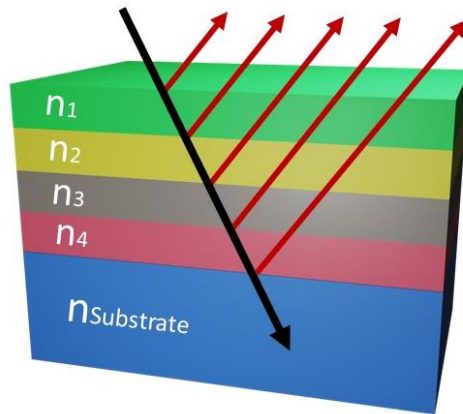


*Figure 1.2 Schematic illustration of an anti-reflective multilayer coating. The anti-reflective effect comes from the destructive interference of the multiple reflected waves from each interface.*

### 1.2.2   *Gradient of Refractive Index*

Although many different coatings have been studied theoretically for broadband anti-reflection, finding materials with such a low refractive index remains a challenge. In 1880, Lord Rayleigh introduced the idea of materials with variable refractive indices[28]. This concept has been studied theoretically for many years and has demonstrated impressive AR properties, with the first film with a non-uniform refractive index being fabricated in 1960. One practical solution was proposed by Xi et al. with oblique-angle deposition coatings. Alternating silicon dioxide ($SiO_2$) and titanium dioxide ($TiO_2$) with different angles of deposition, they managed to tune the refractive index of the deposited layers to create a gradient refractive index from the air to the substrate, achieving significant AR results[29]. The system, however, has some

limitations. First of all, due to its flatness, the multifunctionality of the surface is limited to only AR effects, and secondly, the mechanical resistance of the proposed multilayer is compromised by the adhesion of the materials.

### 1.2.3    *Nanostructured Moth Eye Surfaces*

One alternative to single and multilayer AR coatings that could mitigate the issues mentioned above would be to use subwavelength or anti-reflective patterned surfaces, which, in nature, are found in the eyes of nocturnal insects. In the case of moths, the surface of each cornea is equipped with a hexagonal array of cuticular nanostructures (Figure 1.3). The function of these nipple arrays could be to suppress reflection from the faceted eye surface to avoid fatal consequences for the moth if the reflection were to be detected by a bird or any other predator[7,30,31]. The AR effect of the structure is typically linked with an enhancement in transmission, thereby also improving the visibility of these insects in low light environments. The surface can be understood as a gradation of the refractive index between the air and the corneal material. As the distance between the pillars is sufficiently small, the structure cannot be resolved by the incident light. Hence, the transition between the air/material interfaces will appear as a continuous boundary, with the effect of a decreased reflection and improved transmittance of all light with a wavelength larger than the spacing period.
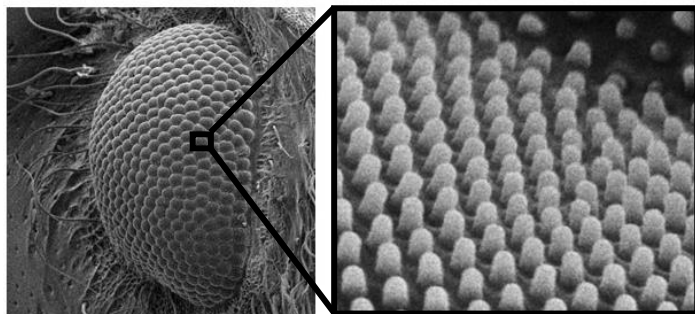


*Figure 1.3 Scanning electron microscope (SEM) images of a moth's eye[7]. The surface is equipped with an array of tiny protuberances, which induces a smooth refractive index gradient from the air to the cornea of the insect. These biological structures have been a valuable inspiration in the creation of different artitificial anti-reflective nanostructured surfaces*

Nanostructured materials can create different profiles of refractive index gradients. As shown in Figure 1.4, the geometry of the structures determines the smoothness of the change of refractive index from the air to the substrate material. For straight structures or porous materials, the optical response can be calculated as a thin film with an effective refractive index determined by the ratio of the air to the substrate material. If the shape is more conical, a smoother transition of the refractive index is achieved. Tapered subwavelength structures can greatly reduce the Fresnel reflection, as has been experimentally proven on different moths' eyes and also on artificially created structures[32–36]. In 1991, the optimal geometry of AR nanostructures was proposed by Southwell[37], who theoretically studied an array of square-based pyramids with curved faces, creating the smoothest transition of refractive index. Unfortunately, despite their impressive optical properties, such structures are extremely difficult to fabricate and the sharp tips of the pyramids are vulnerable to mechanical stress.
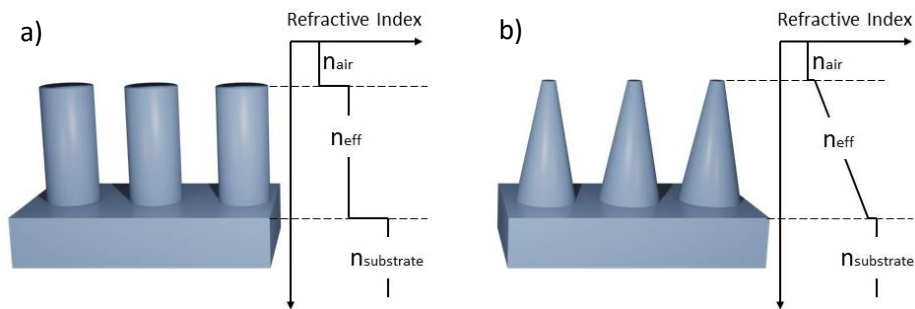


*Figure 1.4 Cross-section illustrations of different nanostructured profiles: straight cylindrical pillars (a) and conical structures (b). The geometry of the structures has a direct impact on the effective refractive index between the air and the substrate material, producing different anti-reflective responses.*

Nanofabrication methods where the shape of the nanostructures can be controlled allow for optimisation of the system for specific applications. As will be demonstrated in this thesis, as well as improving the optics, nanostructured surfaces can offer several other advantages compared with state-of-the-art multilayer coatings. For instance, aside from its mechanical and chemical stability, the roughness of a surface can improve its wetting properties, adding self-cleaning characteristics.

## 1.3 Self-Cleaning Surfaces

Materials with self-cleaning properties are those with the inherent ability to keep their surfaces clean from dirt, debris or bacteria. In general, easy-to-clean surfaces can be divided into two major groups. The first ones are based on bio-inspired surfaces, where superhydrophobic, superomniphobic, or superhydrophilic states can be achieved by modifying the surface's roughness and its chemical composition. The second ones use external agents, such as electrostatic fields or vibration systems, to actively clean the surface. These materials have attracted tremendous commercial interest in electronic devices, solar panels, windows of buildings and vehicle windshields, where their self-cleaning properties have to be combined with high transparency. In this thesis, only the first type has been investigated and developed.

In the study of self-cleaning surfaces, wetting refers to the ability of a liquid to interact with a solid surface. The surface tension and the contact angle (CA) are two concepts used to determine the wettability of a solid. The surface tension is defined as the required energy to expand the surface area of a liquid[38,39]. As shown in Figure 1.5, below a droplet's surface all the liquid molecules are surrounded by other liquid molecules. This equilibrium of intermolecular forces does not exist on the surface of the droplet (where the molecules are only partially surrounded), creating a constant inward pressure and contracting the liquid into the lowest surface area for a fixed volume, a sphere[40]. In the particular case of a liquid droplet placed on top of a surface, the relative strength of the internal forces between the liquid molecules and between the liquid and solid molecules determines the wettability of the solid towards the liquid.
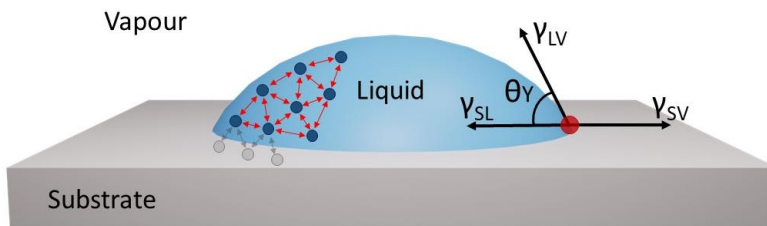


*Figure 1.5 Schematic drawing of a liquid droplet on a solid surface. The interfacial surface tensions at the three-phase contact point (red dot): $\gamma_{SV}$ (solid-vapour), $\gamma_{SL}$ (solid-liquid) and $\gamma_{LV}$ (liquid-vapour). $\vartheta_Y$ is the Young's contact angle.*

The CA of a liquid is the angle formed by a droplet with respect to the surface at the three-phase contact point, i.e., the intersection of the solid-liquid and liquid-vapor interface[41–43]. As shown in Figure 1.5, when the droplet is in equilibrium and the surface tensions are counterbalanced, the contact angle can be theoretically calculated using Young's model equation[44]:

$$\gamma_{SV} - \gamma_{SL} - \gamma_{LV} \cos \theta_Y = 0 \qquad (5)$$

where $\gamma_{SV}$, $\gamma_{SL}$ and $\gamma_{LV}$ are the interfacial tensions of solid-vapour, solid-liquid and liquid-vapour, respectively, and $\theta_Y$ is the CA. Although this model is a good approximation to explain the basics of interfacial interactions, it has been criticised in multiple works as it considers a static scenario with a perfectly flat surface, and the calculations can differ slightly compared with experimental results[41,45,46]. However, it is still useful in order to evaluate the surface free energy of different materials[38]. In an equilibrium state, if the surface free energy of the solid (substrate) is lower than the liquid, it will promote a non-wetting behaviour (high CA), whereas if the surface free energy of the solid is higher than that of the liquid, the fluid will tend to wet the surface and a lower CA will be measured.

CA values are commonly used as an indicator of the wettability of surfaces[47,48]. In general, if the water CA is smaller than 90°, the surface is defined as hydrophilic (high wettability), whereas if the CA is greater than 90°, the surface is considered hydrophobic (low wettability). For surfaces with enhanced wetting properties, the structure is considered superhydrophilic for a CA below 10° or superhydrophobic for a CA greater than 150°[48,49].

In practice, to completely characterise a surface's wettability, the dynamic contact angles are measured in addition to the static CA[50]. As shown in Figure 1.6a, the advancing CA ($\theta_A$) refers to the angle of the droplet when it is expanding, and the receding CA ($\theta_R$), when it is contracting. The dynamic contact angles can also be calculated by tilting the substrate up to the sliding angle ($\alpha$), the point at which the droplet starts to advance over the surface (Figure 1.6b). The difference between the $\theta_A$ and $\theta_R$ is called the CA hysteresis (CAH) (equation 6), and is a crucial parameter in determining the self-cleaning capabilities of a surface, by analysing the ease of a droplet to roll-off[51,52]. The lower the CAH values, the easier a droplet will tend to roll-off over the surface.

$$CAH = \theta_A - \theta_R \qquad (6)$$
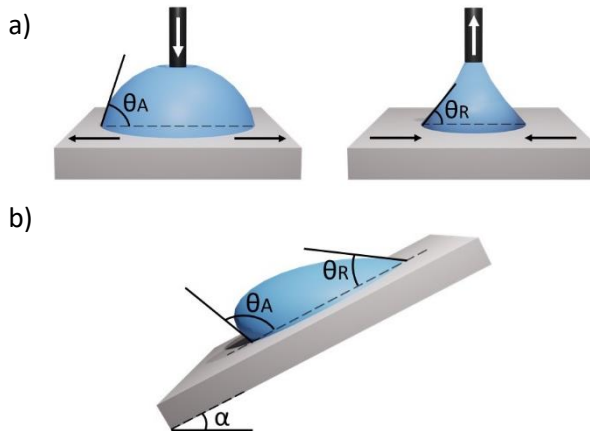
*Figure 1.6 Schematic of the two different methods to measure the advancing CA ($\vartheta_A$) and the receding CA ($\vartheta_R$). Expanding and contracting a liquid droplet (a) or tilting the surface up to the sliding angle (α) (b).*

Over the recent years, much effort has been dedicated to understand the mechanism of passive self-cleaning surfaces and to develop new fabrication methods. It has been demonstrated that the wetting characteristics are highly related to the surface chemistry and the surface roughness or topography.



*Figure 1.7 (Left) Photograph of a lotus leaf showing superhydrophobic behaviour. (Right) Scanning electron microscope image of the rough surface of a lotus leaf at the micro-scale[53].*

Nature, again, has provided great examples of self-cleaning surfaces. The botanist Wilhelm Barthlott examined one of the best-known water-repellent surfaces found on Earth, the lotus leaf[15,16,53]. Its superhydrophobicity has been attributed to the elaborate micro-and nanostructures that cover the surface of the leaf (Figure 1.7) combined with its chemical composition. The increased roughness of the surface reduces the contact area between the leaf and water, lowering the adhesion of the liquid and also improving the roll-off effect of the

droplets on its surface. In addition, the surface is composed of epicuticular wax crystals that also offer water-repellence properties by reducing the surface free energy. Since the first discoveries, more than 200 species of plants, and even some insects, have been found with self-cleaning properties that combine nanostructures with special chemistry.

The study of biomimetic nanostructured materials has demonstrated how increasing the roughness of a surface can enhance its wetting properties[54]. This phenomenon can be explained by the increase in the effective area in contact with the liquid, amplifying its wetting characteristics. In other words, nanostructuring hydrophilic materials will increase their wettability, while with hydrophobic materials it will decrease the wettability. The effect of the roughness on the CA can be demonstrated using the two mathematical models described below.

Two primary states exist to describe the wetting characteristics of nanostructured surfaces. As shown in Figure 1.8, if the droplet fully wets the structure, including the spaces between the nanopillars, the Wenzel model[55] is used to characterise the effect of the roughness on the surface's wetting behaviour. On the contrary, if the liquid droplet rests on the tips of the structures, and there are air cavities beneath the droplet, a model introduced by Cassie and Baxter[56] can define the wetting behaviour of the surface.
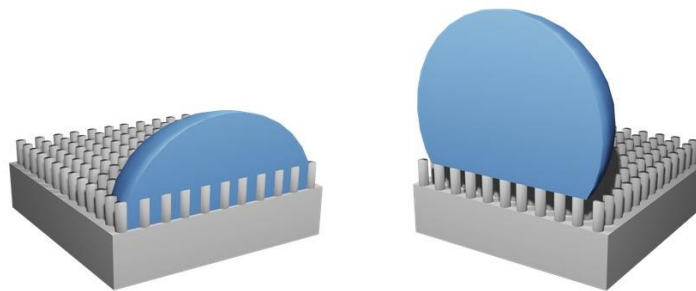


*Figure 1.6 Schematic illustration of liquid droplets on textured surfaces. (Left) Representation of the Wenzel state, where the liquid seeps into the structure, improving the wettability of the surface. (Right) Representation of the Cassie-Baxter state, where the droplet reposes on top of the structures, with trapped air below the liquid, reducing its wettability.*

Robert N. Wenzel purposed an equation to describe the influence of the roughness on nanostructured surfaces according to:

$$\cos \theta_A = r \cos \theta_Y \qquad (7)$$

where $\theta_Y$ is the equilibrium contact angle determined by Young's equation (also called the Young contact angle), $r$ is the average roughness ratio (total area divided by the projected area), and $\theta_A$ is the apparent contact angle. For instance, a regular flat glass surface typically has a CA of 40°. If it is nanostructured, and the total surface area is increased 1.3 times with respect to the projected area, the calculated apparent contact angle is now 5°, and it demonstrates superhydrophilic behaviour.

The Cassie-Baxter model supposes that the liquid droplets repose on top of the structures, the apparent CA is evaluated with the fractional surface areas between the tips of the structures and the trapped air below the liquid droplet, as follows:

$$\cos \theta_A = f_s \, \cos \theta_Y - f_{air} \qquad (8)$$

$$f_{air} = (1 - f_s) \qquad (9)$$

where $\theta_Y$ is the equilibrium contact angle determined by Young's equation, $\theta_A$ is the apparent contact angle, and $f_s$ and $f_{air}$ are the area fraction of the substrate and air under the droplet, respectively. For example, if a flat surface of a particular material has a Young CA of 115°, assuming a $f_s$ of 0.25, the apparent contact angle would be almost 150°. If the ratio of air increases, the wettability of the surface decreases and higher CA would be measured.

The previous examples represent two different approaches which are used to passively keep surfaces clean from dirt or contaminants, these being superhydrophobicity and superhydrophilicity. On superhydrophobic surfaces, the water droplets will roll-off easily, picking up all the undesirable particles and removing them (Figure 1.9 - left). Low sliding angles and low CAH are needed for this scenario. In the case of superhydrophilic surfaces, the water will spread out quickly and flow between the substrate and the contaminants (Figure 1.9 - right), carrying the contaminants off the surface. High wettability and low CA values are needed to achieve this condition, which normally induces ultra-fast drying of the surface.
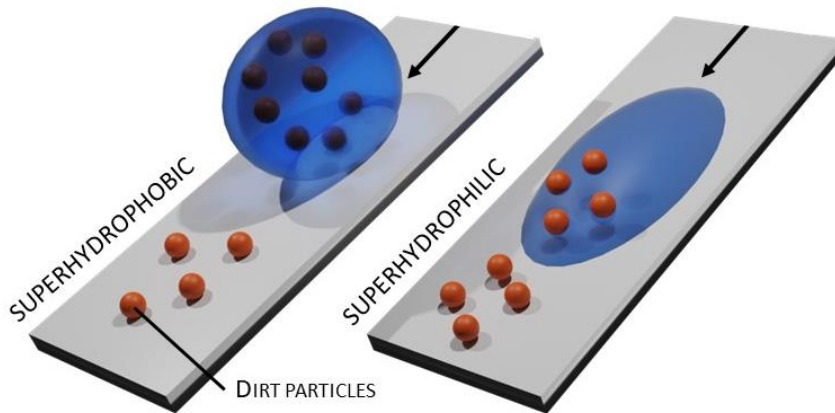
*Figure 1.7 Illustration of two different approaches for passive self-cleaning surfaces. Superhydrophobic behaviour with low contact angle hysteresis uses liquid droplets to pick up all the undesirable particles (lotus leaves method - left). The high wettability of superhydrophilic surfaces is used to spread out the liquid and make it pass underneath the particles to carry them off the surface (right).*

## 1.4 Aims and Potential Impact of the Thesis

The main aim of this thesis is to design and develop multifunctional optical surfaces for optoelectronic devices. The objective is to combine improved optical and self-cleaning properties on transparent materials with finding new mass-scalable ways to modify the surfaces on the nanoscale.

This general aim is addressed through the following specific objectives:

- Design, fabrication and experimental demonstration of bio-inspired optical surfaces with high transmission, low reflection and low scattering for different materials and applications. Investigation and development of different designs and their effect on the overall performance of the surface.

- Analysis and improvement of the mechanical resistance of the proposed nanostructures in order to enhance their optical and wetting properties for applicability into real devices.

- Development of new methods to nanostructure transparent surfaces, which are mass-scalable, faster, low-cost and have enough resolution to beat state-of-the-art techniques.

- Creation of prototypical optical surfaces with multifunctional properties (e.g. antireflection and self-cleaning abilities) for specific applications in the mobile or automotive industries (specific customers).

## 1.5 Thesis Outline

This thesis is organised into seven chapters as follows:

Chapter 2 provides a brief introduction to previous work on bio-inspired nanostructured surfaces. The fabrication techniques and equipment used for nanostructuring inorganic and organic substrates in this thesis are described. The characterisation methods used to analyse and optimise the modified surfaces are also included.

Chapter 3 describes the first work on glass. Nanopillars were created and optimised for different regions of the spectrum for specific applications, demonstrating great anti-reflective (AR) performance and superhydrophobic behaviour. Complete analysis of the properties and mechanical resistance of the samples are also presented.

Chapter 4 introduces a new concept design for the creation of AR surfaces. The merging of two designs (AR multilayer coatings combined with nanostructured surfaces) is demonstrated as a possible solution for specific applications. The design, fabrication, and characterisation are described, as well as the numerical calculations used to optimise the proposed structures. Part of the results presented were used in Publication *ACS Photonics 2021, 8, 3, 894-900*.

Chapter 5 proposes a different nanostructure design (nanoholes on glass substrates) which focuses on achieving improved oil-repellence behaviour and higher mechanical resistance. The patterned surface also presents improved optical properties. Two different fabrication methods to create subwavelength nanoholes were developed and optimised, and experimental results are shown. This work was used in Publications *ACS Appl. Mater.*

*Interfaces 2018, 10, 49, 43230-43235* and *ACS Omega 2019, 4, 22, 19840-19846.*

Chapter 6 demonstrates that one of the methods presented in Chapter 5 can be adapted for other materials, in this particular case for flexible transparent polymers. Polyimide was successfully nanostructured, improving not only its optical properties, but also creating an AR film to reduce reflection on the surfaces of both glass and glass coated with electrically conductive ITO films. The results obtained in this work were used in Publication *ACS Omega 2019, 4, 22, 19840-19846.*

Finally, in Chapter 7, the outputs of the thesis are highlighted and summarised, providing an outlook for future applications.

# 2

# Methods and Characterization Techniques

## 2.1 Lessons from Nature

Biomimetics is defined as the study and development of synthetic systems inspired by nature. Through evolution, many species and organisms have developed interesting micro-and nanostructured surfaces with unique properties such as anti-reflection, self-cleaning, light-absorption, drag-reduction and camouflage, among others[1,4,57,58]. In the development of multifunctional surfaces, bio-inspired textured materials have great commercial interest as they are able to improve the performance of many optoelectronic devices. For transparent optical surfaces, the combination of enhanced optical properties with self-cleaning capabilities has been widely studied for its technological relevance and possible applications.

The moth-eye is one of the most valuable examples of bionic anti-reflective systems. In the early 1960s, C.G. Bernhard found nipple arrays on the eyes and wings of some insects (moths and some butterflies) and suggested that these were for camouflage purposes, to reduce their vulnerability against predators[9]. As explained in the first chapter, tapered profiles with subwavelength dimensions can induce a gradual refractive index at the interface between the material in the cornea of the eye (refractive index around 1.54) and the air, reducing surface reflection and increasing transmission over a large range of wavelengths and angles of incidence. For practical applications, such characteristics could have a great impact on the solar or the display screens industries. There are many examples of improved optical properties with moth-eye nanostructures in literature[5,7,31,59]. For

commercial applications, Apple has recently introduced nano-textured displays to reduce undesirable reflections while keeping high contrast and clear image.

More complex structures are found on the leaves of the lotus plant, one of nature's most water-repellent surfaces and one of the best examples of self-cleaning[14,15,58,60]. The surface combines micro-protuberances with nanostructures, reaching superhydrophobic states with large water contact angles and improved roll-off effects. As also explained in the first chapter, the outstanding water repellence comes from the increased roughness of the surface, with an optimised geometry that traps the air in the crevices and prevents the water from adhering to the surface, together with the chemical composition of the epicuticular waxes, which reduces the surface free energy of the leaves.

One of the challenges of biomimetics is how to fabricate such elaborate structures in the micro-and nanoscale, especially for mass production. Following the late advances in nanofabrication techniques, many research groups have been actively working on this subject, proposing innovative techniques to nanostructure surfaces. However, most of the developed methods are not scalable and involve expensive and time-consuming processes. Alternatives to the current techniques are presented in this thesis, and focus on developing faster, cheaper, and large-area processing techniques that can be implemented at an industrial level with high resolution, and using common inorganic and organic materials.

## 2.2 Fabrication Techniques

Most of the fabrication techniques for nanostructuring surfaces can be split into two main categories: bottom-up and top-down methods[61]. The bottom-up approach refers to chemically synthesised or self-assembled basic units used to generate larger structures, from the atomic and molecular levels to complete nanostructures. On the other hand, top-down techniques are based on removing or etching materials from a substrate in a controlled manner until the nanostructure is obtained.

The bottom-up, or chemical synthesis method, involves scalable and straightforward deposition of thin films that can serve as a mask for a subsequent etching process or can be directly transformed into

nanostructured surfaces through chemical procedures. Although large scale areas can be patterned and do not usually involve sophisticated equipment, these methods suffer from compatibility issues between the self-organised molecules and the surfaces, and the geometry of the structures cannot be defined or tuned as well as with other techniques.

Colloidal lithography is a common bottom-up approach, where monodispersed spherical colloids are deposited on a substrate using different coating methods (e.g., the Langmuir-Blodgett process or spin coating) to create a uniformly distributed nanomask for etching the substrate[62]. The deposited array of nanospheres protects part of the surface during the etching process, and its distribution and shape can be transferred to the substrate to create nanopillars, for instance. Another method for synthesising inorganic nanopatterns is by micellar block copolymers[36,63]. With the help of a precursor, these polymers can self-organise into nanodomains on top of different substrates with better adhesion than colloids, making them suitable candidates for bottom-up lithographic techniques. Another approach to directly create anti-reflection nanostructures was proposed by Yen-Chun Chao et al. with a ZnO nanorod array[64]. A thin film of Zinc acetate diluted in an ethanol solution was spin-coated on a silicon substrate, and the samples underwent heating and hydrothermal processes in order to grow ZnO nanorods.

The top-down approaches often use micro-and nanofabrication methods, where externally controlled tools are used to cut or etch a bulk material. Although there is equipment, like focussed ion beam milling, that offers impressive resolutions (~5nm), most of the procedures involve extensive lithography processes which are expensive, very time-consuming, and not scalable for use on large surface areas[65].

Electron beam lithography (EBL) is a top-down technique with which nanostructures can be directly created on a photoresist material without using a photomask[66]. The resolution is to the order of a few nanometres as the wavelengths of electron beams are much smaller than those of photons and are not limited by the diffraction limit of light. Although this technique is one of the most accurate systems for nanostructuring photoresist masks, there are some important shortcomings related to heating problems, as the system requires high-voltages beams, and proximity and fogging effects, created by scattered electrons in the resist and substrate, causing distortion of the

original pattern designs. In addition, the high cost of the instruments and the extremely low throughput of the method hinders the use of EBL for high-volume fabrication. Multiple e-beam lithography systems have been investigated recently, with promising results, but still present undesirable defects during fabrication, such as stitching, which cause deformation on the mask patterns.

Optical lithography, also known as photolithography, has been widely used in the semiconductor industry and is one of the leading methods for fabricating nanostructures on optical surfaces[65]. The process starts with the deposition of a photoresist material, which can be chemically modified by light exposure (ultraviolet light). The photoresist is patterned with the help of a photomask, which exposes and unexposes different regions of the material. Once it is cured and well adhered to the substrate, the photoresist is typically used as a mask in a dry etching process, transferring the nanopatterns to the surface. At the end of the fabrication process, the remains of the mask can be chemically removed. The main drawback of ultraviolet lithography is the limited resolution, which is associated with the wavelength of light used to expose the resist. The first instruments were limited to sizes of hundreds of nanometres, but thanks to the development of various techniques such as immersion lithography, extreme UV lithography and projection lithography, the resolution has improved to include sizes smaller than 10nm. However, these techniques require expensive instruments and complex facilities, and the processing speeds still limit their implementation for mass fabrication.

Laser interference lithography is a novel fabrication method based on the setup of Lloyd's mirror interferometer[67,68]. This technique does not require a photomask to selectively expose the photoresist, and it uses the periodic patterns created by interfering multiple UV laser beams, using a mirror and tilting the receiving substrate. Although it reduces the costs of the previously mentioned techniques and can nanostructure larger areas, the pattern designs are limited only to periodic arrays, the equipment needed is still expensive, and it is challenging to implement on production lines.

Nanoimprint lithography (NIL) uses a micro- or nanostructured mould to deform the resist or other polymeric materials mechanically[69–71]. The size and distribution of the structures depend on the mould used, and the process is compatible with large-area fabrication. However, despite its reduced cost compared with other lithographic techniques and its high resolution, the

fabrication of a mould still requires expensive and complicated methods, and dimensions below hundreds of nanometres are hard to obtain without defects, typically induced during the demoulding step.

This thesis focuses on finding scalable techniques that, when combined, can create nanostructures on different materials. The main requirements to make this technology industrially feasible are finding cost-effective methods, for large area surfaces and with enough control and precision to adapt the design for different applications. The methods to nanostructure inorganic and organic materials presented in the following chapters combine the advantages of both approaches, i.e., the low-cost, scalability, and uniformity of bottom-up strategies, and the fine control of top-down techniques. Solid-state thermal dewetting has been extensively explored to create masks with nanoparticles for etching processes[72,73]. By rapidly annealing ultra-thin metallic films in high temperatures, the continuous film self-collects into small close-to-spherical particles on the surface. The parameters of the thermal process and the thickness of the film together control the dispersion and the size of the particles. Reactive ion etching has been utilised to precisely transfer the metallic patterns onto the surfaces of the materials. Most of the fabrication methods developed in the next chapters share some processes and characterisation techniques, and the systems and equipment used to produce such nanostructures are described in the following sections.

## 2.2.1   *Sputtering*

In all the experimental chapters of this thesis, an ultra-thin metal film deposition is involved. The methods developed so far to deposit thin layers of different materials are divided into two main categories: Chemical Vapor Deposition (CVD) and Physical Vapor Deposition (PVD). Both systems can deposit films of a few nanometres in a controlled manner, but follow different approaches[61].

CVD is a chemical process used to produce high-purity thin films, employing a precursor that chemically interacts with the substrate inside a chamber under high vacuum. The deposition is controlled by a chemical reaction, where some of the materials mixed in the vapour phase react and are deposited on the surface as a thin film. PVD is used to produce extremely hard and corrosion-resistant metal coatings. This method uses physical energy (mechanical, electrical or thermal) to release a material from a source and deposit it onto

the substrate. The target material goes from a solid to vapour phase and then back again to a solid phase, as a thin film. One of the most common methods of PVD is sputtering.
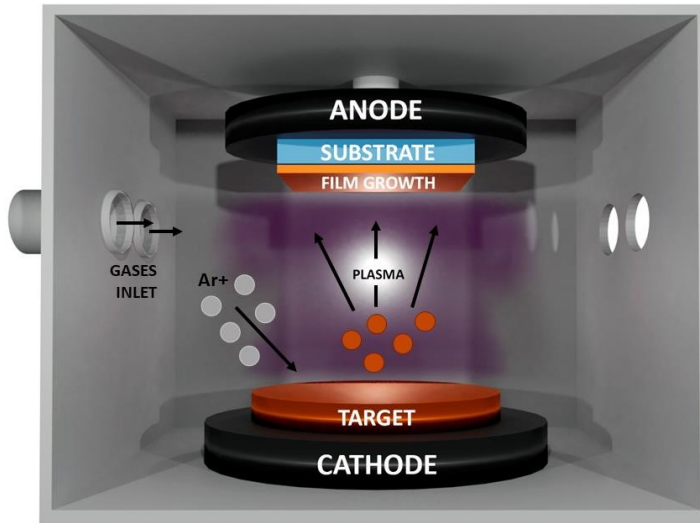


*Figure 2.1 Schematic representation of the sputtering process.*

Sputtering is a technique used for large-area deposition of metals, dielectrics and their alloys, and compounds. The process is based on converting a solid material (target) into a gaseous phase using plasmas, and then depositing it onto a substrate (Figure 2.1).  The target and the substrate are placed into a chamber under a high vacuum while a process gas is introduced to create a controlled atmosphere (Argon (Ar), in most cases). In order to transfer material from the target to the substrate, an electric field is applied between them, leading to the creation of Ar+ plasma with accelerated Ar+ ions towards the cathode (target). Positively charged Ar ions are generated by free electrons hitting the neutral gas atoms. The free electrons are accelerated away from the negatively charged electrode (cathode) and, due to the momentum transfer from the ions to the target material, particles are detached (sputtered), resulting in the deposition of a film on the substrate situated just above the cathode. Various factors can influence the deposition, including temperature, substrate morphology and the gaseous components. Introducing gases into the chamber and making them react with the metal particles before reaching the substrate can create different stoichiometric compounds. Sputtering systems can be classified by the power source used, being radio-frequency (RF) magnetron sputtering or direct-current (DC) magnetron sputtering. The former is widely used to deposit oxides, as

demonstrated in Chapter 4 of this thesis, while the latter is used for metal deposition.

Sputtering was the method chosen for this thesis as it can produce high quality films, with good uniformity and low levels of impurities, and has the highest rate of scalability of all the PVD techniques, making it convenient for ultra-thin metal depositions and mass fabrication.

Figure 2.2 shows the sputtering equipment used in this thesis and installed in ICFO's NanoFabrication laboratory. The ATC Orion 8m from AJA International, Inc. is a computer-controlled, automatic RF/DC system, equipped with five 3-inch targets inside the main chamber and designed to coat substrates up to 5 inches in diameter. It has 3 DC and 2 RF power sources for co-sputtering (deposition of multiple materials simultaneously). The processes are run under high vacuum ($10^{-8}$ Torr), and this particular system has a turbo-pumped vacuum load lock to introduce samples without affecting the main chamber vacuum (more than 3 hours is needed to reach the operational vacuum). The system has a series of gas pipes (Oxygen and Argon for reactive sputtering, and Nitrogen for venting the load lock chamber) and thermal heaters that allow deposition under high temperatures (up to 800°C).



*Figure 2.2 AJA Orion 8 HV Magnetron Sputtering System installed in the NanoFabrication laboratory at ICFO.*

For each experiment and material, the deposition rate was characterised by a complete morphological analysis of the deposited layers, with the equipment described in the following sections.

### 2.2.2 *Dewetting*

Solid-state dewetting is a spontaneous phenomenon where a thin film transforms its structure into 3D islands[73,74]. Thin films deposited through vapour deposition are generally unstable or metastable in the as-deposited state. Heating activates mass transport and capillary forces, driving the film to agglomerate into nanoparticles. This process can occur well below the melting temperature, which maintains the dewetted material in the solid-state and permits the use of various materials as a substrate. The process strongly depends on the type of material, initial thickness of the film, temperature, time exposed, and the surface roughness. The correct optimisation of all the parameters and materials used allows for the creation of a controlled and reproducible array of nanoparticles with sizes ranging from 50nm to 1000nm and density from 20% to 50% (nanoparticles over substrate surface).

Sometimes, the dewetting phenomenon can occur during the formation (deposition) of ultra-thin films, which is often undesirable. For the fabrication methods proposed in this thesis, the dewetted nanoparticles can be used as a metal nanomask, a powerful tool to create tiny particles on different materials without expensive lithography processes. Dewetting typically starts on defects, holes, dirty particles or directly from the edges of the substrate. From there, it expands over the hole formation until it breaks up into perfectly spherical particles (Figure 2.3). The film thickness plays a key role in the ability of a film to dewet. For thinner film thicknesses, the dewetting process is accelerated, and lower temperatures are needed for optimal results. The particle size and density are also related to the film thickness. For each work, full optimisation of the process has to be carried out depending on the materials used and the pattern array required.
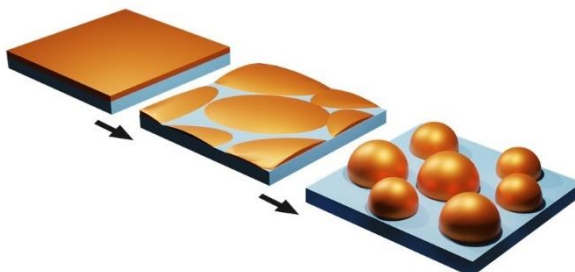


*Figure 2.3 Representation of the solid-state dewetting process. A uniform thin film self-assembles into isolated islands when rapidly heated. The thickness of the initial film, the temperature and the duration of the process will affect the distribution and size of the nanoparticles.*

Depending on the application, the chosen substrate and the geometry of the structure to be created, it is possible to dewet different metals. Copper, nickel or silver have been tested in this work for different purposes. To choose the best candidate, one has to consider the differential etching rate of the mask material compared with the substrate and, also, the maximal temperature the substrate can withstand without affecting its properties. For instance, copper films need a temperature to dewet higher than silver films, but are more resistant in a dry etching process and deeper structures can be created. In this thesis, copper was found to be the optimal material to use as a mask for most of the targeted applications because of its dewetting temperature, the particle size, the density, and the etching rate compared with glass.

The rapid thermal annealing system used to dewet the thin metal films is shown in Figure 2.4. The RTP-100-HV is a high vacuum rapid thermal processing oven with ramp-up up to 150°/sec and a maximum achievable temperature of 1200°C, due to top and bottom heating with 18 infrared (IR) lamps (20kW). The temperature is uniformly distributed in the quartz chamber using a graphite plate to hold the substrates. Samples up to 4 inches can be processed under high-purity $N_2$ to prevent oxidation of the thin metal films. The software allows the process to be controlled by creating recipes with different temperatures, ramps and exposure times.



*Figure 2.4 RTP-100-HV rapid thermal annealing oven installed in the Post-Processing laboratory at ICFO.*

## 2.2.3    *Reactive Ion Etching*

Reactive ion etching (RIE) is a high-resolution top-down technique generally used in nanofabrication processes[75]. Most etching methods are divided into two groups: wet and dry etching. The first one uses wet chemicals or etchants that remove materials from the surface following chemical reactions, inducing isotropic etching (Figure 2.5 (a)). The second one employs plasma or etchant gases that can remove materials through chemical reactions, physical removal, or a combination of both, inducing anisotropic etching[76,77] (Figure 2.5 (c)). Among all the etching techniques available to create nanostructures, RIE excels for its high process controllability, high anisotropy and ease of automation (scalability), without the need to use dangerous chemicals.

RIE is a type of directional dry etching process where the removal occurs due to the combination of physical sputtering and chemical reactions[78]. The process is performed in a vacuum chamber in the presence of an alternating electric field that generates the plasma. High energetic ions are accelerated by the field attacking the target surface and reacting with it. The presence of a voltage between the sample and the plasma leads to bombardment by reactive ions towards the sample, as in the sputtering systems. In the chemical sense, the ion bombardment improves the chemical reactions with the reactants on the target surface, producing volatile reaction products. The system can produce very anisotropic etch profiles due to the straight delivery direction of the reactive ions, while more isotropic etching can be performed by promoting the chemically neutral radicals.
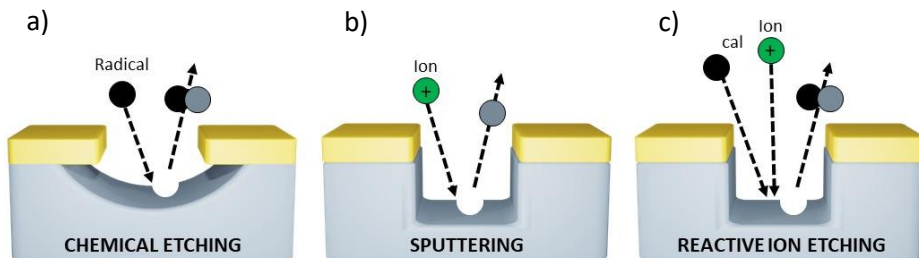


*Figure 2.5 Schematic drawing of different plasma etching mechanisms: a) chemical etching: radicals react with the substrate, taking volatile products; b) sputtering (physical): material removed through ion bombardment and c) reactive ion etching: combination of chemical and physical etching.*

During a RIE process, the most critical parameters are the chamber pressure, the RF power, the temperature, and the gases involved and their flow rates. All these parameters define the profile quality of the patterned surface, the etching rate and the selectivity. Depending on the mask material, all these parameters need to be optimised to obtain the desired structure. The pressure typically used in this process is $10^{-3}$ to $10^{-1}$ Torr, which directly affects the free path of the ions. Lowering the pressure improves the etching rate and anisotropy and helps to remove the etched products from the chamber. However, lower pressures make it more challenging to start the plasma process. Increasing the RF power will increase the ionisation, the etching rate and the bombardment energy, but the selectivity could be compromised. Regarding the gas compounds, halogens are typically used to etch inorganic and metallic substrates, and gas additives like oxygen ($O_2$), argon (Ar), helium (He) or nitrogen ($N_2$) affect the etching chemistry. In this work, the additive used was Ar, which enhances the physical process, provides stability to the plasma, and has sidewall passivation.

As with the dewetting process, a preliminary study was performed for each activity to define the etching rate of the substrate material and the metallic mask used to optimise the RIE process. Nickel, silver and copper were tested as mask materials, with copper again found to be the best option for nanostructuring glass substrates. As well as its adequate particle size and distribution after the dewetting step, its etching rate compared with the glass substrates helped determine the selection of the best mask material. Different topography characterisation techniques described in the following sections were used to measure the etching rates of the studied materials.
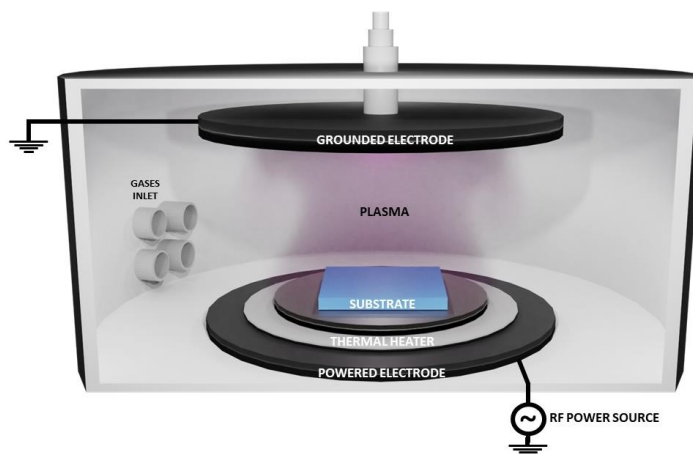


*Figure 2.6 Schematic representation of the reactive ion etching process.*

The Oxford Plasmalab System 100 from Oxford Instruments (Figure 2.7) was the equipment used for most of the dry etching processes developed in this thesis. The system is capable of producing anisotropic etching of silicon, silicon oxide, and other dielectric materials. The RIE combines an inductively coupled plasma (ICP) power source with a radio frequency (RF) power source that can be set up to 2500W and 600W, respectively. The etcher is compatible with wafer sizes up to 3 inches, and the manual load-lock system permits rapid loading of the wafers, maintaining the low pressure in the main chamber. The temperature of the main chamber can be controlled from -150°C up to 300°C, and the gasses used for the developed process were Ar, $O_2$, He, fluoroform (CHF$_3$), octafluorocyclobutane (C$_4$F$_8$) and sulfur hexafluoride (SF$_6$).



*Figure 2.7 Plasmalab System 100 reactive ion etching system installed in the NanoFabrication laboratory at ICFO.*

## 2.2.4    *Functionalisation of the Samples*

As explained in the first chapter, to improve the wetting properties of a particular surface and reach, for example, superhydrophobic and eventually superoleophobic states, it is necessary to increase the surface roughness and lower the surface interfacial free energy. Most of the nanostructured samples processed in this thesis have been functionalised by self-assembled monolayer coatings to modify the substrate's surface chemistry. The most commonly used coatings are fluorinated molecules, non-fluorinated polymers, alkyl molecules and silicon/silane compounds[79,80].

For inorganic substrates such as glass, silanes, which possess a hydrolytically sensitive centre and form stable covalent bonds with the substrate, are the chemicals commonly used. The reaction with the substrate of most of the organosilanes is similar. In general, these chemicals have one organic substituent and three hydrolysable substituents. The hydrolysis occurs on the three labile groups containing silanol species and, then, they condensate to form oligomers, which form a hydrogen bond with the substrate. The substrates are usually activated with plasma to create hydroxy (OH) groups and react better with the coating. During the drying or curing process, a covalent linkage is formed with a concomitant loss of water. In this work, most of the samples were functionalised with 1H-1H-2H-2H-Perfluorododecyltrichloro silane, and the trichloro groups ensured that the reactivity and the long-fluorinated alkyl chains led to better water repellence.

The method used to apply the silane was dip coating. These chemicals are typically diluted with a fluorinated solvent (Novec 7200 from 3M) in a high ratio and mixed with a magnetic stirrer. The glass substrates are activated by an oxygen plasma system (PVA TePla 300 SemiAuto from Plasma Asher) to improve the coating's adhesion to the surface and activate the OH groups. The samples are dip-coated into the solution for several minutes (depending on the coating) and cured at 50°C for a few hours. The dip-coating method usually deposits more than one layer and the last step is to rinse the substrates in the solvent in an ultrasonic bath for just 3 minutes to remove the excess material.



*Figure 2.8 PVA TePla 300 SemiAuto plasma cleaner installed in the NanoFabrication laboratory at ICFO.*

## 2.3 Characterisation Techniques

The properties and final quality of all the samples manufactured in this thesis were analysed using specific characterisation techniques. In this section, the methods and equipment used to study and evaluate the nanostructured samples are described and divided into four different categories: optical, morphological, wetting and mechanical.

### 2.3.1   *Optical Characterisation*

In the study of anti-reflective transparent surfaces, their optical properties are essential information when comparing and determining their practical characteristics. Transmission, reflection and scattering are the principal parameters used in this thesis to evaluate the performance of the developed biomimetic structures.

The total transmission and reflection were measured with spectrophotometry across the spectral UV-Visible range and up to the near-infrared for specific applications. The spectrophotometer used was the Lambda 950 from PerkinElmer (Figure 2.9), with a measurable wavelength range from 185nm to 3300nm, and pre-aligned tungsten-halogen and deuterium light sources.

Reflection measurements at normal incidence were carried out with an angle of incidence of 6°. Note that value of reflection remains essentially the same for angle of incidence up to 20°. The experimental values of one-sided reflection were calculated from the two-sided reflection, following ref [81], taking into consideration that the back surface is flat. For angular dependent measurements, the available set-up only allowed measurement of two-sided transmission (T), but not reflection (R). For this reason, the reflection values were obtained from measured transmission using the formula R=100-T, as scattering (haze) and absorption are usually low in the transparent samples of this thesis.

Scattering is another critical parameter used to characterise transparent materials, especially textured surfaces that can easily induce light dispersion. As the size of the proposed nanostructures is similar to the wavelength of the incoming light, they can deflect its straight path, making the surface less clear.
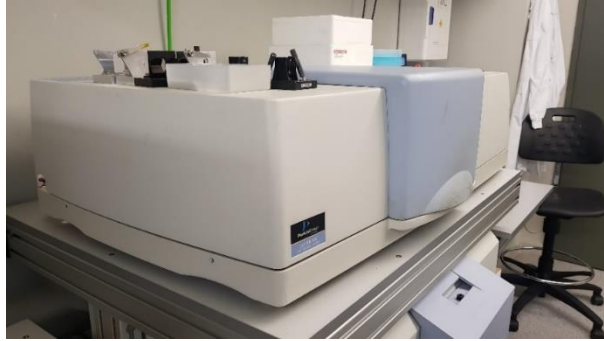
*Figure 2.9 Lambda 950 spectrophotometer installed in the Post-Processing laboratory at ICFO.*

Scattering can be quantified by haze, which is defined as the amount of light scattered or dispersed at an angle greater than 2.5° after passing through an optical surface. It should be kept as low as possible for high transmission applications, such as display screens. The WGT-S Hazemeter from Labthink Instruments Co., Ltd (Figure 2.10) was the instrument used to measure the haze in this work.
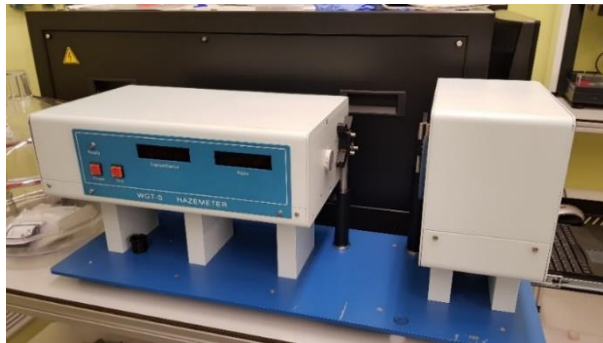


*Figure 2.10. WGT-S Hazemeter installed in the Corning laboratory.*

In the optical analysis of thin films, spectroscopic ellipsometry if often used as a sensitive technique to measure film thickness and optical constants, offering high precision and accuracy. Goniometer ellipsometer spectroscopic equipment from SOPRA with a 75W xenon lamp source (Figure 2.11) was used to obtain the refractive index and the absorption coefficient of different materials. The data extracted was added to the simulation software used for theoretical analysis and design optimisation.
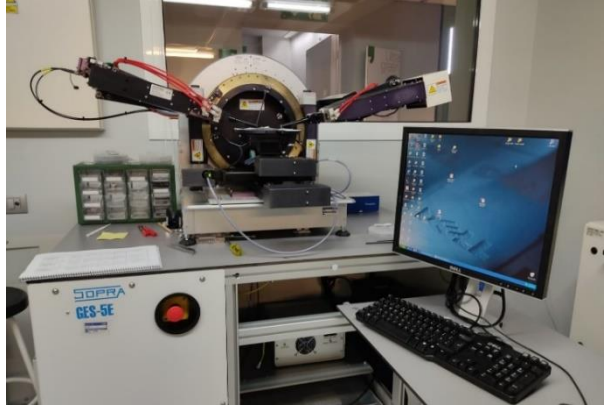
*Figure 8.11 GES5 ellipsometer spectroscopy system from SOPRA installed in the NanoCharacterisation laboratory at ICFO*

### 2.3.2    Morphological Characterisation

The analysis of optical surfaces at the nanoscale requires extremely accurate topographic characterisation techniques. Scanning electron microscopy (SEM), atomic force microscopy (AFM) and a profilometer were used to determine the thicknesses of films, and the shape and density of the developed nanostructures.

Most of the fabrication processes proposed in this thesis include sputtering deposition of ultra-thin metal films, from 2nm to 20nm. Characterisation of the deposition rate of all the sputtered materials (Cu, Ni, Ag, ITO, $TiO_2$, $SiO_2$) was conducted with an atomic force microscope system (Veeco Dimension 3100 from BRUKER - Figure 2.12). The thickness and roughness of multiple depositions were characterised with high precision during optimisation of the fabrication processes. The system measures the mechanical frequency change of an oscillating micron-scale cantilever with a very sharp conical tip that approaches the surface of the films. Although the AFM has an accuracy of nanometres, the system was limited to studying thin films, because, with nanostructures, the tip could not reach the bottom part of the structures due to its geometry and dimensions.
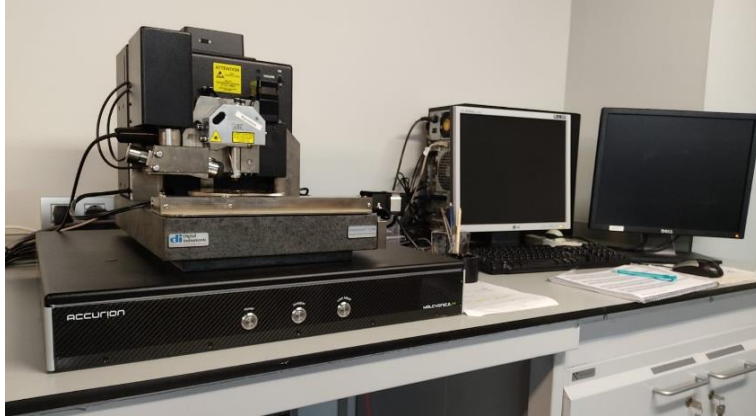
*Figure 2.12 Atomic force microscope Veeco Dimension 3100 from BRUKER installed in the NanoCharacterisation laboratory at ICFO*

Scanning electron microscopy was used to analyse the morphology, topography and defects of dewetted nanoparticles and nanostructured surfaces. This system focuses an electron beam over the surface and from the reflected signal measured by various detectors, the machine can process and create an image of the examined surface. Top view and cross-section images were taken to determine the distribution and geometry of the particles and structures with high precision, and these were used to optimise steps like the dewetting and the reactive ion etching. The SEM used was the Inspect F from FEI (Figure 2.13).



*Figure 9 Scanning electron microscope Inspect F from FEI installed in the NanoFabrication laboratory at ICFO*

For thin film characterisation, the profilometer is another useful tool that can provide quick measurements of the surface profile of a particular area. It is commonly used to measure the step height of a coated area, i.e., the curvature or the roughness of a surface. The Tencor Stylus Alpha-step from KLA (Figure 2.14) uses a stylus that is directly in contact with the surface, which operates with an optical lever sensor for high-resolution measurements. This equipment was mainly used for thin films (thickness < 50nm).



*Figure 2.14 Tencor Stylus Alpha-Step profilometer from KLA installed in the NanoFabrication laboratory at ICFO*

### 2.3.3 *Wetting Characterisation*

The self-cleaning capabilities of a sample can be determined by measuring the contact angle (CA) between the surface and different liquid droplets. As well as the static contact angle, it is also important to study the dynamic contact angles, i.e., the advancing, the receding and the hysteresis CAs. Together with the sliding angle, these values determine the ability of the studied droplet to "roll-off" the surface.

In this thesis, a droplet shape analyser (DSA100, KRÜSS) (Figure 2.15) was used for measuring the wetting properties of bare and nanostructured materials. This equipment uses a 0.5mm needle to precisely deposit 0.1µl small droplets of water and other liquids on top of the studied surface. The sample holder can rotate 90 degrees to analyse dynamic CA measurements, and the software provides images and videos of the contact angle calculations with a high-resolution camera.
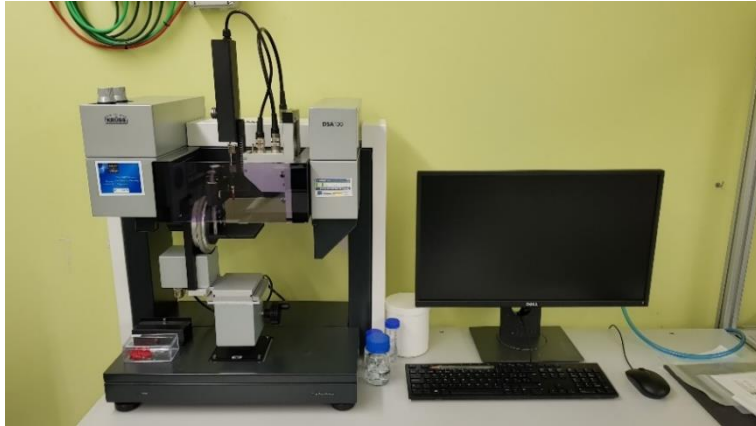
*Figure 2.15 Droplet shape analyser DSA100 installed in the Corning laboratory*

### 2.3.4    *Mechanical Resistance*

For practical applications, standard equipment and procedures were used to characterise the mechanical resistance and durability of the developed nanostructured surfaces, and, in addition, climatic tests were performed to analyse the resistance of the coatings.



*Figure 2.16 M238BB crockmeter installed in the Corning laboratory.*

In this thesis, the crockmeter test was used as a standard and reproducible evaluation system to determine and compare the mechanical durability of the studied surfaces. The crockmeter (M238BB, SDLATLAS) (Figure 2.16) emulates the action of a human finger and signals any wear or damage, making it relevant for display screen applications. It uses a constant force of 9N over a 2cm$^2$ area applied through a standard rubbing material (microfiber cloth). The test was performed for more than 1000 wiping repetitions, and optically and

morphologically analysed before and after the test to determine the resistance of the structures. The crockmeter test method was originally designed to determine how much colour transferred from a textile material to other surfaces by rubbing, but recently, it has been found to be useful for optical surfaces.

The ability of a surface to withstand extreme weather conditions has also been studied in this thesis as this is vital for outdoor applications. A weathering test (described in detail in Chapter 3) was performed to determine the resistance of different coatings in high moisture, UV exposure and high temperature conditions. A climatic chamber (VCL 7003 from Vötsch Industrietechnik GmbH) (Figure 2.17) was used to simulate different environmental conditions, controlling parameters such as temperature, humidity and pressure. An ad-hoc setup was built to combine a UV lamp (VL-115.c from VILBER) and a hot plate (Fisherbrand™) to emulate UV light exposure with high temperatures.



*Figure 2.17 Climatic chamber installed in the Post-Processing laboratory at ICFO*

## 2.4 Modelling Nature's Designs

Computer science has become a powerful tool for saving time and resources when conducting experiments. Running models and simulations allows for trends or patterns to be identified, and assists with understanding the theory behind the experiments and quickly optimising a proposed structure to obtain the best performance depending on the application. Finite element method commercial software (COMSOL Multiphysics®) was used to perform electromagnetic simulations in this thesis.

For thin film characterisation and multilayer coating design optimisation, 2D simulations were used. The nanostructured patterns proposed in this thesis were 3D-modelled to study and optimise the geometry of the structures for optimal optical results. Although most of the patterned arrays are not periodic, the proposed structures were studied using periodic boundary conditions to optimise the simulation processing time, and the experimental results matched well with the calculations.

## 2.5 Conclusions

This chapter has described most of the fabrication and characterisation techniques utilised in this thesis towards the development of nanostructured transparent surfaces. The procedures and instruments used in this work combine solutions that have been already implemented in the optical surfaces industry, together with new alternatives that look to be cost-effective for large-area processing and have enough resolution to compete with other techniques based on expensive and time-consuming optical and e-beam lithography systems.

The methods investigated are based on the deposition of thin films via sputtering, solid-state thermal dewetting using rapid thermal annealing processes, and chemical and dry etching techniques. All of these have been described and optimised in each chapter of this thesis.

The enhanced optical and wetting characteristics of the proposed structures were studied through various characterisation procedures. Spectroscopy was used to measure light interaction with the studied surfaces, evaluating the total transmission and reflection. The scattering of the samples was measured with a hazemeter, analysing the clarity of the materials processed. The wetting properties were characterised with a drop shape analyser, where the static

and dynamic water contact angles were measured to analyse the wettability of the proposed surfaces.

The structural morphology of the films and nanostructured surfaces were studied in detail with AFM, profilometry and SEM techniques. The deposition and etching rates of different processes, the thickness of thin films, and the geometry of the nanostructures created on different materials were analysed with these techniques to characterise the fabrication methods and the resulting samples.

The proposed structures were also analysed for mechanical resistance against external agents. Different standardised tests, such as the crockmeter and weathering tests, were used to study the mechanical durability of the nanostructures and the coatings used to functionalise the surfaces.

Powerful software tools were used in the design and optimisation processes of all the structures proposed in this work. COMSOL Multiphysics® was the program used to perform parametric simulations, which saved time and optimised the search for the best parameters for optimal optical results, from multilayer designs to the geometry of the nanostructures.

# 3

# Anti-reflective and Self-Cleaning Nanostructured Glass

## 3.1 Introduction

Glass has been produced for thousands of years and today it is one of the most widely used materials by humans. This non-crystalline amorphous solid has become a lucrative material for multiple applications due to its unique characteristics, such as chemical resistance, high transmission and significant mechanical strength. The construction, solar, and automotive industries are leading the growth in the flat glass market, which was expected to reach USD 119.7 billion during 2020, with a forecast of 5% annual growth until 2026[81].

For optical components and optoelectronic devices, there is a broad range of transparent substrates, such as quartz, dielectric crystals or organic polymers. However, glass is still the preferred choice when high transparency is required. It appears to be the most suitable material for the majority of applications due to unique attributes, easy tunability for different requirements and low cost. Other alternatives to glass are more expensive or have worse optical properties.

Most electronic devices need transparent covers that protect their surface from contamination or damage (e.g., display screens or solar cells). These

transparent protectors are typically made of glass or plastics. However, the high surface reflectivity of such covers has a negative impact on the optical performance. At normal incidence, the average reflection loss is more than 4% at each surface and this increases with larger angles of incidence (AOI). This might seem a small value, but these reflections can manifest as glare and make it difficult to see the intended information on the display or reduce the efficiency of a solar cell.

As discussed in the previous chapter, based on the cancellation of multiple interferences, multilayer coatings are the most popular commercially available anti-reflective (AR) solutions[25–27,82]. However, these structures suffer from several disadvantages including narrowband wavelength and AOI operation, thermal expansion mismatch, poor substrate adhesion, and sensitivity to thickness variations. Designs for multifunctional nanostructured surfaces inspired by nature are emerging as a possible solution to improve the optical properties of transparent surfaces and to add new functionalities, such as omnidirectional antireflection, low haze, superhydrophobicity and oleophobicity, in addition to moderate mechanical resistance[1,24,53,62].

One of the most significant challenges with biomimetic surfaces is to find scalable fabrication techniques. Although very precise, developing such elaborate and small structures with expensive lithography processes is time-consuming and cannot process large surfaces, making it costly and, thus, not feasible for industrialisation. Finding new ways to create these structures has become the target of many research groups and is one of the main motivations of this thesis.

In this chapter, tapered nanopillars on glass substrates are presented as a possible solution, having significant AR and self-cleaning performance.  The method used to create such structures is based on the formation of large-scale nanosized etching mask patterns. The technique includes a thermal dewetting process[72,73,83], which is cost-effective, scalable, and does not require any lithographic step. The process can be tuned to obtain different particle size and density, which permits optimisation of the final structures for various applications.

## 3.2 Fabrication

Novel strategies to produce AR and self-cleaning substrates have been introduced in recent years. In this chapter, a novel method to create nanopillars, which combines scalable techniques, is proposed and represented in Figure 3.1.
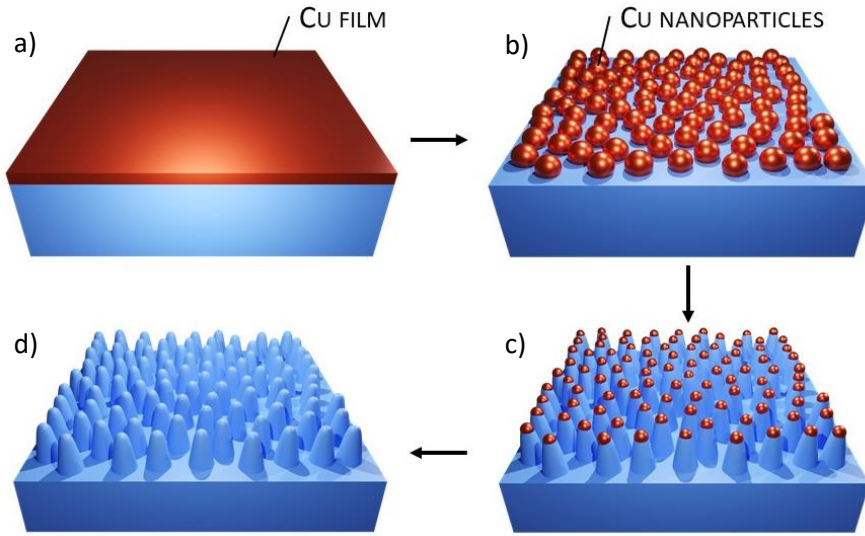


*Figure 3.1 Nanostructure fabrication process. The initial ultra-thin copper (Cu) film is deposited on top of the glass substrate by sputtering (a) and thermally dewetted into Cu nano-islands (b). These nanoparticles are used in a dry etching process as a metal nanomask to transfer its pattern to the glass substrate (c). The final step consists of removing the residual Cu (d).*

This work has been conducted with Corning® chemically strengthened glass with a thickness of 0.7mm and an area of 5cm square. Initially, the samples were cleaned in acetone followed by ethanol in an ultrasonic bath for 10 minutes each. The substrates were then rinsed in deionised water and dried with nitrogen ($N_2$), which was followed by an oxygen ($O_2$) plasma cleaning process (PVA TePla 300 SemiAuto Plasma Asher) for 10 minutes with 300ml/min of $O_2$ and 700W of power. After the preparation and cleaning of the samples, an ultra-thin metal film of copper (Cu) was deposited using a magnetron sputtering system (ATC Orion 8m, AJA International, Inc.) – Figure 3.1(a). The deposition was performed at a base pressure of $10^{-8}$ Torr, room temperature, 100W of DC-power and 25 standard cubic centimetres (sccm) of pure argon. The working pressure was $1.5 \times 10^{-3}$Torr, the deposition rate of Cu was 0.166nm/s, and the target-substrate distance was 40cm. All of these

parameters were calibrated to obtain a uniform and continuous ultra-thin Cu film and, then, the coated samples were introduced into a rapid thermal annealing oven (TsunamiTM RTP-600S) to dewet into nanoparticles – Figure 3.1(b). The substrates were rapidly heated at a temperature of 600°C for 135 seconds in a high purity $N_2$ atmosphere to prevent oxidation. Under these conditions, the dewetting phenomenon occurs because the thin film's surface energy is greater than the interfacial and surface energy of the underlying substrate. By modifying the initial thin film thickness, the temperature of the process, and the time exposed, it is possible to control the size and distribution of the agglomerated 3D nano-islands. Full optimisation of the process was performed to control this step. The resulting metallic nanoparticles were used as an etching mask during a dry etching process – Figure 3.1(c). With a reactive ion etching system (Plasmalab System 100, Oxford Instruments), the shape of the particles was transferred to the glass surface, and the height of the resulting nanopillars was defined by the processing times. The etching parameters were 300W RF power (875DCV) at 10mTorr in 40sccm Ar/5sccm CHF3 plasma. After the etching process, the residual mask was chemically removed with ammonium persulfate. Finally, the samples were ultrasonically cleaned in acetone, ethanol and deionized (DI) water for 10 minutes each and dried by blowing $N_2$ over the surface – Figure 3.1(d).

## 3.3 Simulation

In this section, a full optimisation study was performed to theoretically understand the optical effect of different parameters, such as the shape, the size, and the density of the nanostructures. After learning the fabrication limits of this technology, numerical calculations were performed to identify the best possible designs among all the existing solutions. The results obtained with simulations were also validated experimentally and used to study some of the proposed structure's optical properties.

The modelled structure is shown in Figure 3.2 and consists of a square cell with a central pillar. The parameters used to define the structure are the period (P), the base diameter ($D_{BASE}$), the apex diameter ($D_{APEX}$) and the height (H) (Figure 3.3). The nanostructured samples were simulated using periodic boundary conditions, and the glass manufacturer provided the refractive index used in all the calculations. The values used in the parametric simulations in the following sections were extracted from previous scanning electron microscopy (SEM) analysis during the manufacturing optimisation.
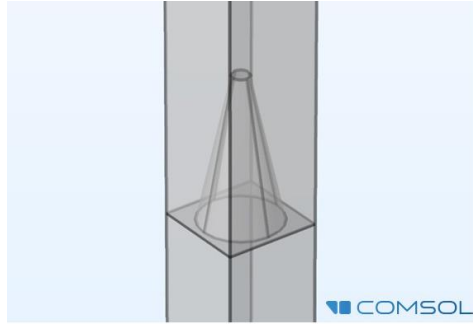
*Figure 3.2 3D model of the proposed structure, simulated with COMSOL Multiphysics® software. A central pillar in a square cell was defined with the parameters shown in Figure 3.3, and the structure was studied using periodic boundary conditions.*
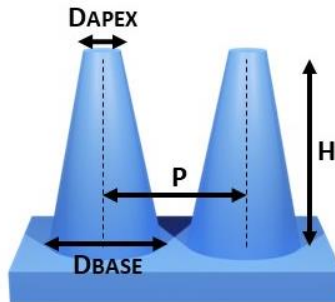


*Figure 3.3 Parameters used to define the geometry of the studied structures*

## 3.4 Optimisation

The fabrication process conditions were defined after an optimisation study. In order to control the final geometry of the structures, it is crucial to understand the effects of all the parameters involved in the fabrication. Among all the variables associated with this method, certain parameters are essential to define the shape, the density and the size of the resulting nanopillars.

The initial film thickness and the material used as a mask are defined at the beginning of the process. When choosing the material, two major factors have to be taken into account, firstly, the ease of creating nanoparticles during the dewetting process, and, secondly, the etching rate compared with the substrate under the same dry etching conditions. For the chemically

strengthened glass (Corning® Gorilla® Glass), Cu was found to be the best choice. It can dewet into spherical particles with the appropriate size and density at temperatures below the substrate's strain point. Also, the etching rate allows to create pillars of more than 400nm height, which is far more than is needed for applications working in the visible and near-infrared regions.

The average size and distribution of the resulting metal nanoparticles from the dewetting step can be moderately controlled by the thickness of the initial ultra-thin metal film. Each thickness has an optimal dewetting temperature and process duration, and theoretical analyses with simulations helped to find the desired particle size and distribution for optimal optical results. An SEM inspection was conducted to measure the average particle density and diameter after dewetting different thin films of Cu on Corning® Gorilla® Glass substrates. Table 3.1 shows data extracted from the SEM images (Figure 3.4) with the software ImageJ, an open-source image processing program.

*Table 3.1 Data extracted from a scanning electron microscopy analysis of different samples after the dewetting process (Figure 3.4).*

| Initial metal thickness (nm) | Average particle density (#Particles/$\mu m^2$) | Average particle diameter (nm) |
|---|---|---|
| 4 | 41 ± 4 | 60 ± 16 |
| 6 | 36 ± 5 | 75 ± 25 |
| 8 | 26 ± 7 | 95 ± 18 |
| 10 | 12 ± 2 | 142 ± 35 |
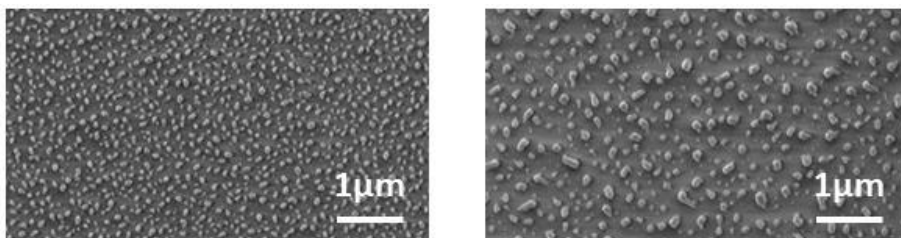


*Figure 3.4 Images from a scanning electron microscopy analysis of Cu nanoparticles after a single dewetting process. Thinner initial Cu films (6nm) form smaller and denser nanoparticle arrays (left) compared with thicker initial Cu films (10nm) (right).*

Figure 3.5 shows that thinner initial films lead to smaller particle size and higher density, while thicker initial films produce bigger particles with lower

density. The results can vary depending on surface conditions and cleaning before metal deposition.
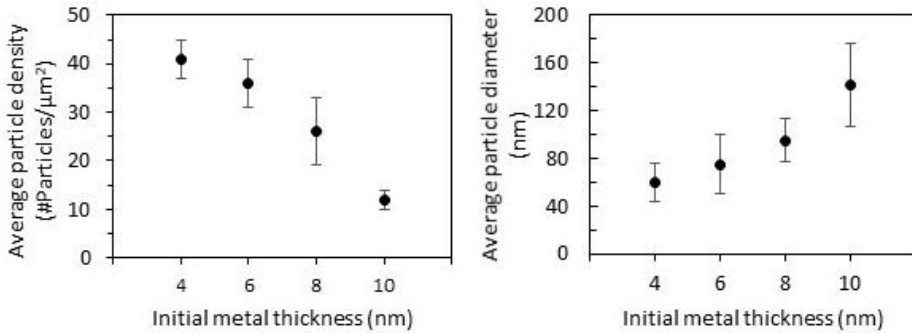


*Figure 3.5 Average particle density (left) and particle diameter (right) versus the initial copper film after the dewetting process (data from Table 3.1).*

The metallic nanoparticle array generated by the dewetting step (Figure 3.1(b)) is used as a mask during the patterning process (Figure 3.1(c)). By modifying the pressure, the power, and the gases involved, it is possible to adjust the selectivity of the etching process. For instance, high selectivity is required to generate perfect straight nanopillars, guaranteeing practically the same nanoparticle diameter during the etching process. For nanopillars with conical shapes, however, lower selectivity is required, and the Cu nanoparticles have to be etched as well but at a lower rate than the substrate material (Figure 3.6).
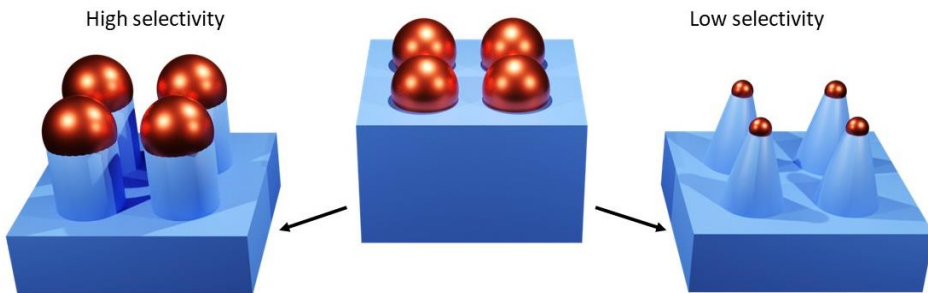


*Figure 3.6 Cylindrical (left) and conical (right) pillar structures after high and low selectivity etching processes, respectively, for the same initial Cu nanoparticle array (central).*

A parametric simulation was performed to evaluate multiple structural designs, and the results are represented in Figure 3.7 and Figure 3.8. The variables studied were the apex diameter ($D_{APEX}$), the period (P) and the height, fixing the base diameter to 140nm as a starting point (from previous SEM

analysis). The $D_{APEX}$ parameter defines the structure's shape, from cylindrical ($D_{APEX}$ = 140nm) to conical ($D_{APEX}$ = 0nm) nanopillars. The period determines the final structure's density, the highest density being 140nm as the bases of the nanopillars were touching each other. The heights studied were from 100 to 300nm as the structure was optimised for the visible region. The reflection values plotted for each combination of parameters are the average reflection calculated for three different wavelengths: 400, 550 and 700nm. Only one surface was considered in the study, the maximum reflection of the substrate being 4% approximately.

Figure 3.8 shows the AR effect of different structures using some of the optimal parameters extracted from Figure 3.7. From these theoretical results, one can see that the best AR performance in the visible region is obtained with densely packed conical nanopillars, which induces a smooth refractive index from the air to the substrate material. The optimal optical results were obtained with small $D_{APEX}$ values (20-50nm), pillar heights between 225 and 275nm, and periods close to the structures' base diameter.
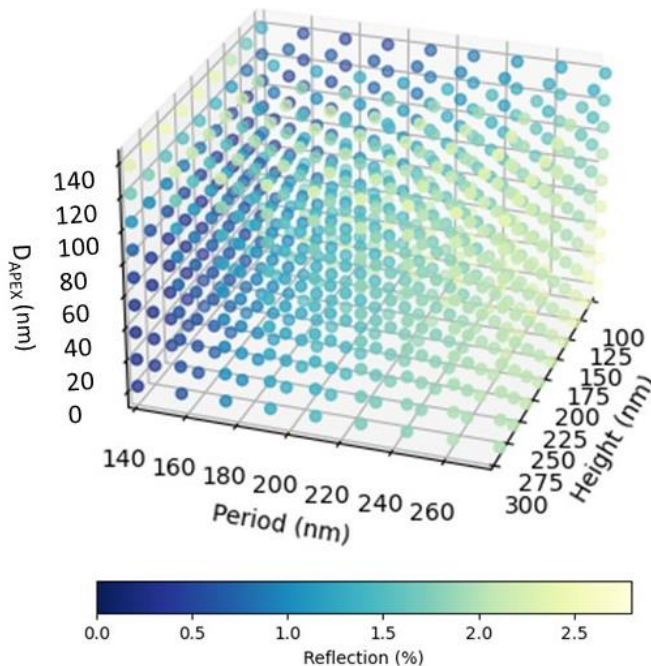


*Figure 3.7 Nanostructure parametric simulation. The average reflection was calculated in the visible region (400-700nm) for different combinations of geometrical parameters.*
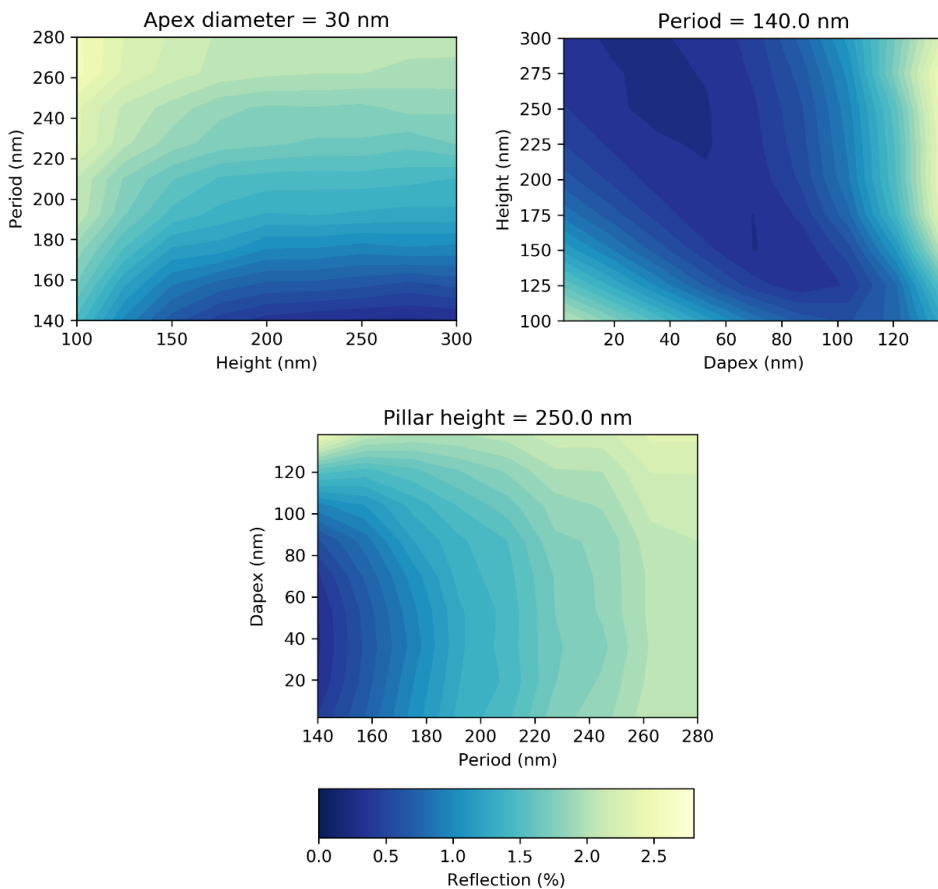
*Figure 3.8. Simulated average reflection in the visible range (400-700nm) for different parametric combinations. The lowest reflection was obtained for small DAPEX values (20-50nm), a high density of nanopillars (P=140nm) and heights between 225-275nm.*

The duration of the etching process (Figure 3.1(c)) determines the final height of the nanopillars. A set of samples was prepared with the same film thickness and dewetting process to evaluate this effect. The structure resulting from a thickness of 6nm and a temperature of 600°C was found to match well with the optimal results from the previous parametric simulation. As Table 3.2 indicates, longer etching processes produce taller nanopillars, displacing the optimal AR effect to the near-infrared region (Figure 3.9), and increasing the scattering at shorter wavelengths (Figure 3.10).

*Table 3.2 Fabrication variables for test samples and the height of the average pillar measured with a scanning electron microscope.*

| Sample | Cu Film (nm) | RTP (°C) | RIE (min) | Pillar Height (nm) |
|--------|-------------|----------|-----------|-------------------|
| 6' RIE | | | 6 | 170 |
| 7' RIE | | | 7 | 195 |
| 8' RIE | 6 | 600 | 8 | 220 |
| 9' RIE | | | 9 | 252 |
| 10' RIE | | | 10 | 278 |
| 11' RIE | | | 11 | 304 |
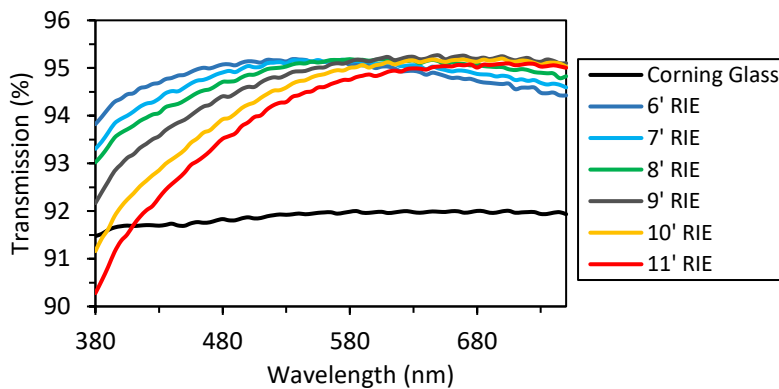


*Figure 3.9. Measured direct transmission of single-sided nanostructured samples with different nanopillar heights. The reactive ion etching (RIE) time (in minutes) defines the size of the structures.*
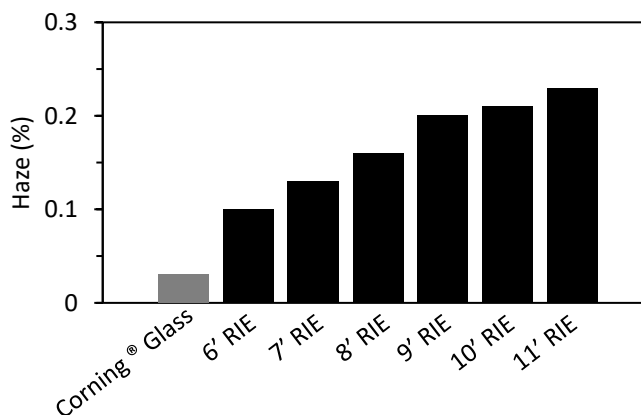


*Figure 3.10. Haze measurements for the samples plotted in Figure 3.9. Longer reactive ion etching (RIE) times (in minutes) create larger nanopillars, increasing the scattering.*

Nanostructured samples were fabricated with optimal parameters obtained from the simulation study, as shown in the SEM image in Figure 3.11(b). Conical nanopillars, densely packed and around 250nm in height, showed good agreement with the optical results obtained with simulations even for different AOIs (Figure 3.11(a)).
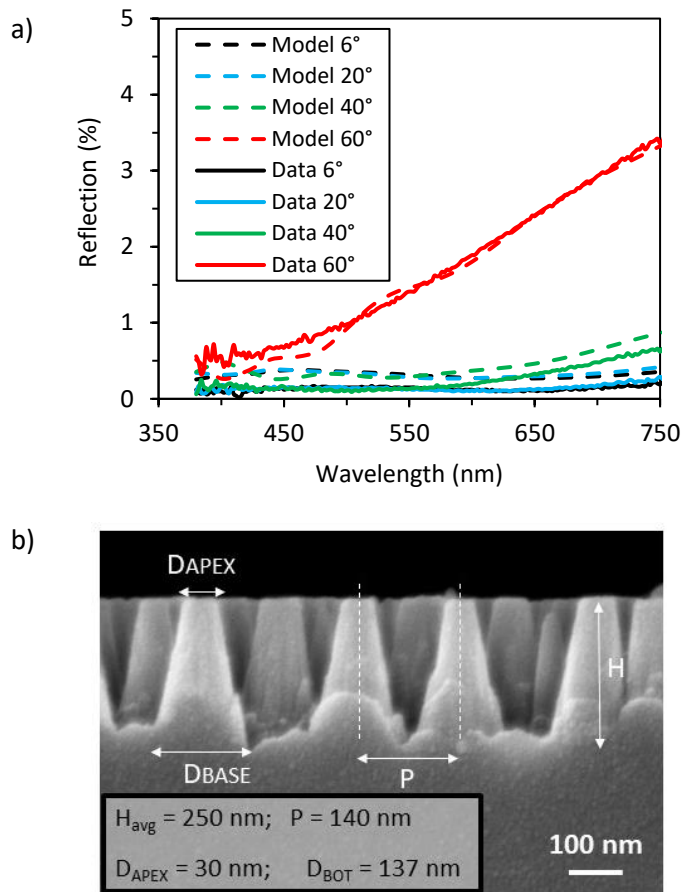


*Figure 3.11 Reflection comparison of a typical sample between the simulation model (dashed lines) and experimental data (solid lines) results for different angles of incidence (a). Only the front side was considered for comparison. The geometric values were extracted from a scanning electron microscopy analysis of the measured sample (b).*

## 3.5 Experimental Results

### 3.5.1 *Optical Performance - Visible*

Transparent AR surfaces could be widely used in many industrial applications. The overall optical and optoelectronic performance of a device can be enhanced by improving the transmission, reducing the reflection, and if high clarity is demanded, minimising the scattering values. The optical properties of these single-sided structured samples were investigated by measurements of wavelength-dependent transmission and reflectance. The scattering was also considered, as this quantifies the incident light diffused by the sample, and, thereby, its clarity. As a reference, an unstructured glass substrate (denoted by "bare" or "Corning® Glass") was measured too. The fabrication variables for nanostructured glass (NS Glass) with optimal optical properties in the visible range are shown in Table 3.3. In the simulations, the optimal AR effect was obtained with 225-275nm pillars, but, experimentally, it was found that such heights caused undesirable scattering due to the closer similarity with the incident light wavelength. Thus, shorter conical nanopillars (~170nm) were fabricated, maintaining excellent AR effect with higher clarity.

*Table 3.3 Variables used to fabricate nanopillars on Corning® Glass with optimal AR performance in the visible range.*

| Sample | Cu Film (nm) | RTP (°C) | RIE (min) | $D_{BASE}$ (nm) | $D_{APEX}$ (nm) | Pillar Height (nm) |
|---|---|---|---|---|---|---|
| NS Glass | 6 | 600 | 6 | 130 | 35 | 170 |

Figure 3.12 shows the measured total transmission and reflection of the proposed structure with respect to the bare glass. The nanopillar array clearly induces AR properties, reducing the reflection to almost 4% over the spectrum's whole visible region. Note that only one surface was treated in this experiment, so the minimum reflectivity that can be achieved corresponds to the sample's back flat surface (around 4%). High transmission can be achieved, and by controlling the size of the pillars, the haze values can be kept close to 0.1%, which is the reference limit for applications demanding high clarity surfaces (e.g., display screens or lenses). The haze parameter is the percentage of incident light diffused at an angle larger than 2.5° and quantifies the scattering induced by a sample. When the nanopillars have subwavelength dimension, light scattering becomes almost negligible, thus preserving the directionality of the transmitted beams.
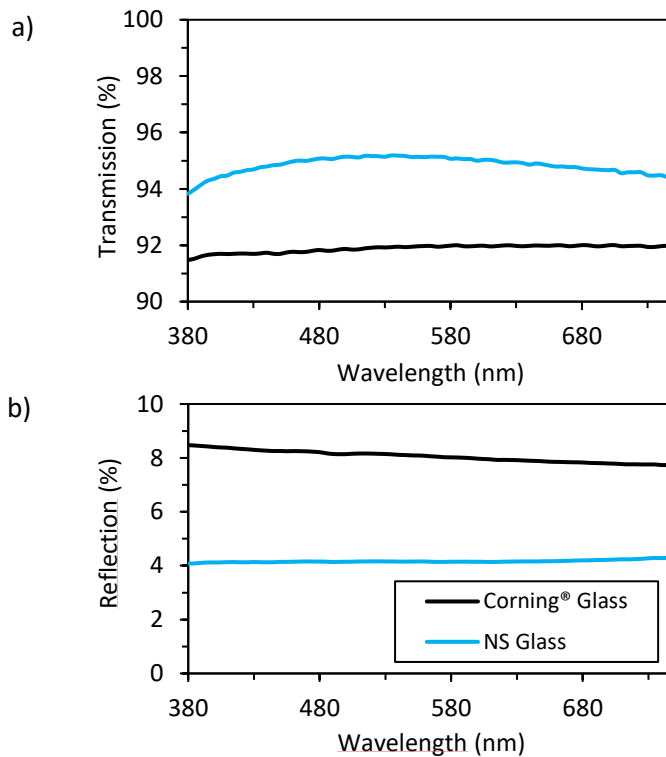
*Figure 3.12 Measured total transmission (a) and reflection (b) in the visible region (380-780) for one-sided nanostructured glass (NS Glass) compared with a bare substrate (Corning® Glass).*

In Figure 3.13, the comparison between a one-sided nanostructured sample and bare glass is shown. The AR effect created by the nanopillars can be seen with the naked eye.
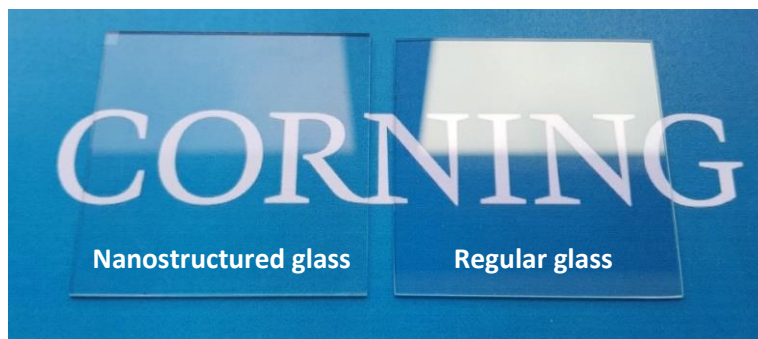


*Figure 3.13 Comparison between one-sided nanostructured glass and regular glass.*

For porous or patterned surfaces, the refractive index of the structured layer is dependent on the volume fraction between air and the created protuberances, and the effective medium theory can be used to calculate the AR effect. In this particular case, conical nanopillars (Figure 3.14) produce a refractive index gradient, making the transition from the air (low-refractive-index medium) to the glass substrate (high-refractive-index medium) smoother, and, thus, improving the AR characteristics.
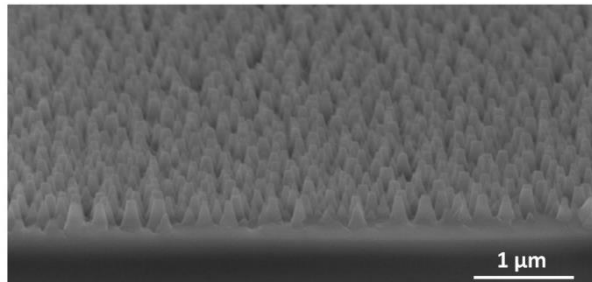


*Figure 3.14 Scanning electron microscope image of the proposed nanostructured glass surface*

Simulations were also used to theoretically compare the proposed structure with typical AR multilayer coating designs based on intercalated silicon dioxide ($SiO_2$) and titanium dioxide ($TiO_2$) optimised for the visible region. The reflectance was calculated for unpolarised light from 380 to 780nm and with different AOIs. Figure 3.15 shows how the smooth refractive index gradient produced by the conical nanostructures generates a flatter response with a broadband AR effect.
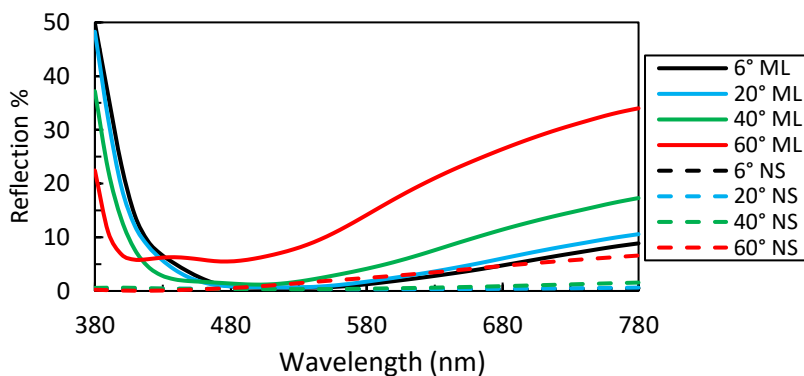


*Figure 3.15 Simulated AR effect of an AR multilayer coating (ML) and the optimised nanostructured sample (NS). The reflectance was calculated in the visible range (380-780nm) and for different AOIs. Only one side was considered. The refractive indices used to simulate the ML coating were extracted from the refractiveindex.info database.*

A commercially available AR multilayer coating optimised to operate in the visible region was experimentally compared with the proposed structure by measuring the reflection (Figure 3.16). The samples were measured for different AOIs and showed good correlation with the simulation results (Figure 3.15). As can be seen, the sample with nanopillars presents outstanding performance for large AOIs, keeping the reflection below 0.5% even for 40°. The multilayer coating instead shows much larger (3%) reflectivity under the same conditions.
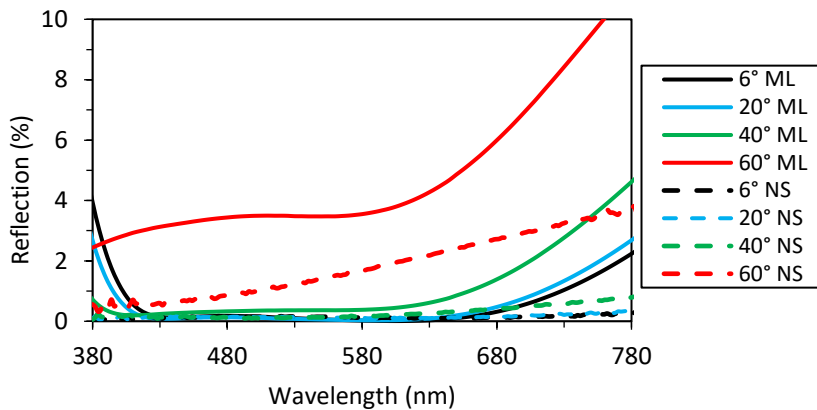


*Figure 3.16 Measured reflection for different angles of incidence (AOI). Only the front side was considered for comparison between the AR multilayer coating (ML) and the AR nanostructures (NS).*

The nanostructured sample curves are flatter throughout all the frequency bands, and for larger AOIs, the improvement becomes even more significant. These results show the excellent AR effect created by conical nanopillars, overcoming some of the main drawbacks of multilayer coatings (e.g., the narrowband operation and poor response at high AOIs).

### 3.5.2   *Optical Performance - Near-Infrared*

The proposed structure is versatile and can be applied to a large variety of optoelectronic devices. Samples optimised for another wavelength range were fabricated to demonstrate the tunability of the process. Light detection and ranging (LIDAR) systems use light to map the terrain and can act as the "eyes" of autonomous vehicles[84,85]. The system emits thousands of laser pulses that collide with surrounding objects and reflect back, generating a 3D image. Current state-of-the-art LIDAR systems operate in two wavelengths:

905 and 1550nm. For this particular application, taller nanostructures (Table 3.4) were fabricated and optimised to reduce the reflection in the wavelength range 600-1300nm.

*Table 3.4. Fabrication variables of the optimised nanostructured samples for the near-infrared (NIR) region.*

| Sample | Cu Film (nm) | RTP (°C) | RIE (min) | $D_{BASE}$ (nm) | $D_{APEX}$ (nm) | Pillar Height (nm) |
|--------|--------------|----------|-----------|-----------------|-----------------|---------------------|
| NS NIR | 8 | 600 | 19 | 150 | 15 | 390 |

The thickness of the initial thin film was increased to 8nm in order to obtain bigger nanoparticles, while the annealing temperature and the time of exposure were kept the same. As shown in the SEM analysis in Figure 3.17, the structure is still dense but with taller and sharper nanopillars, as the etching process time was increased.
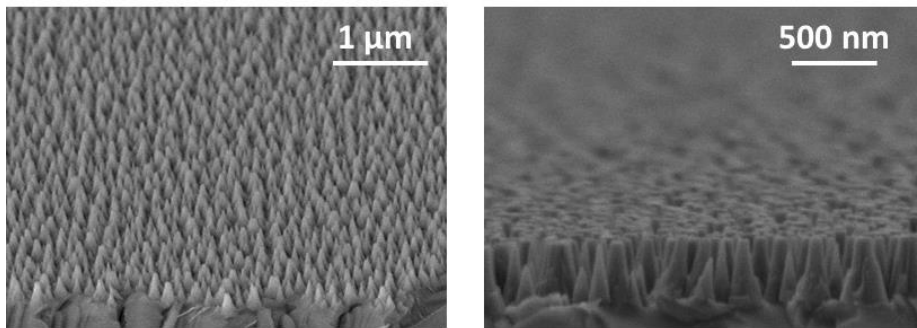


*Figure 3.17 Scanning electron microscope images of the optimised sample for the near-infrared region, showing taller nanopillars.*

Figure 3.18 shows the total transmission of the optimised sample for the near-infrared region with taller nanopillars (H = 390nm). The optical performance is significantly improved in the near-infrared range compared with the bare substrate (Corning® Glass). However, due to the scattering at shorter wavelengths, the transmission values drop drastically in the visible range.
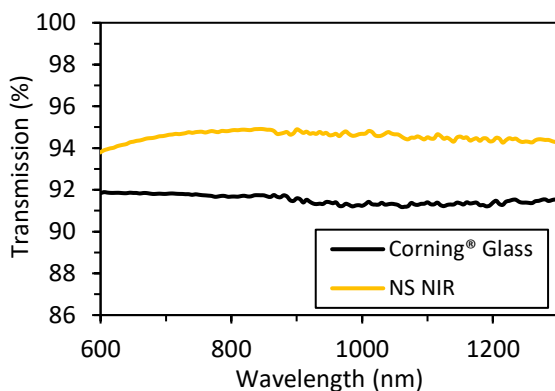
*Figure 3.18. Measured total transmission in the visible and near-infrared regions for a single-sided nanostructured glass sample with tall nanopillars (H=390nm). Bare substrate (Corning® Glass) serves as a reference.*

### 3.5.3 *Wetting Performance*

Nanostructured glass samples exhibit a superhydrophilic and lipophilic behaviour right after the fabrication process. This phenomenon can be explained by the intrinsic hydrophilicity and lipophilicity of the glass. As mentioned in the first chapter, a textured surface presents enhanced wetting characteristics as the total area in contact with the liquid increases[54]. With this particular structure, right after the fabrication process, superhydrophilicity can be achieved.

The performance can be fully transformed by coating the surface with a low free energy self-assembled monolayer (SAM). The best wetting performance was obtained using fluorine-containing silanes, which have extraordinary water repellent properties and stability[80]. Table 3.5 shows the wetting characterisation of a functionalised nanostructured sample compared with a bare substrate. High static contact angles (CA>150°) and low contact angle hysteresis (CAH<10°) were obtained, indicating potential for self-cleaning capabilities.

The method used to functionalise the samples followed the same procedure explained in chapter two. 1H,1H,2H,2H-Perfluorododecyltrichlorosilane came as a powder, and was dissolved in NOVEC 7200 with a weight ratio of 1:1000. The glass surface was activated with an $O_2$ plasma treatment to enhance the bonding of the SAM coating to the substrate. The samples were dip-coated for 3 minutes and cured at 50°C for two hours in a convection oven. Finally, to

remove the excess layers, the samples were ultrasonically cleaned in a NOVEC 7200 bath for 2 minutes.

*Table 3.5 Wetting properties of an optimised nanostructured (NS) glass sample for the visible region after a superhydrophobic fluorosilane treatment. The wetting properties of bare glass were measured for comparison.*

| Sample | Static CA (°) | Sliding Angle (°) | Advancing CA (°) | Receding CA (°) | Hysteresis CA (°) |
|---|---|---|---|---|---|
| Corning® glass | 40 | 50 | 37 | 17 | 19 |
| NS glass | 150 | 3 | 152 | 146,4 | 5,6 |



*Figure 3.19 The water contact angle (CA) measurements were performed with a drop shape analyser, where multiple droplets with the same volume could be deposited in a controlled manner on the sample's surface (a). Image of a droplet of 7ul used to calculate the static CA (b).*

### 3.5.4   *Mechanical Resistance Test*

In most industries, mechanical resistance tests are essential parts of the design and manufacturing process of products. From validating the required properties to evaluating the safety or maximum resistance until failure, the information extracted from these tests is crucial for the research and engineering teams.

In order to compare results or establish safety regulations depending on the application, organisations like the American Society for Testing and Materials (ASTM) provide standard guidelines to unify the tests that determine how resistant a material or structure is. For instance, the display screens industry, especially with regard to touch screens, has severe tests that have to be passed before a product can be approved for industrialisation. These include a crockmeter test, steel-wood wear test and drop test.

For micro- and nanostructured surfaces, the standardised wear and abrasion tests are performed with a crockmeter. The method is designed to simulate the action of a human finger with a constant load pressure of 4,5N/cm². It can repeat the swiping effect thousands of times and with different rubber materials. In this work, microfibre standard crockmeter test cloth and microfibre eyeglass cleaning cloth were used.

Figure 3.20 shows a nanostructured sample (fabricated following the parameters in Table 3.3) before and after 1000 runs of the crockmeter test using a microfibre standard crockmeter cloth. Visible scratches and wear could be seen with the naked eye, and the optical and wetting properties were affected by a reduction in transmission and the superhydrophobic properties (Table 3.6).
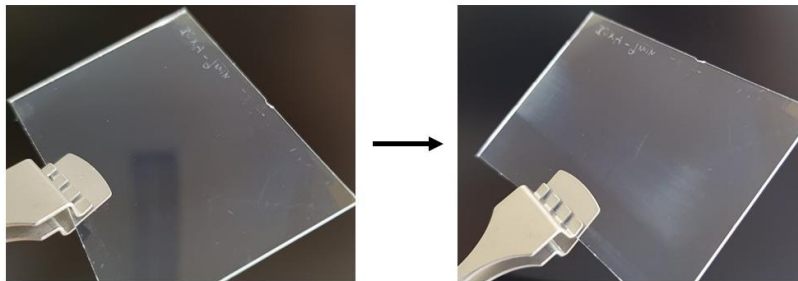


*Figure 3.20 Nanostructured samples before (left) and after (right) the crockmeter test with a standard microfibre cloth. Cloth residues are visible where the crockmeter was performed.*

*Table 3.6. Optical and wetting properties before and after the crockmeter test.*

| Sample | Before Crockmeter | After Crockmeter | O₂ plasma cleaning | Functionalization with SAM silane |
|---|---|---|---|---|
| Transmission (%) | 95,1 | 94,8 | 95 | 95,0 |
| Haze (%) | 0,09 | 0,45 | 0,09 | 0,10 |
| Water CA (°) | 150 | 125 | 4 | 150 |

The surfaces were examined with a scanning electron microscope (SEM) to characterise any damage at the nanometric scale. As shown in Figure 3.21, the SEM images reveal that the nanopillars withstood the crockmeter test with no significant physical damage. However, cloth residues were found in between the pillars on the nanostructure. Some micro-scratches due to hard particles

trapped between the cloth and the surface were also found, but these were not visible to the naked eye and they did not affect the optical performance.
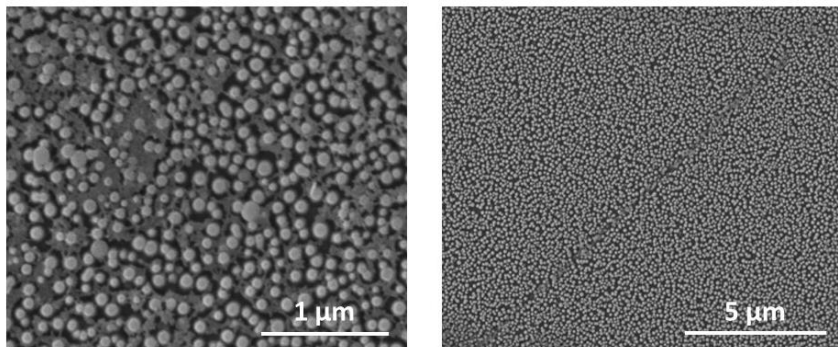


*Figure 3.21 Scanning electron microscope images after the crockmeter test. The optimised nanostructures (H= 170nm) withstood the wear test, but cloth remains were found between the nanopillars (left). Micro scratches due to hard particles trapped between the cloth and the surface damaged small regions, but without affecting the optical properties (right).*

To demonstrate the integrity of the nanostructures after the mechanical test, the surfaces were cleaned with an $O_2$ plasma treatment and measured again. As shown in Figure 3.22 and Figure 3.23, the samples recovered the optical properties with high transmission and high clarity. After coating the samples again, the self-cleaning properties were restored with the same characteristics as before the mechanical test (Table 3.6).
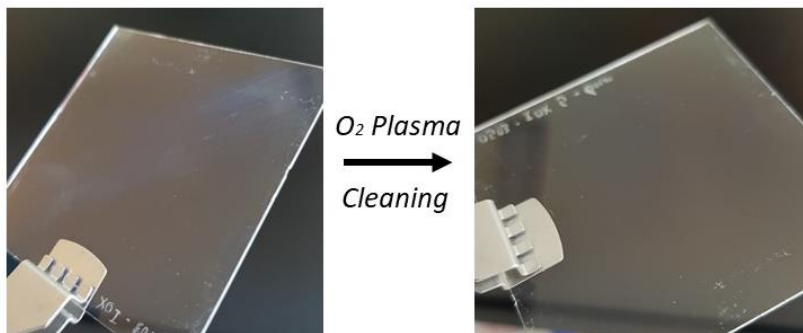


*Figure 3.22 Nanostructured glass samples after the mechanical resistance test (left) and after the oxygen plasma cleaning (right). The sample recovers its optical properties after cleaning.*
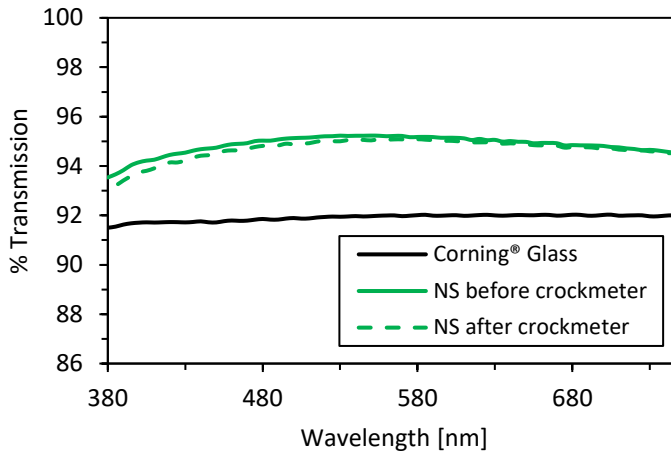
*Figure 3.23 Transmission measurements before (solid line) and after (dashed line) the crockmeter test.*

The test proves that the conical nanopillar structures are robust even for long crockmeter runs, but they trap residues from this particular microfibre cloth, which are clearly visible. Another test was performed with eyeglass cleaning cloth, which is designed to clean glass surfaces. As with the standard microfibre cloth, the structure was not affected by the crockmeter test, but, unlike the standard cloth, there were no residues left between the pillars. This is shown in Figure 3.24.
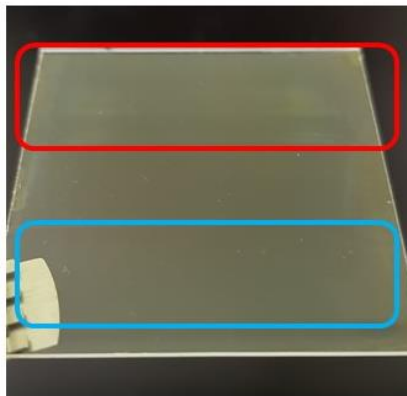


*Figure 3.24 Comparison after the crockmeter test using different cloth materials. Microfibre standard crockmeter test cloth (in red) leaves visible residues between the nanopillars. Microfibre eyeglass cleaning cloth (in blue) does not leave any residue, and the surface maintains the same optical properties without needing to be cleaned using special cleaning methods.*

### 3.5.5 Weathering Test

Accelerated weathering tests are used to simulate severe weather conditions and to evaluate the resistance of materials and coatings designed to withstand these conditions. Typically, specialised instruments like climatic chambers or ultraviolet (UV) exposure lamps are used to speed up the process. However, these tests can lead to severe deterioration, and the main purpose of this section is to evaluate the resistance of the SAM coating used in this work.

*Table 3.7 Detailed ASTM D7869 test cycle sequence*

### ASTM D7869 Test Cycle Sequence

| Step Number | Step Minutes | Function | Irradiance (W/m²/nm) | Black Panel Temperature | Chamber Air Temperature | Relative Humidity |
|---|---|---|---|---|---|---|
| 1 | 240 | dark+spray | - | 40°C | 40°C | 95% |
| 2 | 30 | light | 0.4 | 50°C | 42°C | 50% |
| 3 | 270 | light | 0.8 | 70°C | 50°C | 50% |
| 4 | 30 | light | 0.4 | 50°C | 42°C | 50% |
| 5 | 150 | dark+spray | - | 40°C | 40°C | 95% |
| 6 | 30 | dark+spray | - | 40°C | 40°C | 95% |
| 7 | 20 | light | 0.4 | 50°C | 42°C | 50% |
| 8 | 120 | light | 0.8 | 70°C | 50°C | 50% |
| 9 | 10 | dark | - | 40°C | 40°C | 50% |
| 10 | Repeat steps 6-9 an additional 3 times (for a total of 24 hours = 1 cycle) | | | | | |

The ASTM provides a standardised procedure for the analysis of coatings for outdoor applications under extreme climatic conditions. The test used in this work is the ASTM D7869, developed by companies in the automotive and aerospace industries. The test simulates the hot, humid subtropical climate in Florida, which has been determined as one of the harshest for coatings. These conditions have been used as a testing benchmark due to the combination of high solar radiation, high temperatures and extreme moisture.

The test cycle sequence is divided into ten different steps, as described in Table 3.7. Each 24-hour cycle consists of intercalating dark and high-humidity conditions that simulate the wet night periods, with high UV radiation at high temperatures that correspond to the prolonged sun exposure during the day. In this test, a climatic chamber was used to simulate the dark+spray steps, while the drying process was performed under a UV lamp with a heating system to simulate high temperatures.

The SAM coating (Table 3.8) chosen was the 1H,1H,2H,2H-Perfluorododecyltrichlorosilane, a perfluoro silane (without ether groups). Compared with other coatings, the fluorosilane used to functionalise the studied samples has a high number of fluorine atoms, reducing the surface's polarity and enhancing its superhydrophobicity and stability.

*Table 3.8 Description of the self-assemble monolayer (SAM) coating tested with the ASTM D7859 method.*
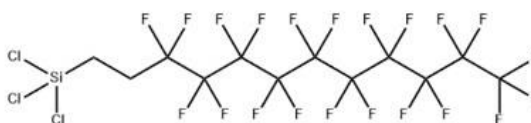


Table 3.9 shows the wetting properties measured with a drop shape analyser before and after the first complete 24-hour cycle. The samples showed excellent resistance against the weathering test, keeping the same self-cleaning properties after completion of all the steps under intense UV radiation and temperature cycles.

*Table 3.9 Wetting characterisation before and after the weathering test. The studied sample  maintained its wetting properties, showing high resistance against the test.*

| | Sample |
|---|---|
| SAM | $C_{12}H_4Cl_3F_{21}Si$ |
| | STATIC CONTACT ANGLE |
| Initial CA | 149 |
| Final CA | 147 |
| | CONTACT ANGLE HYSTERESIS |
| Initial CAH | 12 |
| Final CAH | 13 |

## 3.6 Conclusions

In this chapter, a biomimetic structure inspired by the moth-eye, with an array of nanopillars uniformly distributed on glass substrates, has been proposed. An optimal AR effect has been demonstrated, improving commercially available multilayer coatings with a broadband antireflection and better angular response. The experiments have been supported by simulations that theoretically prove the results obtained. Full mechanical and weathering resistance tests have been performed. The method used to fabricate nanostructured glass is based on scalable techniques and can be easily tuned. To summarise, we have demonstrated a nanostructured, multifunctional optical surface with low reflectivity, low haze, high transmission and high durability, which can be fabricated using large-scale mass production methods for high-performance optical components and optoelectronic devices.

# 4

# Anti-reflective Multilayer Coatings with Self-cleaning Subwavelength Structures

## 4.1 Introduction

Anti-reflective (AR) surfaces are essential elements in many applications, ranging from display screens with reduced disturbance from ambient light, to high-efficiency photovoltaic cells and stable light detection and ranging (LIDAR) systems[3,25,86]. Besides AR, superhydrophobicity (SH) is another attribute that is often desired, as it promotes self-cleaning behaviour[4,58,87]. Therefore, it is technologically advantageous to search for AR and superhydrophobic surfaces that can meet the optical and mechanical requirements for specific applications[88].

Commercially available AR solutions are usually made of single-layer or multilayer (AR-ML) coatings[17,19–21,24–27,89]. These are built on a stack of thin layer materials with different refractive indices, which reduces the overall reflection due to destructive interference of the multiple wavefronts reflected at each interface. By adjusting the number, thickness and optical properties (or choice of materials) of these layers, it is possible to optimise the AR-ML for specific spectral regions. However, due to the resonance nature of the interference, the response tends to be narrowband in wavelength and angle of incidence (AOI).

Chapter three demonstrated that new and more advanced AR surfaces are based on biomimetic nanostructures (NS)[1,2,5,6,59,83,90–96]. The AR effect originates from a smooth refractive index gradient at the interface between the air and the surface. It is possible to achieve higher spectral and angular broadband properties in AR-NS than in AR-ML, while still maintaining negligible scattering loss, due to the sub-wavelength dimensions of the NS[83,90–92,97]. In addition, AR-NS can provide superhydrophobic and self-cleaning properties by coating them with low surface energy molecules, such as self-assembled monolayers (SAM) of fluoropolymers[14–16,83,97–102]. Thus, NS can provide both broadband AR and SH.

Unfortunately, in practice, such structures are not always easy to make with scalable techniques and often suffer from low mechanical durability. These limitations become more critical for the deeper structures required for operation at longer wavelengths. On the one hand, larger nanostructures need to be created in order to maintain the AR properties at such regions of the spectrum, increasing the aspect ratio (height/diameter), and making them more susceptible to mechanical damage, more scattering and difficulties in the fabrication process. On the other hand, although AR-ML can provide a more durable surface due to their flat structure, their AR effect is narrowband, and the wettability cannot achieve superhydrophobicity without surface textures.

This chapter proposes a new AR-ML-NS design, combining AR-ML with shallow NS on the top layer, which provides the following advantages: (i) greater spectral and angular bandwidth and water repellency compared to AR-ML; (ii) easier fabrication, lower scattering and higher mechanical durability compared to AR-NS, due to shallower structures. Theoretical and experimental results are provided for combined AR-ML-NS glass surfaces operating in the visible spectrum (VIS) at 380-780nm, and, in particular, at longer wavelengths in the near-infrared (NIR) at around 900nm, where applications such as LIDAR for autonomous vehicles are of great interest.

## 4.2 Fabrication Process

The proposed design merges two AR technologies. The methods used to create ML coatings are already well established in industrial applications. Physical vapour deposition techniques such as evaporation or sputtering are often used to deposit thin films with high precision. In this experiment, the AR-

ML coatings were fabricated in a cleanroom environment with a sputtering system. However, promising manufacturing techniques to create AR biomimetic surfaces have been developed in recent years and represent a clear step towards the industrialisation of this technology. The NS created on the top layer of the AR-ML followed the method introduced in chapter three.

### 4.2.1   *Fabrication of Anti-reflective Multilayer (AR-ML) Coating*

Double-sided, optically polished, ultraviolet-grade fused silica (FS) glass, with a thickness of 1 mm and an area of 5 cm square, was used as a substrate. The surfaces were cleaned in acetone followed by ethanol in an ultrasonic bath for 10 minutes each. The substrates were then rinsed in deionised water and dried with nitrogen, which was followed by an oxygen ($O_2$) plasma cleaning process (PVA TePla 300 SemiAuto Plasma Asher) for 10 minutes with 300 ml/min $O_2$ and 700 W of power.  For the $SiO_2$ layers, the sputtering deposition (ATC Orion 8m, AJA Internacional, Inc.)  was performed at a base pressure of $10^{-8}$ Torr, room temperature, 175 W of RF-power, 20 standard cubic centimetres per minute (sccm) of pure argon (Ar) and 2 sccm of $O_2$ to maintain the stoichiometry of the target material deposited on the substrate. The working pressure was $1.5 \times 10^{-3}$ Torr, the deposition rate was 0.012 nm/s, and the target-substrate distance was 35 cm. For the $TiO_2$ layers, the deposition was performed at a base pressure of $10^{-8}$ Torr, room temperature, 175 W of RF-power, 20 sccm of pure Ar and 0.4 sccm of $O_2$ to maintain the stoichiometry of the target material deposited on the substrates. The working pressure was $1.5 \times 10^{-3}$ Torr, the deposition rate was 0.018 nm/s, and the target-substrate distance was 35 cm. By varying the deposition time, it is possible to adjust the thickness of each layer according to the desired design.

### 4.2.2   *Anti-reflective Multilayer with Nanostructure (AR-ML-NS) Coating*

The fabrication of nanopillars on the top layer followed the same techniques as discussed in chapter three, and the process is represented in Figure 4.1. The AR-ML samples were cleaned in acetone followed by ethanol in an ultrasonic bath for 10 minutes each. Afterwards, they were rinsed in deionised water and dried with nitrogen, which was followed by an $O_2$ plasma cleaning process for 10 minutes with 300 ml/min of $O_2$ and 700 W of power. Following the same sputtering procedure as for the multilayer coating fabrication, an additional $SiO_2$ layer was deposited to increase the thickness of the last layer. An ultra-thin film of copper (Cu) was deposited by sputtering on top of the AR-ML stack
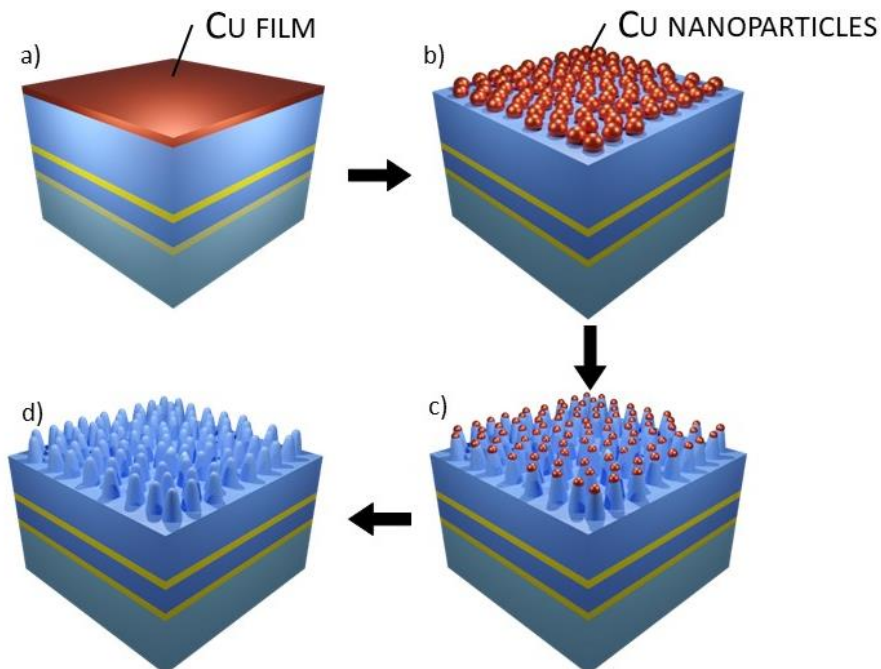
*Figure 4.1 Fabrication process of nanostructures (NS) on top of a multilayer (ML) coating. Ultrathin copper (Cu) film is deposited by sputtering (a) and thermally dewetted into nanoparticles (b). The metal nanoparticles are then used as an etching mask to create nanopillars in the last ML layer, by reactive ion etching (c). Finally, the residual Cu mask is chemically removed (d).*

(Figure 4.1(a)). The deposition was performed at a base pressure of $10^{-8}$ Torr, room temperature, 100 W of DC-power, and 25 sccm of pure Ar. The working pressure was $1.5 \times 10^{-3}$ Torr, the deposition rate was 0.166 nm/s, and the target-substrate distance was 40 cm. The samples were then subjected to a rapid thermal annealing process (RTA) – Figure 4.1(b). Dewetting takes place due to the minimisation of the surface free energy of the system[74], and the metal film reduces its surface area by grouping into small islands. Before the RTA, the samples were blown down with a nitrogen ($N_2$) gun to ensure that the surfaces were completely clear of small dust particles and pollutants that could alter the dewetting process. The RTA was carried out in the TsunamiTM RTP-600S system at a temperature of 600°C for 450 seconds. It is possible to tune the density and size of the nanoparticles by adjusting the Cu initial film and the temperature used in the process, as explained in the optimisation section. The nanoparticles created by dewetting were used as an etching mask (Figure 4.1(c)). The dry etching step was performed by Plasmalab System 100

(Oxford Instruments) with 300W RF power (850 DCV) at $10^{-2}$ Torr in 40 sccm Ar/5 sccm CHF3 plasma. The etching time determines the pillar heights. Afterwards, the residual mask of Cu was chemically removed with ammonium persulfate (Figure 4.1(d)). Finally, the AR-ML-NS samples were cleaned in an ultrasonic bath with acetone and ethanol for 10 minutes each and dried with $N_2$.

## 4.3 Simulations

The AR-ML-NS concept was first studied with simulations. Numerical calculations were used to optimise the sample designs and fabrication process. The AR-ML was modelled as a square cell with the substrate and four layers of intercalated silicon dioxide ($SiO_2$) and titanium dioxide ($TiO_2$) (Figure 4.2). The refractive indices were experimentally obtained by ellipsometry, and the properties of the substrate material (fused silica) were provided by the glass manufacturer. For the AR-ML-NS, the same model was used with a centred nanopillar on top of the fourth layer. Both structures were simulated using periodic boundary conditions, and the geometry of the nanostructure was extracted after a statistical analysis of SEM images.
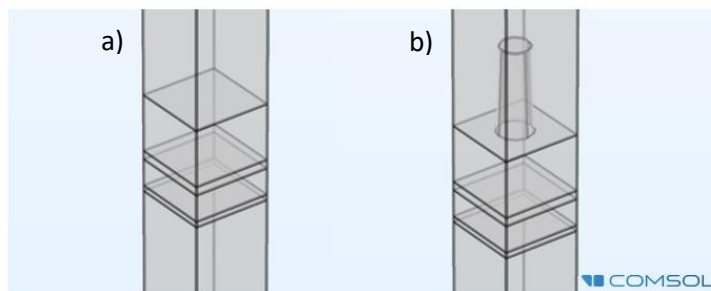


*Figure 4.2 3D-Model geometry defined in the simulation software (COMSOL Multiphysics®). The AR-ML is modelled as a square cell with different layers of different materials (a). The AR-ML-NS has a central pillar on top of the ML design (b). Both models use periodic boundary conditions.*

## 4.4 Optimisation

Four-layer designs, alternating layers of $SiO_2$ and $TiO_2$, were optimised for the VIS and the NIR regions to demonstrate the AR-ML-NS principle and for ease of fabrication. The proposed AR-ML structures were based on previous works to reduce the reflection of glass surfaces. $SiO_2$ and $TiO_2$ have been widely employed as AR coatings for many reasons. Optically, their refractive indices are suitable for the destructive interference of multiple reflections. As surface

layers, both materials present good passivation, anti-scratch properties, and chemical resistance. However, the concept adopted applies to any different number of MLs, different choices of materials or other NS geometries, which could lead to more optimal results.

Depending on the sputtering deposition conditions and the stoichiometry, the refractive index of the deposited materials can vary. Characterisation of the composing materials was performed to determine the essential parameters for the simulation studies and optimisation of the designs. First, the deposition rate was characterised on $Si/SiO_2$ substrates with multiple depositions, and thickness measurements were taken with an atomic force microscopy system and a profilometer. Once the thicknesses of different layers had been characterised, a spectroscopic ellipsometry study (SOPRA, GES5) was performed with a 75W xenon lamp source to obtain the refractive index coefficient of both the $SiO_2$ and $TiO_2$ (Figure 4.3).

a)                       b)
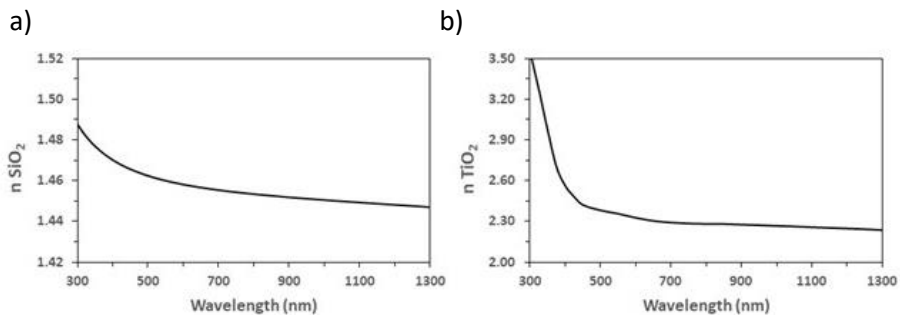


*Figure 4.3 Refractive index of SiO2 (a) and TiO2 (b) used in the simulations.*

After characterisation of the properties of the materials, each AR-ML design was fine-tuned using numerical simulations. Multiple combinations of layer thicknesses were evaluated for optimal AR effects in the VIS and the NIR regions. The parametric modelling system studied more than 600 designs, calculating the average reflection over the whole spectral region for the selection process. The chosen designs present excellent AR performance and are in the top 5%, with the minimum average reflection of all the solutions studied. As well as the optical properties, the ease of fabrication played a significant role in the final selection. Table 4.1 shows the AR-ML designs used for comparison, and the geometrical parameters of the ML and NS for operation either in the VIS or NIR. The NS geometry was optimised to obtain minimum reflection considering the fabrication constraint, i.e. the typical nanopillar density (50 nanopillars per micron square) and base diameter

(60nm). Parametric simulations presented in Figure 4.4 indicate that a height and apex diameter of about 150nm and 50nm, respectively, provide close to optimal operation. These dimensions were confirmed for the fabricated NS by scanning electron microscopy (SEM) images (Figure 4.9).

*Table 4.1. Anti-reflection multilayers (AR-ML) and AR-ML with nanostructures (AR-ML-NS). An ML composed of 5 alternating layers of SiO2 and TiO2 on fused silica substrate with NS made of nanopillars on the top layer was studied as a prototypical AR-ML-NS example. Geometrical parameters are given for structures for visible (VIS) and near-infrared (NIR) operations (380-780 nm and 900 nm, respectively). The AR-ML structure consisting of 4 alternating layers is also prototypical and provides benchmarking for comparing optical performance (Figure 4.8).*



| ML layer | Material | Thickness (VIS) | Thickness (NIR) |
|---|---|---|---|
| Substrate | Fused Silica | - | - |
| 1 | $TiO_2$ | 10.0 nm | 16.3 nm |
| 2 | $SiO_2$ | 47.5 nm | 77.7 nm |
| 3 | $TiO_2$ | 15.0 nm | 24.5 nm |
| 4 | $SiO_2$ | 107.5 nm | 175.9 nm |
| 5 | $SiO_2$ | 100.0 nm | 150.0 nm |

| NS | Material | Height | $D_{BASE}$ | $D_{APEX}$ | Density |
|---|---|---|---|---|---|
| 6 | $SiO_2$ | 150nm | 60nm | 50nm | 50 particles/µm² |
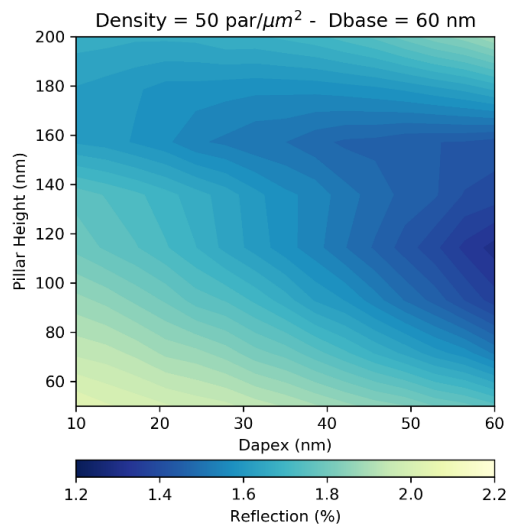


*Figure 4.4 Simulated average reflection in the visible range (380-780) of the antireflective multilayer with nanostructures surface (AR-ML-NS). The studied parameters are the height and the geometry of the nanopillars, being Dapex = 60nm a cilindrical pillar and Dapex = 10nm a cone shaped structure.*

Figure 4.5 shows the correlation between the simulation and experimental results using the parameters given in Table 4.1. The theoretical calculations match well with the samples prepared with the sputtering technique for both regions (VIS and NIR), validating the model used for design and optimisation.
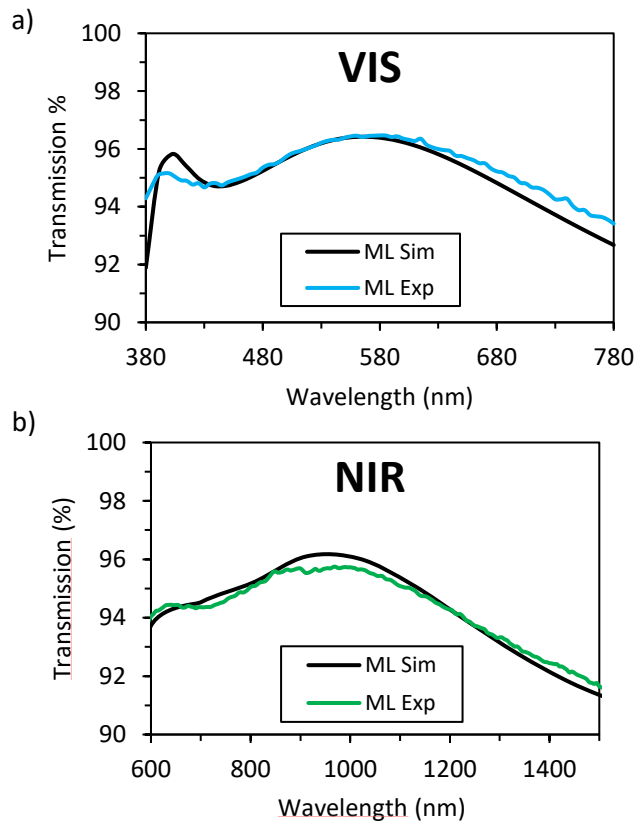


*Figure 4.5 Comparison of total transmission between AR-ML simulated (ML Sim) and AR-ML experimental (ML Exp) in the VIS (a) and NIR (b) regions. Only one surface was coated. Both designs match well with the experimental results.*

Before fabrication of the nanopillars, it was necessary to find the appropriate modifications required to add nanostructures on the top layer of the ML stack. Simulations again helped to optimise this process by analysing multiple top layer thicknesses.

Figure 4.6 shows the optical effect of the top layer thickness after the patterning process. If the last layer of the AR-ML is directly nanostructured, the destructive interference phenomenon is completely changed, and, thus, the AR effect is lost or even reversed, creating a constructive intereference

(Figure 4.6(a)). The proposed solution was to deposit an additional layer of the same top material ($SiO_2$) before nanostructuring in order to preserve or improve the AR effect (Figure 4.6(b)). Depending on the structure created, the last layer has to be modified accordingly in order to obtain optimal optical results. In this particular work, the height of the nanopillars was fixed to 150nm to ensure superhydrophobicity and reasonable mechanical resistance, and the optimal thickness of the last layer was extracted from a parametric simulation. As shown in Table 4.1, before the nanostructuring process, layers of 142.5nm and 124nm were deposited for the VIS and NIR designs, respectively.
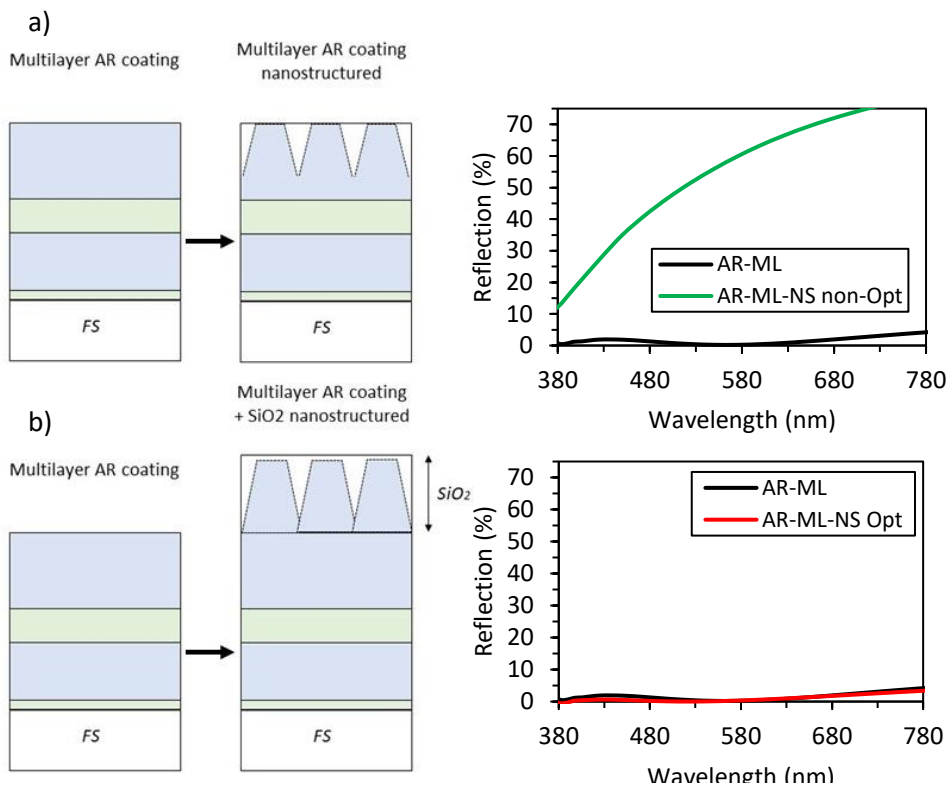


*Figure 4.6 Comparison between AR-ML and the AR-ML-NS with the last layer non-optimised (AR-ML-NS non-Opt) (a) and optimised (AR-ML-NS Opt) (b) to create enhanced AR performance. Directly nanostructuring the top layer causes the AR effect to be lost, due to the the destructive interference of multiple reflections of the AR-ML.*

The fabrication of nanopillars on the ML stack's top layer followed the same procedure as in chapter three. However, the rapid thermal annealing step was again optimised, for two specific reasons. First, the structure has to withstand

a high-temperature process, and it is crucial to determine the maximum temperature where the optical properties of the AR-ML are maintained. Second, the parameters have to be re-adjusted as the ultra-thin Cu film dewetts on a different surface, this being sputtered $SiO_2$. As explained in chapter two, the dewetting phenomenon is sensitive to characteristics of the particular surface and it has to be optimised for the best results.

Figure 4.7 shows the total transmission for AR-ML samples (with the same design) after the completion of RTA processes at different temperatures. The results refer to the initial transmission of the AR-ML design after processing it at two different temperatures. 700°C is the optimised temperature for dewetting Cu on fused silica substrates and was the starting point in this experiment. However, looking at the total measured transmission plot, the process at 700°C generated a significant loss in the optical performance (especially at shorter wavelengths). After several tests, 600°C appeared to be the maximum temperature for this particular ML design, as the samples kept the same transmission after the thermal process.
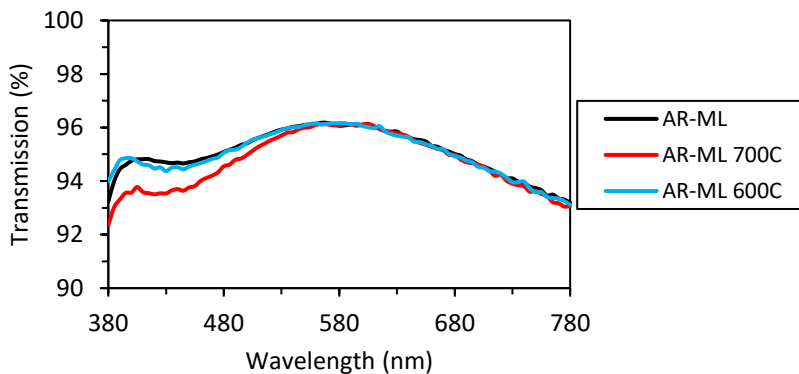


*Figure 4.7 Measured total transmission of different AR-ML samples with only one surface coated and subjected to different rapid thermal annealing temperatures. The system can withstand 600°C for short periods of time with no significant damage or variation in optical properties.*

Following the same optimisation procedure as discussed in chapter three, and keeping the temperature under 600°C, different parameters were tested in order to obtain the best nanoparticles for both ranges (VIS and NIR). The dewetting step is dependent on slight differences in the surface roughness, but, as the scanning electron microscope image shows in Figure 4.8, Cu nanoparticles were successfully created on top of the AR-ML stacks.
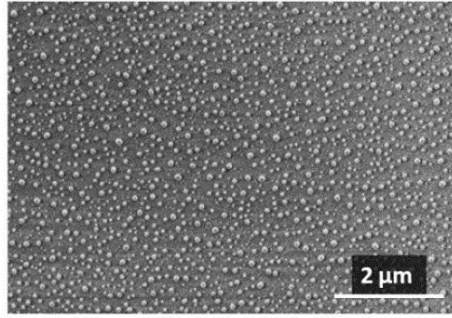
*Figure 4.8 Scanning electron microscope image of dewetted copper nanoparticles at 600°C on the top layer of the ML structure.*

## 4.5 Experimental Results

### 4.5.1 Optical Performance

Two sets of samples were fabricated to experimentally investigate the effect of the NS on an AR-ML in the VIS and NIR regions. The four-layer ML coating geometry is defined in Table 4.1 and was fabricated following the process represented in Figure 4.1. Note that the nanopillar dimensions had to be subwavelength in order to avoid scattering and their height (150 nm) was a compromise between adequate SH and mechanically durability. Also, the thickness of the final layer of the AR-ML-NS was larger than that of the final AR-ML structure to take into consideration the subsequent NS. The fabrication variables used to create the nanopillar array structures are shown in Table 4.2 and the structure dimensions were extracted from an SEM image (Figure 4.9).

*Table 4.2 Fabrication variables and geometrical parameters from scanning electron microscopy analysis of the nanopillars on top of the fourth layer of the ML stacks. The same structure was used for the VIS and NIR designs with a good compromise between superhydrophobicity and mechanical durability.*

| Sample | Cu Film (nm) | RTP (°C) | RIE (min) | $D_{BASE}$ (nm) | $D_{APEX}$ (nm) | Pillar Height (nm) |
|---|---|---|---|---|---|---|
| AR-ML-NS | 6 | 600 | 3 | 60 | 50 | 150 |

The AR-ML and AR-ML-NS samples were optically characterised by measuring their transmission and reflection (Figure 4.10) along with those of the bare fused silica substrate, which served as a reference. Figures 4.10a and b also contain results on AR-NS (same nanostructure design as for AR-ML-NS). The AR-ML structures clearly show an AR effect, i.e. lower reflection and higher
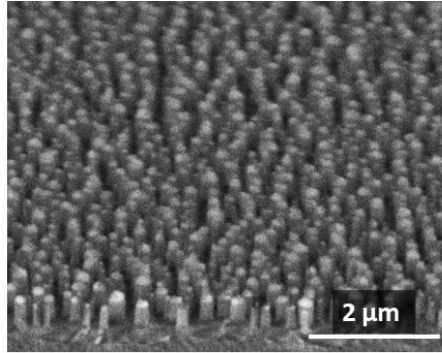
*Figure 4.9 Scanning electron microscope image of the nanopillar structure built on top of the multilayer coating stacks.*

transmission, with respect to the bare substrate. With NS, the combined AR-ML-NS structures for both the VIS and NIR ranges present flatter AR responses, with lower reflectivity and higher transmission compared with those of their AR-ML counterparts. As expected, this is more evident in the VIS range, considering that the NS height is the same for both VIS and NIR, whereas the wavelength nearly doubles in the NIR. The performance of the AR-ML-NS is also significantly superior to AR-NS with the same nanopillar structure, especially in the NIR range. The angular dependence of both AR-ML and AR-ML-NS structures are presented in Figure 4.10(c) and compare well with the simulations in Figure 4.11.

Another important, yet often neglected, parameter for optical surfaces is scattering, which can be quantified by the haze parameter as the percentage of incident light diffused by the sample at an angle larger than ±2.5°. It is known that NS, if not subwavelength, can cause significant scattering. In this case, haze values of 0.03% and 0.13% were measured for the AR-ML and AR-ML-NS surfaces, respectively, indicating very low scattering. To obtain a similar AR effect with only NS, higher nanopillars are needed and, as a result, the haze values would have been much higher. Haze is measured in the VIS range, where the instrument used operates. For the NIR, given that the NS geometry is similar and the wavelength much larger, the haze value and scattering for the combined AR-ML-NS surface should be even lower.
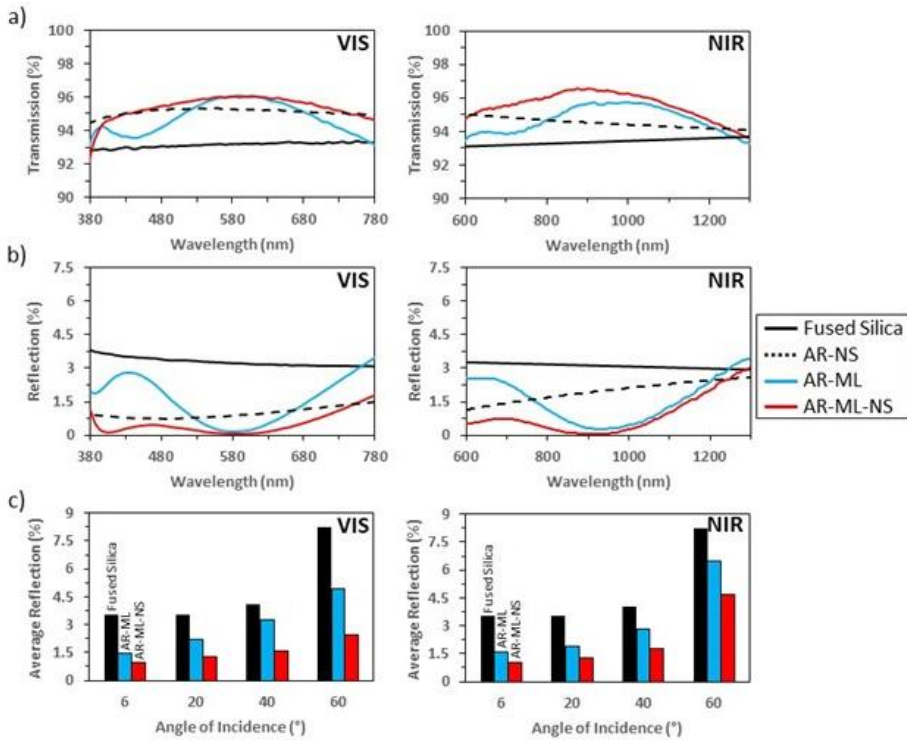
*Figure 4.10 Experimental comparison, total two-side transmission (a) and one-side reflection (b) at close to normal incidence (angle of incidence 6°) between antireflective nanostructured fused silica (AR-NS), antireflective multilayer (AR-ML) and antireflective multilayer with nanostructures (AR-ML-NS) (150nm height nanopillar) optimised for the visible (VIS) region (λ=550nm) (left) and the near-infrared (NIR) region (λ=900nm) (right). Experimental one-side reflection, averaged values over VIS and NIR range, of the proposed AR-ML and AR-ML-NS structures for different angles of incidence. For comparison we also show the calculated bare fused silica substrate (c). In addition to providing superhydrophobicity and self-cleanliness, the NS reduces reflection and thus increases transmission (flat response) over a large wavelength range and for different angles of incidence.*

Figure 4.11 shows the simulated reflection for unpolarised light as a function of wavelength for the VIS Figure 4.11(a) & Figure 4.11(b) and the NIR Figure 4.11(c) & Figure 4.11(d) regions, at different angles of incidence (AOI). The NS on the top layer improves the angular behaviour on the AR-ML surface, i.e. it provides flatter and lower reflectivity over a larger wavelength range and AOI. Note that, as expected, the effect of the NS on the AR-ML is more noticeable in the VIS range. Deeper structures would create comparable benefits in the

NIR range but could lead to mechanical durability issues, as will be explained in the following sections of this chapter.
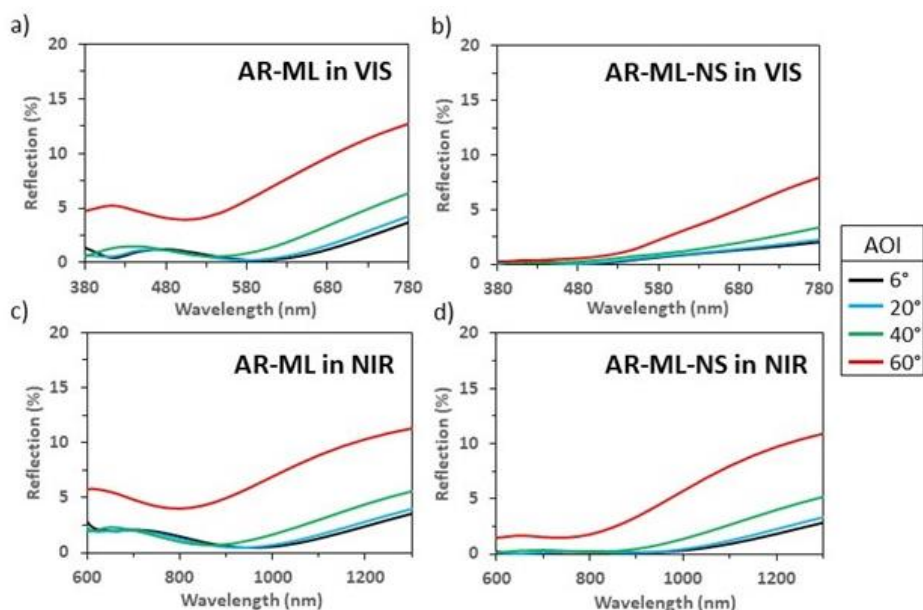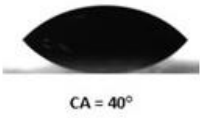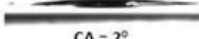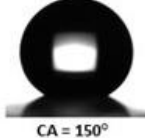


*Figure 4.11 Comparison of anti-reflection (AR) effects between multilayer coatings without nanopillars (AR-ML) and with nanopillars (AR-ML-NS) as a function of angle of incidence (AOI): visible (VIS) (a) and (b) and near-infrared (NIR) (c) and (d). All simulations refer to only one substrate surface, i.e. the back surface is placed at an infinite distance as if it has zero reflectivity. Refractive index and absorption coefficients used in the simulations are shown in Figure 4.2.*

## 4.6 Wetting Performance

The self-cleaning capabilities of a structure are related to the wetting properties between a water droplet and the surface. Static and dynamic contact angles (CA) before and after applying a low surface tension fluorosilane were measured (Table 4.3). The self-assembled monolayer coating used was the same as in chapter three (1H,1H,2H,2H-Perfluorododecyltrichlorosilane) and the method used for the deposition followed the same process. After fabrication, the AR-ML exhibited hydrophilic behaviour (CA<90°) while the AR-ML-NS was superhydrophilic (CA<10°). After functionalising with fluorosilane, the AR-ML became hydrophobic (CA = 115°) while the AR-ML-NS reached a SH state (CA=150°) with a low sliding angle (~ 6°) and low CA hysteresis (CAH<8°), which indicates a strong roll-off effect.

Thus, the results confirm that an initial design with 150 nm nanopillars is deep enough to achieve SH.

*Table 4.3 Wetting characterisation. Comparison of anti-reflection multilayer surfaces that are flat (AR-ML) and nanostructured (AR-ML-NS) before and after the application of a fluorosilane self-assembly monolayer (SAM).*

| Sample | Before Fluorosilane | After Fluorosilane |
|---|---|---|
| AR-ML | CA = 40° | CA = 115° |
| AR-ML-NS | CA = 2° | CA = 150° |

## 4.7 Mechanical Resistance Test

The mechanical durability of the samples was also tested using a crockmeter. Commercially available eyeglass cleaning cloth was used under standard conditions (constant load pressure of $4.5N/cm^2$), and after 1000 repetitions, an SEM analysis (Figure 4.12) revealed that the structure had been preserved (Figure 4.12(b)). This was also consistent with optical transmission measurements before and after the crockmeter test (Figure 4.12(c)) and with calculations showing that the maximum tension is well below the silica's breaking point.

If much deeper NS are created, these could not pass a mechanical test such as this. Figure 4.13 shows a comparison between two different pillar heights (150 and 400nm) under the same wear test conditions. The sample with 150nm nanopillars represents the structure developed in this chapter, with optimal wetting behaviour and improved optical properties. As shown in the SEM image (Figure 4.13(a)), the structure withstands the crockmeter test, showing good mechanical resistance. The sample with 400nm nanopillars (Figure 4.13(b)) represents the structure optimised for the NIR region using only nanopillars. As the stress generated by the crockmeter is proportional to the

moment created by the lateral force, the length of the pillar is a key parameter for its mechanical resistance[96] and, as can be seen in the SEM picture, the taller pillars were more vulnerable to mechanical damage.
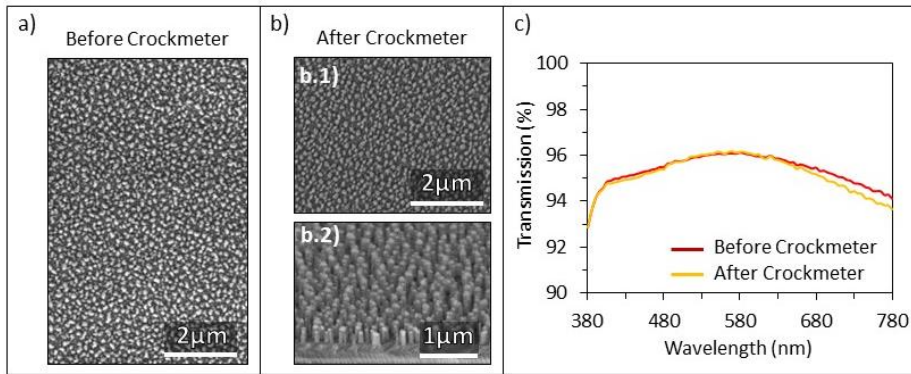


*Figure 4.12 Mechanical durability of the anti-reflective multilayer nanostructured surface (AR-ML-NS), tested with a crockmeter. SEM images before (a) and after (b) more than 1000 repetitions carried out with standard 4.5N/cm² pressure using eyeglass cleaning cloth. Top view (a) and (b.1), and cross section (b.2). The fact that the sample passes the test is also confirmed by optical transmission measurements (c).*
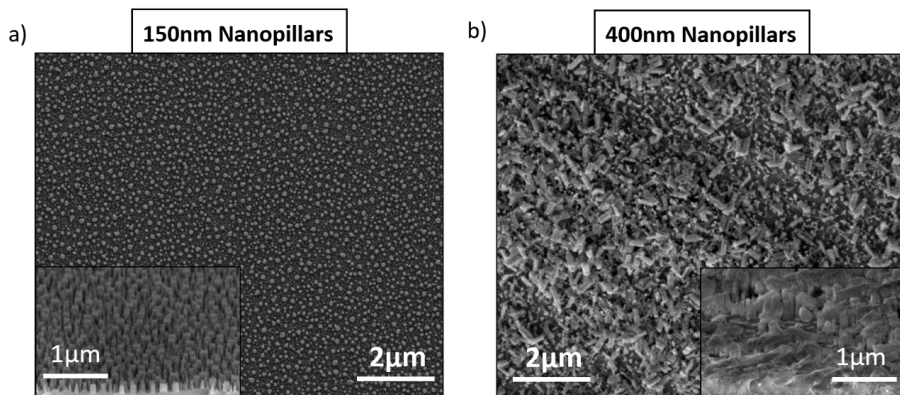


*Figure 4.13 Comparison between two structures, with 150nm and 400nm nanopillars, after the same mechanical resistance test. For structures with 150nm nanopillars, the SEM images show no changes on the surface (a). For 400nm nanopillar structures, most of the nanopillars are damaged after the same crockmeter test.*

The proposed concept of combining NS and ML in order to achieve a combination of AR, SH and mechanical resistance has, therefore, been proven to work.

## 4.8 Conclusions

In this chapter, a multifunctional anti-reflective multilayer with nanostructures (AR-ML-NS), which combines two AR technologies (ML coatings and subwavelength biomimetic NS), has been proposed. It has been demonstrated that the combined structure can provide optimal AR properties, with low reflectivity, broadband wavelength operation and improved angular response. It also has self-cleaning properties, reaching superhydrophobicity. The fabrication process uses scalable methods with lithography-free techniques that can be implemented for different materials and surfaces. The structure can be designed for different wavelength ranges, including the infrared region, while keeping good mechanical resistance and adding superhydrophobicity. All these features make the developed structure very versatile and relevant for implementation in different devices and applications.

# 5

# Nanocavities on Glass

## 5.1 Introduction

Multifunctional optical surfaces have attracted a lot of attention in recent years. Due to their potential impact in numerous industries, many research groups have presented innovative designs and new fabrication methods[26,60,103–105]. Antireflection (AR) and oleophobic properties, combined with moderate mechanical resistance, have emerged as some of the most sought-after requirements for multiple applications, including self-cleaning transparent windows, and windshields for automobiles and aircrafts.

Low energy liquids can drastically change the superhydrophobic behaviour of some of the biomimetic structures mentioned in previous chapters. Oils or other organic substances can seep into the nanostructures, transforming the Cassie-Baxter (CB)[56] state into the Wenzel (W) state[55], drastically changing the wettability of a surface. The development of superhydrophobic and oleophobic surfaces is a good solution for maintaining the self-cleaning

109

capabilities in dirty environments or difficult weather conditions. However, the combination of both of these properties leads to greater fabrication challenges in achieving the specific requirements of transparent optical surfaces, like high optical transmission or low scattering.

So far, two approaches have been used to create oil-repellent surfaces. The first one significantly increases the roughness and lowers the surface energy to ensure the creation of air cavities underneath the liquid[106–108]. The second one uses elaborate micro- and nanoscale re-entrant geometries with primary and secondary structures, or overhang geometries[109,110]. The purpose of such designs is to create an energy barrier to the wetting transition from the CB to W state. It has been claimed that the only possible way of creating a robust oleophobic state is through the fabrication of such structures.

Based on the fundamental understanding inspired by designs in nature, artificial superhydrophobic and superoleophobic surfaces have been fabricated with asperities of different cross-section geometries[108,111–120]. However, such complex structures are difficult and expensive to fabricate and may not be suitable for industrial applications. Therefore, there is great value in developing geometries that are easy to fabricate, yet provide oleophobic and superoleophobic characteristics.

In this chapter, new designs and fabrication processes aimed at creating noninteracting cavities using simple geometries are proposed. The suspension of liquid droplets relies on the mechanism of air compression under the meniscus, leading to stable composite oil-air-solid interfaces. The chosen geometry is nanoholes, and two new methods to create them have been demonstrated on glass substrates. Due to the geometry and subwavelength size of the developed structures, the nanostructured glass samples present anti-reflective properties and improved transmission with high mechanical resistance. The results indicate the possibility of using the modified substrates for a wide range of applications.

### 5.1.1 _Review of Oleophobic Surfaces (Fabrication and Challenges)_

Self-cleaning materials with superhydrophilic or superhydrophobic coatings can keep surfaces clean with the help of an external agent, such as rain or artificial water sprays, while maintaining high performance and reducing the need for maintenance of the devices. Nevertheless, some of the previously

studied nanostructured surfaces cannot repel oils or organic liquids, and, consequently, superamphiphobic (superhydrophobic and superoleophobic) coatings have gained a great deal of attention recently.

Superamphiphobic surfaces need to have a significant roughness (thereby worsening the optical properties) or use tiny re-entrant and overhang structures[109,114,121–128]. The most recent ones showed promising optical and wetting results; however, such elaborate nanoscale structures involve very complex fabrication techniques and present inferior mechanical resistance.

The re-entrant geometry theory[109,121] was first introduced by Tuteja et al., and superamphiphobic surfaces were achieved. They fabricated an oleophobic surface by electrospinning a widely used polymer, Poly(methyl 2-methylpropenoate), also known as PMMA. Later, another structure was created using silica and a two-step etching process. The inverted trapezoidal structure was able to prevent liquid from penetrating the structure as the net forces on the interface of the three phases (air-liquid-solid) was toward the outside of the structure. Gao et al. demonstrated how the capillary force was able to provide an energy barrier that prevented water from entering into the textured surface and maintained the Cassie-Baxter state[122]. They proposed that the structures' geometry was directly related to the resulting net force at the interface.

This chapter explores a new design where oleophobic surfaces can be created using simple geometries that do not require re-entrant structures. This phenomenon can be achieved through the creation of noninteracting cavities on the substrate surface. An example of such a noninteracting cavity is shown in Figure 5.1(a). Square cavities of side 'a', spacing 'b' and depth 'H' were fabricated in silicon substrate via standard photo-lithography and reactive ion etching (RIE). The noninteracting cavities are designed to physically trap air inside, when a liquid meniscus is formed at the top of the cavities. This is a distinctive feature compared to the asperities where the air can leave the space under the advancing oil meniscus through interconnecting pathways.

a)

b)

liquid

trapped air

$P_{air}$, $V_{air}$
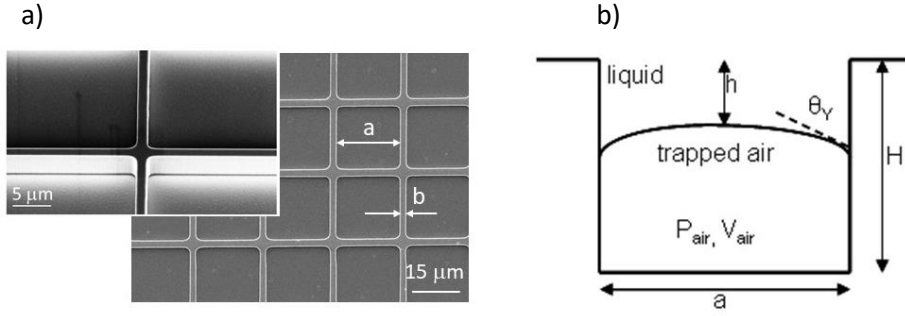
*Figure 5.1 (a) Scanning electron microscope picture of square noninteracting cavity structures fabricated on the surface of a silicon substrate. (b) Schematic of the mechanism of oleophobicity in noninteracting cavities.*

As the meniscus invades the cavity, the air gets compressed, which raises its pressure. The increased pressure of the trapped air opposes the advancing meniscus, and a mechanical equilibrium is reached between the downward capillary force and the upward pressure force exerted by the compressed air, as shown in Figure 5.1(b). This state is differentiated from the CB and W states, as a Partial Wetting (PW) state. A simplified mechanistic model of the PW state can be developed in the following way. If the equilibrium penetration depth is h*, assuming ideal gas law and adiabatic compression, the pressure of entrapped air is given by:

$$P_{air}(h^*) = P_\infty \left[ \frac{a^2 H}{V_{air}(h^*)} \right]^\gamma \tag{1}$$

where $P\infty$ is the atmospheric pressure, $P_{air}(h^*)$ and $V_{air}(h^*)$ are the pressure and the volume, respectively, of the compressed air inside the cavity at the equilibrium condition, and $a$ is the adiabatic index. The volume of air is given by:

$$V_{air}(h^*) = a^2(H - h^*) + \frac{a^3}{6\sqrt{\pi}} \left[ 3 \frac{1 - \sin\theta_Y}{\cos\theta_Y} + \left( \frac{1 - \sin\theta_Y}{\cos\theta_Y} \right)^3 \right] \tag{2}$$

where the second term is the cap volume under the hemispherical[129]. The condition for mechanical equilibrium is:

$$P_{air}(h^*) - P_\infty = \frac{4\sigma \cos\theta_Y}{a} \tag{3}$$

The solution of equilibrium penetration depth can be found from equations 1-3 as:

$$\frac{h^*}{H} = 1 - \left[\frac{aP_\infty}{aP_\infty + 4\sigma \cos\theta_Y}\right]^{1/\gamma} + \frac{\pi a}{6H}\left[3\frac{1-\sin\theta_Y}{\cos\theta_Y} + \left(\frac{1-\sin\theta_Y}{\cos\theta_Y}\right)^3\right] \qquad (4)$$

Using the equilibrium depth h* from equation (4), the overall contact angle (CA) of the partially wetted state could be calculated as:

$$\cos\theta_{PW} = -1 + f(1 + r_f \cos\theta_Y) \qquad\qquad (5)$$

with

$$f = 1 - \frac{1}{(1+b/a)^2} \qquad\qquad (6a)$$

$$r_f = 1 + \frac{4ah^*}{f(a+b)^2} \qquad\qquad (6b)$$

Calculations of the contact angles corresponding to various cavity designs are presented in Table 5.1 for two low surface tension liquids, hexadecane and oleic acid. The Young contact angles are equal to 70° and 80° for hexadecane and oleic acid, respectively, and their surface tension values are 32.5 dynes/cm and 27.5 dynes/cm, respectively. The CB calculation corresponds to the case where the liquid drops remain on the very top of the cavities, offering the highest contact angle. The W calculation corresponds to the case when the liquid fully invades and fills up the cavities, leading to the lowest contact angle. The PW calculation corresponds to the model developed above, where the liquid meniscus partially invades the cavities and is equilibrated by the pressure of the compressed air. The contact angle values of the PW state are very close to the CB contact angles. Liquid contact angles were measured on the fabricated cavities from Figure 5.1(a) after being coated with a fluoropolymer corresponding to the same dimensions as the calculations. The measured contact angle values were then compared with the three theoretical models shown in Table 5.1. The results fall in between the PW and W models, and closer to the PW model than the oleophilic W model. This confirms that the oleophobic state has been achieved on the substrate through the noninteracting cavities.

The PW state micro-holes in silicon described above are not suitable for applications which need optical transparency, e.g. protecting windows, touch screens, car windshields and solar panels. For such applications, an optically transparent substrate material must be used, and the PW state structures

must be smaller than the light wavelength. In the visible range, their dimensions should not exceed about 150 nm in order to avoid scattering effects. A glass substrate (fused silica) was used to demonstrate this effect, and, in this chapter, two methods to create nanohole structures on glass substrates are presented.

*Table 5.1 Compilation of calculated and measured oleic acid and hexadecane contact angle data (in degrees) for microstructure silicon samples after being coated with fluorosilane. The dimensions of a, b and H are in μm. PW=partial wetting, CB=Cassie-Baxter and W=Wenzel.*

| Sample ID | Dimensions | Experiment: Fluorosilane | | Calculated: Fluorosilane, PW | | Calculated: Fluorosilane, CB | | Calculated: Fluorosilane, W | |
|---|---|---|---|---|---|---|---|---|---|
| | | Oleic acid | Hexadecane | Oleic acid | Hexadecane | Oleic acid | Hexadecane | Oleic acid | Hexadecane |
| A | $a = 18.6$, $b = 1.4$ $H = 1.07$ | 127.0 | 115.0 | 145.7 | 142.7 | 147.3 | 146.1 | 78.0 | 71.9 |
| B | $a = 20.5$, $b = 1.5$ $H = 2.4$ | 128.0 | 109.0 | 146.1 | 143.1 | 147.7 | 146.5 | 75.9 | 68.7 |
| C | $a = 20$, $b = 4$ $H = 2$ | 126 | 111 | 129 | 126 | 129.9 | 128 | 77.2 | 70.7 |
| D | $a = 20$, $b = 2$ $H = 2$ | 125 | 106 | 141.4 | 138.5 | 142.8 | 141.4 | 76.6 | 69.9 |
| E | $a = 20$, $b = 2$ $H = 2$ | 126 | 107 | 141.4 | 138.5 | 142.8 | 141.4 | 76.6 | 69.9 |

## 5.2 Simulations

The optical properties of the proposed structures were theoretically studied with a finite element method commercial software (COMSOL Multiphysics®). As in previous chapters, the optimisation of the design was supported with numerical calculations, and the AR effect was analysed with a parametric simulation. The density, size, and depth of the nanocavities were the main variables studied. The structure was simulated using periodic boundary conditions and modelled as a square cell with a central cavity (Figure 5.2). The geometric parameters used to define the structure (Figure 5.3) were the diameter (a) and depth (H) of the holes, and the space between each cavity (b). The refractive index and absorption coefficient of the substrate material used for all the calculations were provided by the glass manufacturer.
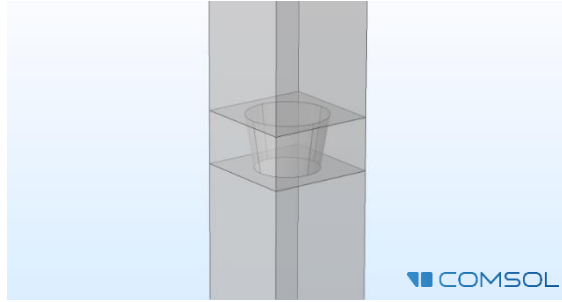
*Figure 5.2 Nanohole structure simulated with COMSOL Multiphysics® software. The geometrical variables used to define the cavities are represented in Figure 5.3.*
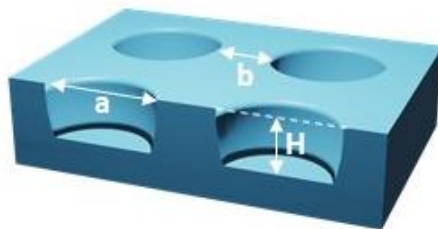


*Figure 5.3 Parameters used to define the geometry of the structure studied: diameter (a) and depth (H) of the cavities and the spacing (b) between each hole.*

## 5.3 Nanocavities Fabricated Using the Langmuir Blodget Method

### 5.3.1 *Fabrication Process*

Micro-holes on silicon wafers were created via standard photo-lithography and reactive ion etching in order to experimentally demonstrate the wetting properties of the cavities theoretically studied. One of the fabrication processes to create nanohole subwavelength structures on a glass surface using scalable techniques is also described in this section.

 *5.3.1.1 Fabrication of Micro-holes on Silicon Wafer.*

The following fabrication process was used to create the silicon micro-holes. Firstly, a silicon wafer surface was cleaned in acetone followed by ethanol in an ultrasonic bath, each process lasting 10 minutes. The substrates were then rinsed in deionised water and dried with nitrogen ($N_2$) gas. Photoresist AZ5214 (from Microchemicals) was spin-coated on a dehydrated silicon substrate and soft baked at 100°C. The hole structures were then patterned by laser

lithography at 405nm wavelength (Microtech Laserwriter LW405B). After development, the cavities were etched by a reactive ion etching system (Plasmalab System 100, Oxford Instruments) using $C_4F_8$ and $SF_6$ chemistry. After etching, the remaining photoresist was removed with acetone.

### 5.3.1.2 Fabrication of Nanohole Subwavelength Structure on Glass Surface.

The process to fabricate a nanohole subwavelength structure on a glass surface is shown in Figure 5.3. Double-sided, optically polished, ultraviolet-fused silica glass substrates, with a thickness of 1mm and an area of 5cm square, were used. The surfaces were cleaned in acetone followed by ethanol in an ultrasonic bath for 10 minutes each. The substrates were then rinsed in deionised water and dried with $N_2$ gas. A uniform monolayer of polystyrene (PS) nanobeads with a diameter of 300nm (from Sigma Aldrich) was deposited on the glass substrate using the Langmuir Blodgett method (KSV NIMA LB from Biolin Scientific) – Figure 5.4(a). The diameter of the nanobeads is a crucial factor when determining the period between each cavity. The deposited nanoparticles were then shrunk with oxygen plasma using a RIE system (Plasmalab System 100, Oxford Instruments) – Figure 5.4(b). The etching process reduces the size of the beads while keeping the same distribution. This step controls the final diameter of the holes and defines the separation between them. A thin layer of copper (Cu) was then deposited with a magnetron sputtering system (ATC Orion 8, AJA International, INC) – Figure 5.4(c). The nanobeads were subsequently removed from the structure using Kapton tape, leaving a Cu mask with an array of nanoholes – Figure 5.4(d).

A Cu mask was used during the RIE process to etch the surface of the glass. Different etching times allowed nanohole structures of different depths to be created. After the RIE, the samples were immersed in ammonium persulfate for 10 minutes to remove the residual metal mask – Figure 5.4(e). The nanostructured glass substrates were then ultrasonically cleaned in acetone, ethanol and deionised water for 10 minutes each, and dried by blowing $N_2$ over the surface.

By adjusting the size of the PS Beads, the shrinking process and the final etching time, specific optimisation of the nanocavity structure (size, distribution and depth) can be performed for different requirements or applications.
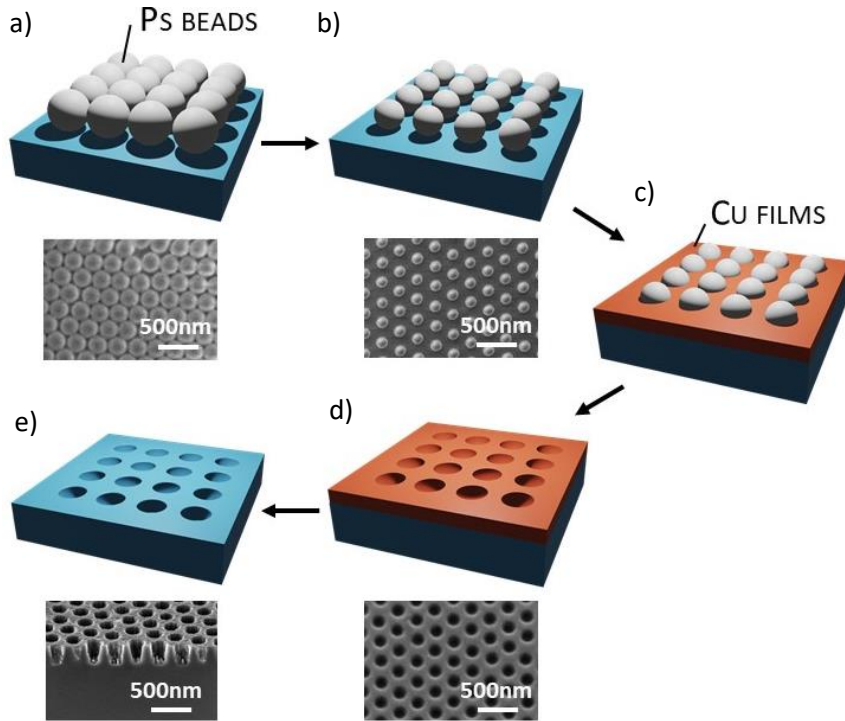
*Figure 5.4 Process used to fabricate subwavelength oleophobic nanohole structures which are also transparent in the visible and near-infrared ranges: deposition of polystyrene nanobeads (a); shrinking using oxygen plasma (b); deposition of the Copper (Cu) film (c); reactive ion etching (d); removal of the Cu mask (e).*

### 5.3.2   *Optimisation*

The development of new fabrication techniques requires a complete optimisation of each step of the process to control the resulting structure. In order to achieve optimal results for specific applications, it is crucial to understand the effect of every variable. The most critical parameters during the fabrication of nanocavities on glass substrates with the Langmuir-Blodgett method are: the size and distribution of the beads, the thickness of the Cu film deposited in between the nanobeads, and the etching process that defines the depth of the holes.

The diameter of the nanospheres not only defines the  dimensions of the holes but also controls the final period of the nanostructured array. The Langmuir-Blodgett technique was used to deposit uniform layers of polystyrene nanobeads ranging from 100nm to 1000nm in diameter. The beads with a

diameter smaller than 200nm were hard to remove with tape after partially being covered with Cu (Figure 5.4(c)). However, this size is still beneficial for optical applications in the visible and near-infrared ranges and has higher resolution than other fabrication techniques. The optimal bead size was found to be 300nm, since this allows a dense structure to be built with the smallest holes that the proposed technique admits. The rest of the parameters were optimised accordingly.

As shown in Figure 5.4(b), the beads are shrunk slightly to reduce the diameter while the period is maintained. This process defines the final size and density of the nanoholes. Optically, the volume fraction of air cavities affecting the sample's AR performance can be varied. Mechanically, if the distance between each hole (b) is larger, the samples can better withstand mechanical stress.

A parametric simulation study was performed to analyse the effect of hole size, fixing the period to 300nm (Figure 5.5). The average reflection in the visible region (400-700nm) was calculated for different combinations of the structure's diameter and depth. Experimentally, the plasma process to shrink the beads was optimised according to the simulation results in order to find the best compromise between the final optical properties, for ease of removing the beads and for mechanical durability against wear or abrasion tests.
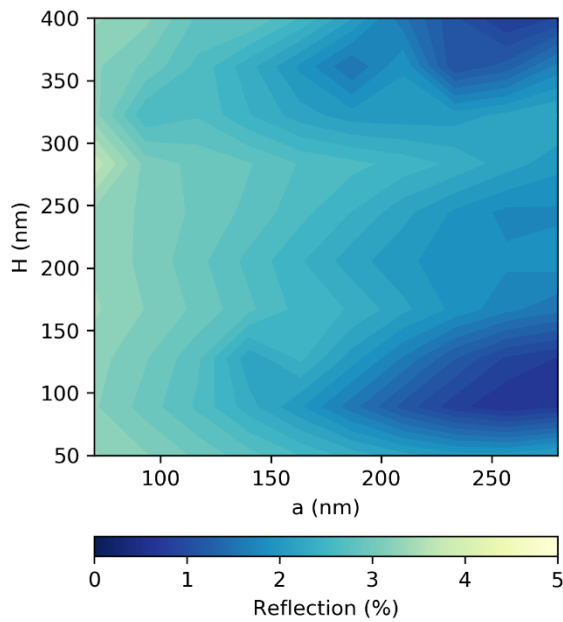
*Figure 5.5 Simulated average reflection in the visible range (400-700nm) for different parametric combinations. Only one surface was considered. Hole diameters from 50nm to 290nm (a) and depths from 0nm to 400nm (H) were evaluated. The period (P) was fixed to 300nm, which is the minimum size of PS beads that can be used with the proposed fabrication method.*

The deposition thickness of the Cu film (Figure 5.4(c)) is an important parameter to study because, firstly, it affects the feasibility of removing the nanobeads with tape, and, secondly, it determines the thickness of the nanohole metal mask for the final dry etching process. The thickness of the film needs to be thinner than the diameter of the nanobeads after the shrinking process, but with enough material to etch the glass during the reactive ion etching process. After different tests, a thickness of 50nm was chosen as it offered a good trade-off between ease of manufacture and ability to create holes ranging from 0 to 400nm in depth, which is the preferred range for optical applications in the visible and near-infrared ranges.

The final dry etching process (Figure 5.4(d)) determines the depth of the nanocavities (H). In order to control the process's selectivity, the etching rates of the Cu and the fused silica substrate were studied for the same RIE recipe. The same metallic mask was used to fabricate a set of samples with different nanohole depths and to study their optical properties. Table 5.2 shows the fabrication variables of the samples studied. The geometric values of the structures were extracted from a scanning electron microscopy (SEM) analysis (Figure 5.6)

*Table 5.2 Fabrication variables for test samples with cavities of different depths. The average geometrical parameters were extracted from a scanning electron microscopy analysis.*

| Sample | PS Beads (nm) | Cu Film (nm) | RIE (min) | a (nm) | b (nm) | H (nm) |
|--------|--------------|--------------|-----------|--------|--------|--------|
| 6' RIE | | | 6 | 235±6 | 40±6 | 230 |
| 7' RIE | | | 7 | 230±5 | 48±5 | 260 |
| 8' RIE | 300 | 50 | 8 | 232±8 | 68±9 | 290 |
| 9' RIE | | | 9 | 232±9 | 46±6 | 320 |
| 10' RIE | | | 10 | 225±7 | 45±4 | 350 |
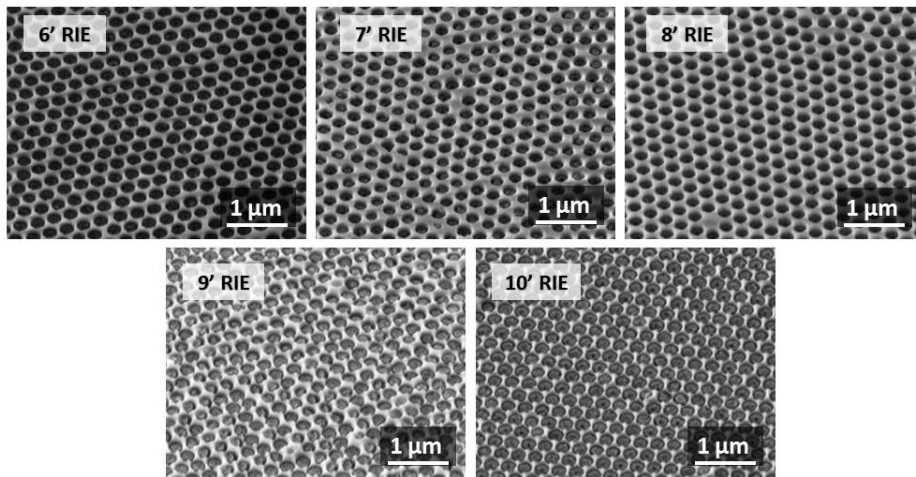


*Figure 5.6 Scanning electron microscope images of the nanostructured test samples. Different reactive ion etching times (in minutes) were studied to see the effect of the different depths on the optical properties.*

The total transmission and reflection of the test samples were measured with a spectrophotometer and are shown in Figure 5.7. A bare fused silica substrate was also measured as a reference. As can be seen, the nanostructured samples present remarkable AR performance with improved transmission. The maximum transmission was shifted to the near-infrared for deeper structures, but more scattering was induced at shorter wavelengths. The scattering of the various samples was characterised with a hazemeter, and the values are plotted in Figure 5.8.
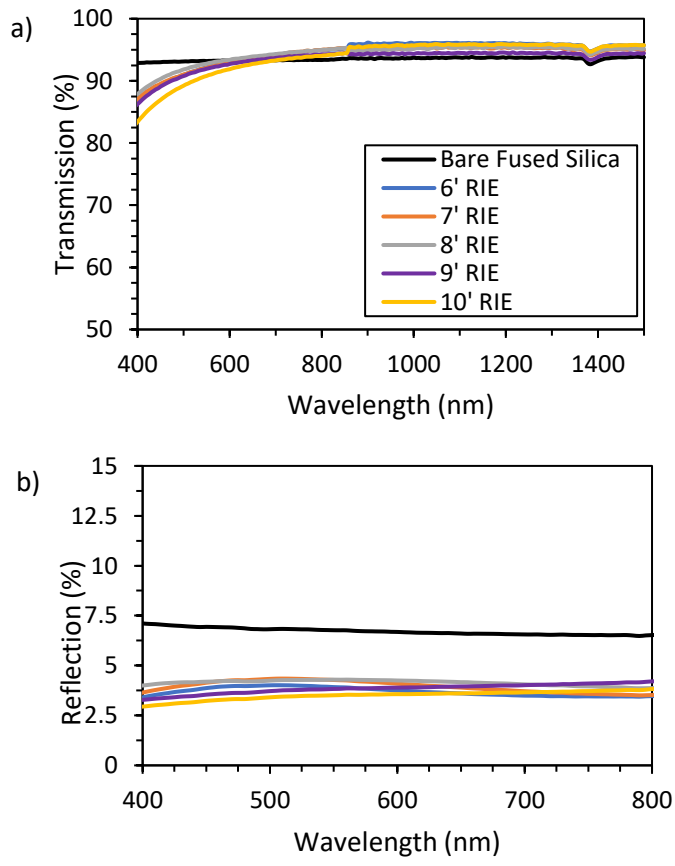


*Figure 5.7 Measured total transmission (a) and reflection (b) of the one-sided nanostructured samples. The different depths of the cavities were defined by the time (in minutes) of the reactive ion etching process.*
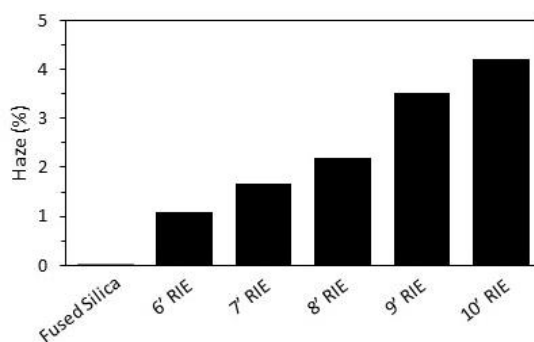
*Figure 5.8 Haze measurements of the samples plotted in Figure 5.7. The scattering induced by the surface roughness of the samples is directly related to the size of the structures. The haze increases proportionaly with the size of the cavities.*

Depending on the requirements of the specific application, the structure can be adjusted by modifying the fabrication parameters. Sample 6'RIE presents lower haze and higher transmission in the visible range while sample 10'RIE, although it has higher haze values at shorter wavelengths, has better transmission in the near-infrared range.

### 5.3.3  *Experimental Results*

#### 5.3.3.1 Optical Performance

The nanostructured samples present improved transmission compared with the bare substrate due to the AR effect of the air cavities. The nanohole array acts as a porous surface with an effective refractive index dependent on the volume fraction between the air and the substrate material, and can be tuned by modifying the geometry of the nanoholes. The optimised fabrication variables used to create nanoholes with the Langmuir-Blodgett techniques are shown in Table 5.3, and the geometrical parameter values were obtained with an SEM analysis of the sample's surface (Figure 5.10).

*Table 5.3 Fabrication variables of the optimised sample with nanocavities. The geometry average values were extracted from scanning electron images (Figure 5.10).*

| Sample | PS Beads (nm) | Cu Film (nm) | RIE (min) | a (nm) | b (nm) | H (nm) |
|--------|--------------|--------------|-----------|--------|--------|--------|
| NS Glass | 300 | 50 | 6 | 235±6 | 40±6 | 230 |

Figure 5.9 shows that the reflection of the nanostructured front surface is almost suppressed, considering that only one surface was modified and the residual reflection (about 3.5%) is entirely due to the flat back surface. The reflection of a bare fused silica substrate with both surface contributions is about 7%. Correspondingly, the optical transmission of the nanostructured sample reaches values above 95%.
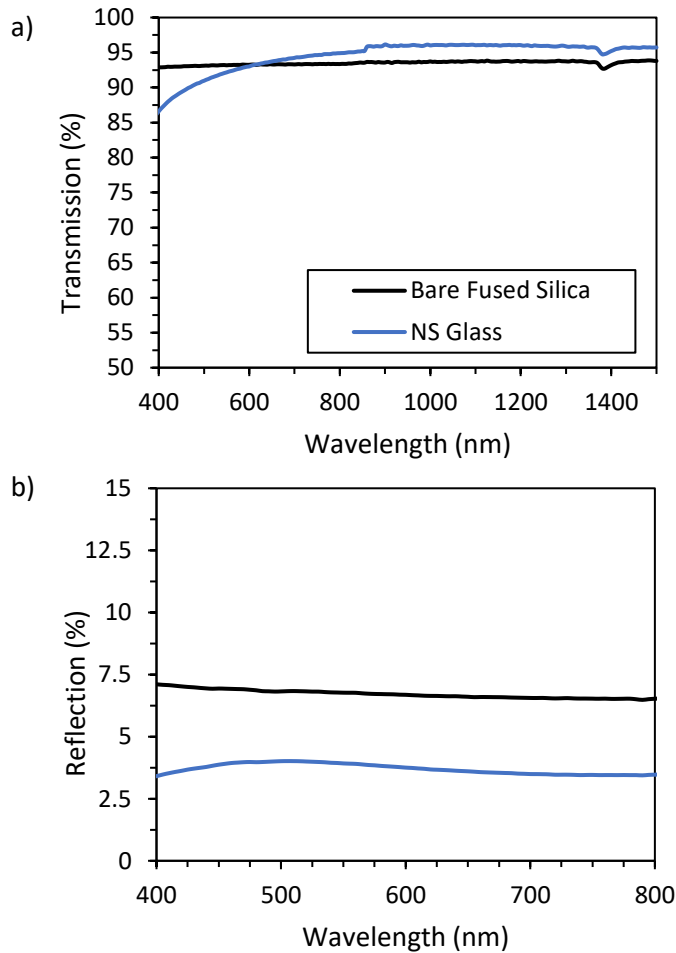


*Figure 5.9 Measured total transmission (a) and reflection (b) of the proposed subwavelength nanohole structure fabricated with the Langmuir-Blodgett method. Only one surface was nanostructured.*
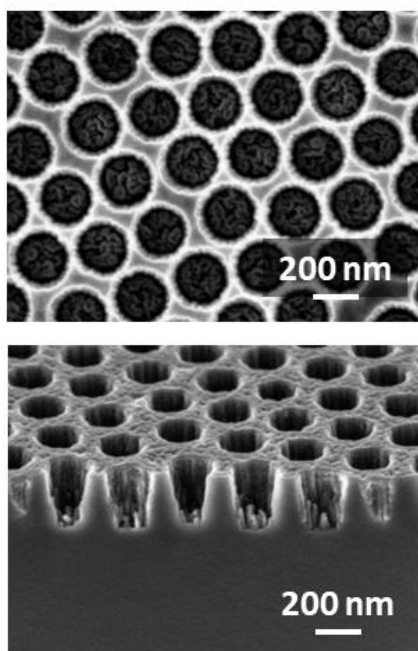
*Figure 5.10 Scanning electron microscope images of the optimised nanostructure sample.*

*5.3.3.2 Wetting*

The nanohole structures are oleophilic right after fabrication and cleaning it using an SC1 process (a mixture of deionised water, NH4OH and H2O2 (5:1:1) at 75-80°C for 10 minutes). The surface becomes oleophobic (contact angle for oil of about 120°) after applying a fluorosilane coating (Table 5.4). Oleic acid and hexadecane were used to evaluate the wetting characteristics of the surface. The method used to functionalise the samples followed the same procedure explained in chapters three and four. 1H,1H,2H,2H-Perfluorododecyltrichlorosilane was the organofluorine used, due to its excellent wetting characteristics and durability against external agents. Note that without structuring the surface, the contact angle of glass coated with fluorosilane would be much lower (about 75°), proving the effect of the air trapping nanohole cavities to improve oleophobicity.

*Table 5.4 Wetting properties of the optimised nanostructure sample (NS Glass). Measurements of the contact angle (CA) for oleic acid and hexadecane taken at each stage, from the fabrication of the structures to the application of the fluorosilane coating to improve the oleophobicity of the structured sample. A flat fused silica sample after application of the fluorosilane was used for comparison.*

| | After fabrication | After SC1 Cleaning | After Fluorosilane | Flat SiO₂ sample After Fluorosilane |
|---|---|---|---|---|
| Oleic acid | CA = 40° | CA = 50° | CA = 117° | CA = 75° |
| Hexadecane | CA = 2° | CA = 2.5° | CA = 106° | CA = 65° |

*5.3.3.3 Mechanical Resistance Test*

Focusing on the potential applications where the proposed structures could be applied, a crockmeter test is a valuable tool for measuring the mechanical resistance of the proposed structure. It can emulate the action of a human finger, which makes it relevant for display screen applications by signalling any wear or damage. The standard crockmeter test provides reproducible and comparable results using a constant load pressure of 4,5N/cm$^2$, applied through a standard rubbing material (microfiber cloth). It evaluates the response of the nanostructured glass surfaces, especially the resistance of the nanoholes after many repetitions. Before and after the test, the samples were characterised by SEM analysis (Figure 5.11(a)) and measurements of the wetting properties (Figure 5.11(b)). In Figure 5.12, the reflection measurements before and after the crockmeter are shown. The results prove that the nanocavities can withstand more than 1,000 repetitions as there is no sign of any significant change in the SEM or wetting response. This mechanical resistance is crucial for most applications where the transparent omniphobic surfaces are touched, either for functional reasons (e.g. touch display screens) or cleaning purposes (e.g. glass windows).

a)



b)

| Before crockmeter test | | After crockmeter test | |
|---|---|---|---|
| Oleic acid | Hexadecane | Oleic Acid | Hexadecane |
| 120 ± 3 | 105 ± 5 | 118 ± 4 | 105 ± 3 |
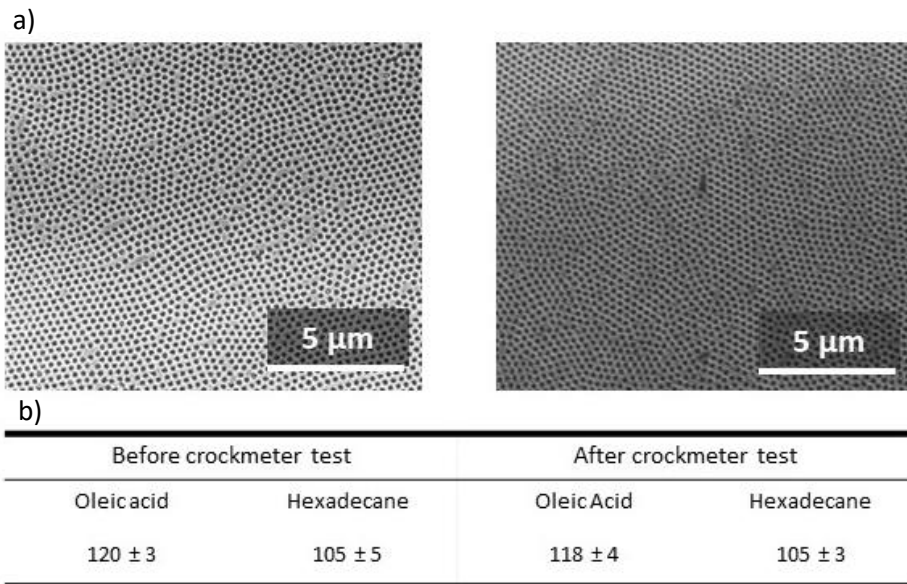
*Figure 5.11 Mechanical resistance test results after 1,000 crockmeter repetitions with a constant load pressure of 4.5N/cm2. Scanning electron microscope images of the nanoholes before and after the crockmeter test (a), and the wetting characterisation (oleic acid and hexadecane contact angles, in degrees) before and after the crockmeter test (b)*
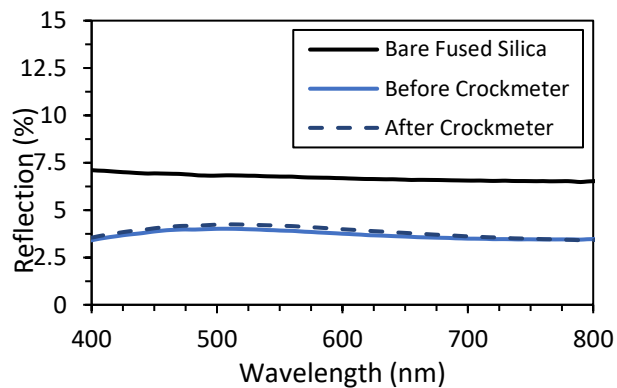


*Figure 5.12 Measured total reflection of one-sided nanostructured glass sample (NS Glass) before and after the crockmeter test.*

## 5.4 Nanohole Structures with Dewetting

The results presented in the previous section were promising for real applications, showing high AR effects, self-cleaning abilities, and, because of the chosen geometry, higher mechanical resistance compared with other structures. It has been demonstrated that the Langmuir-Blodgett technique is a scalable method which can be implemented for large surface areas and mass fabrication. However, like many other manufacturing techniques, the process has some limitations. In this particular case, even though the created structures are on the nanometric scale, the diameter of the holes are larger than 200nm, inducing undesirable scattering.  For high transparency and low haze, nanostructures below 150nm of diameter are required, and in this section, a new method to create smaller nanoholes is described and analysed.

After evaluating the cavities fabricated with the Langmuir-Blodget technology and seeing the potential impact of the structure, the objective was to find an alternative way to create smaller cavities with scalable manufacturing techniques. Reducing the diameter of the holes to below 150nm, although very challenging, would lower the scattering significantly whilst keeping similar oleophobic characteristics and widening the possible future applications.

The proposed method to fabricate smaller nanocavities on glass is based on the dewetting phenomenon. Dewetting was described in chapter two and the process was used to fabricate nanopillars on glass substrates, as discussed in chapters three and four. By rapidly annealing an ultra-thin metal film in high temperatures, it is possible to create randomly distributed metal nanoislands. These nanoparticles can be used as a mask during the etching process, transferring their pattern to the surface. The size and density of the nanoparticles depend on the initial metal thickness, as well as the temperature and time of the annealing process. By controlling these variables, it is possible to obtain a wide range of different nanoparticle distributions and sizes.

The deposition of the PS nanobeads using the Langmuir-Blodgett technique, and the removal of the beads with tape, were the limiting factors in the previous procedure. The proposed method uses dewetted Cu nanoparticles and a chemical etching process to create a metallic mask with a nanohole array. After dewetting the initial Cu film, the space between the spherical

nanoislands is filled with another metal. Nickel (Ni) was chosen in this experiment as it withstands the Cu etchant (ammonium persulfate) process. The Cu nanoparticles can be selectively removed using a chemical etching process, leading to a metallic thin film with an array of nanoholes that can be used as a mask to transfer the pattern to the substrate.

## 5.4.1  Fabrication Process

### 5.4.1.1 Fabrication of Nanohole Subwavelength Structure on Glass Surface – Dewetted Nanoparticles.

The fabrication process used to create the nanohole subwavelength structure on the glass surface is shown in Figure 5.13. Double-sided, optically polished, ultraviolet-fused silica glass substrates, with a thickness of 1mm and an area of 5cm square, were used. The surfaces were cleaned in acetone followed by ethanol in an ultrasonic bath for 10 minutes each. The substrates were then rinsed in deionised water and dried with $N_2$ gas. An ultra-thin metal film of Cu was first deposited using a magnetron sputtering system (ATC Orion 8, AJA International, Inc.), as shown in Figure 5.13(a). Using a rapid thermal annealing (RTA) system (RTP-150-HV, Unitemp GmbH), the samples were then rapidly annealed in high temperatures to form nanoparticles, as shown in Figure 5.13(b). High purity $N_2$ gas at a pressure of one atmosphere was used to prevent oxidation of the metal film.  By controlling the thickness of the deposited metal, the temperature, and the duration of the annealing process, it is possible to define the geometry of the nanoparticles formed by dewetting as presented in Chapter 3. A thin film of Ni was then deposited by sputtering on top of the Cu nanoparticles, filling the gaps between them but without covering the whole structure – Figure 5.13(c). The Cu was chemically removed using ammonium persulfate, leading to a nanohole patterned Ni mask with enough thickness to be used for a dry etching process – Figure 5.13(d). An RIE system (Plasmalab System 100, Oxford Instruments) was used to etch the surface of the glass, creating a nanohole structure with the same pattern as the dewetted particles of Cu – Figure 5.13(e). Finally, the samples were immersed in Ni etchant (iron chloride) to remove the residual metal mask. The nanostructured glass substrates were ultrasonically cleaned in acetone, ethanol and deionised water for 10minutes each and then dried by blowing $N_2$ over the surface.
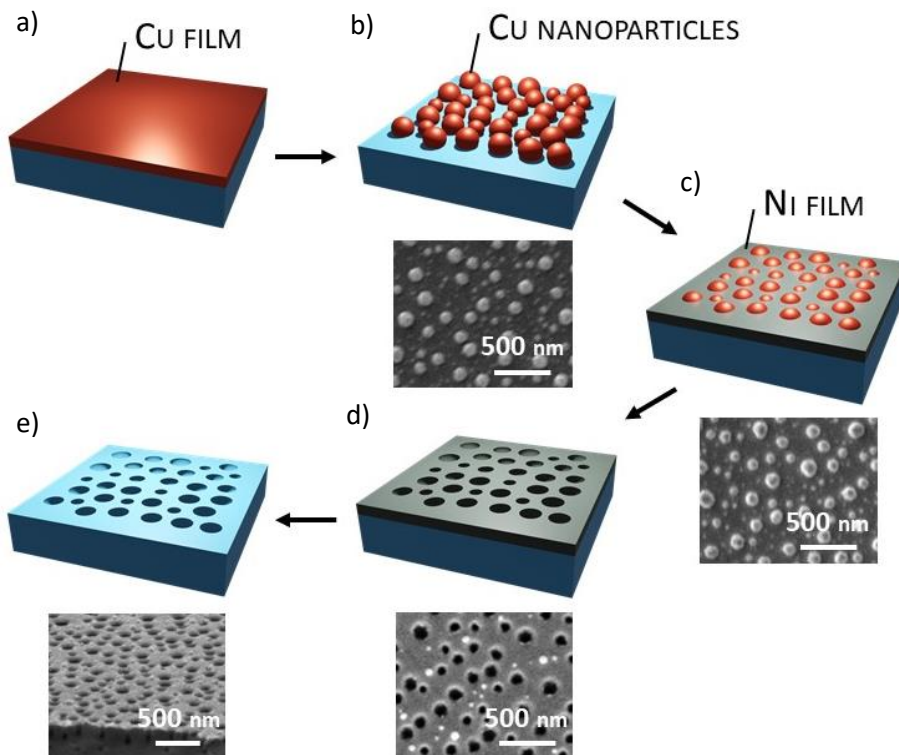
*Figure 5.13 Process flow for the fabrication of subwavelength nanohole structures, which are also transparent in the visible and near-infrared ranges: deposition of an ultra-thin film of Cu (a); thermal dewetting (b); deposition of a Nickel film (c); selective chemical etching of the Cu nanoparticles (d); reactive ion etching and removal of the residual Ni mask (e).*

## 5.4.2   *Optimisation*

Each step of the fabrication process described above was optimised to obtain the best optical and wetting characteristics. Among all the variables involved, the most important steps were the dewetting process, the Ni deposition, and the final dry etching.

The final size and distribution of the nanoholes are defined in the dewetting stage. The nanoparticle array created during the thermal process matches well with the final structure, as shown in Figure 5.14.
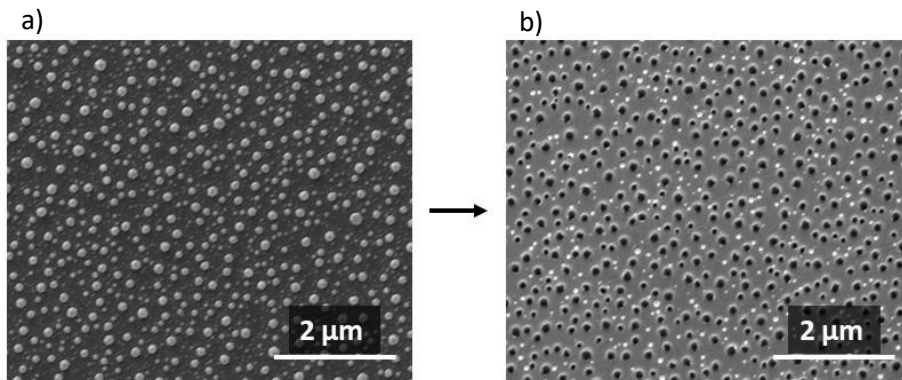
*Figure 5.14 Scanning electron microscope images. Distribution of the dewetted Cu nanoparticles (a) is comparable with the nanohole array created on the nickel thin film after the copper chemical etching process (b).*

Simulations were used to analyse the geometric parameters of the nanoholes needed for optimal AR performance, with different hole diameter and depth combinations being evaluated (Figure 5.15). Taking into consideration the average distribution of dewetted Cu particles discovered in previous chapters, the period was fixed to 150nm.
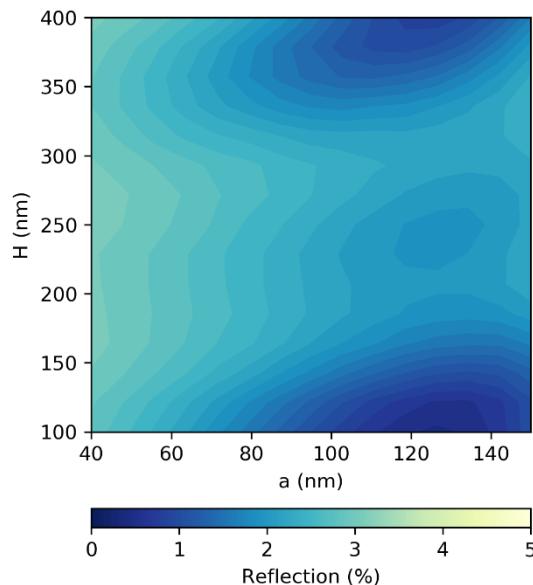


*Figure 5.15 Simulated average reflection in the visible range (400-700nm) for different parametric combinations. Hole diameters from 40nm to 145nm (a) and depths from 100nm to 400nm (H) were evaluated fixing the period to 150nm.*

As with the Langmuir-Blodgett method, the optical properties, wetting capabilities and mechanical resistance were evaluated in order to select the optimal geometry of the nanostructures. The dewetting step (Figure 5.13(b)) was optimised according to the results of the simulations to obtain a dense structure with hole sizes from 90nm to 130nm, and multiple RTA processes were run to analyse the distribution of the Cu nanoparticles.

The thickness of the Ni mask was also studied. After optimising the dewetting step and the dimensions of the Cu nanoparticles, various films were sputtered on top of the metallic structures and then etched with ammonium persulfate following the same procedure for comparison. If the Ni fully covers the particles, the Cu nanoislands remain unaltered during the etching process. For thicknesses near the average height of the nanoparticles (75nm), only part of the nanoparticles are etched, as shown in Figure 5.16. The chosen Ni thickness for this structure was 50nm. Most of the particles can easily be removed chemically, and the resulting Ni nanohole mask has enough material to create deep structures (more than 300nm) during the final etching process. Note that for different particles sizes, the Ni film has to be readjusted for optimal results.
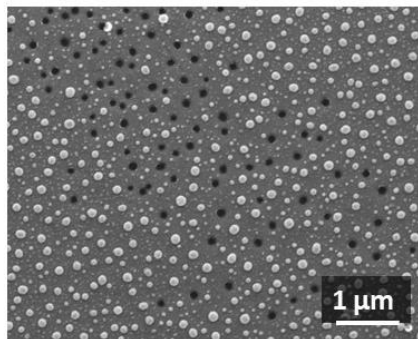


*Figure 5.16 Scanning electron microscope image of partial etching of the Cu nanoparticles.*

The final dry etching process was characterised to study the effect of the depth of the holes on the optical properties. The fabrication variables of the test samples and the geometric parameters measured with SEM analysis are shown in Table 5.5, and Figure 5.17 displays the transmission and the haze values of the studied samples. Sample 1'RIE, with an average hole diameter smaller than 100nm, presents improved transmission and low haze over the whole visible region with respect to the bare glass. Samples with deeper

131

cavities shift their optimal transmission to the near-infrared region with a significant increase in the haze values at shorter wavelengths.

*Table 5.5 Fabrication variables of nanostructured test samples and the geometric parameters extracted from scanning electron microscopy analysis.*

| Sample | Cu Film (nm) | RTP (°C) | Ni Film (nm) | RIE (min) | a (nm) | b (nm) | H (nm) |
|--------|--------------|----------|--------------|-----------|--------|--------|--------|
| 1' RIE | | | | 1 | 90 ± 10 | 112 ± 24 | 160 |
| 1,5' RIE | 8 | 600 | 50 | 1,5 | 112 ± 11 | 94 ± 31 | 245 |
| 2' RIE | | | | 2 | 120 ± 17 | 67 ± 29 | 330 |
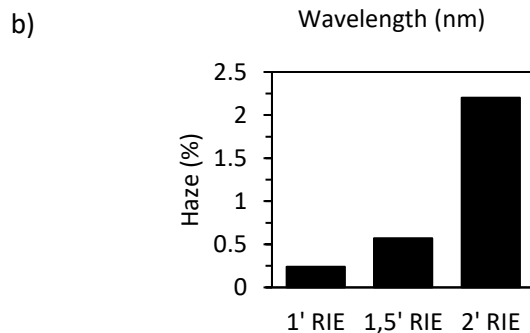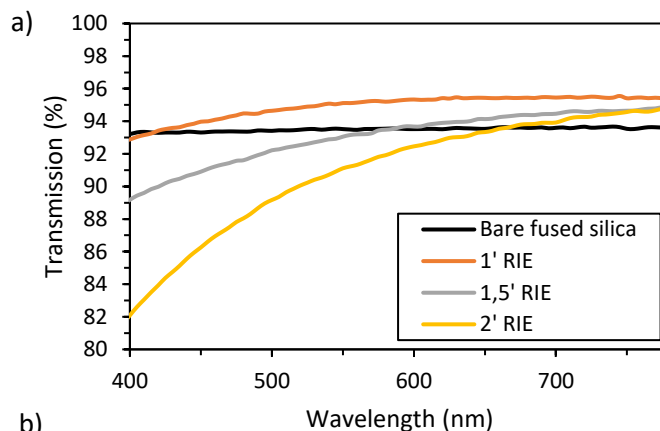


*Figure 5.17 Measured total transmission (a) and haze (b) for holes of different size and depth. Only one side was nanostructured. For deeper structures, the haze increases, reducing the transmission at shorter wavelengths.*

## 5.4.3    *Experimental Results*

### 5.4.3.1 Optical Performance

As shown in Figure 5.18, the new structure with smaller nanoholes on fused silica presents higher transmission with a flatter curve compared to the nanocavities produced with the Langmuir-Blodgett technique. This proves that the scattering at low wavelengths has been reduced, significantly improving the overall transmittance of the sample. The subwavelength size and the geometry of the nanoholes (Table 5.6) create an effective refractive index, given by the volume ratio between air:substrate (FS). Proper optimisation of this ratio determines if the structure is close to the quarter-wave plate condition for antireflection. Even though this condition is not fully accomplished, the results presented show a remarkable improvement in the optical characteristics without the need for a lithographic process.

| Sample | Cu Film (nm) | RTP (°C) | Ni Film (nm) | RIE (min) | a (nm) | b (nm) | H (nm) |
|--------|------|------|------|------|------|------|------|
| NS Glass | 8 | 600 | 50 | 1 | $90 \pm 10$ | $112 \pm 24$ | 160 |

*Table 5.6 Fabrication variables of the optimised nanostructured sample (NS Glass) with the geometric parameters extracted from scanning electron microscope images (Figure 5.20).*
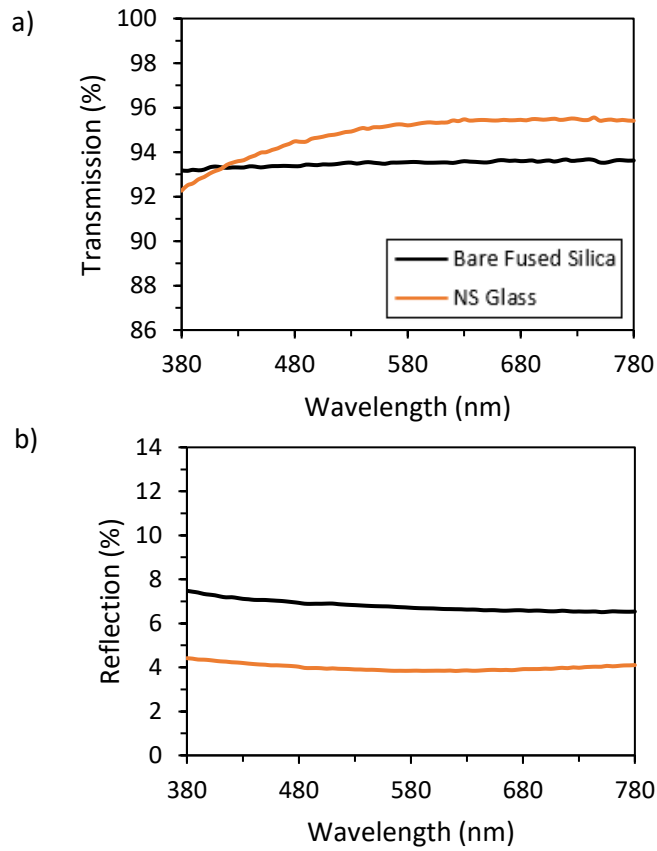
*Figure 5.18 Measured total transmission (a) and reflection (b) of the optimised one-sided nano\structured glass with smaller cavities.*
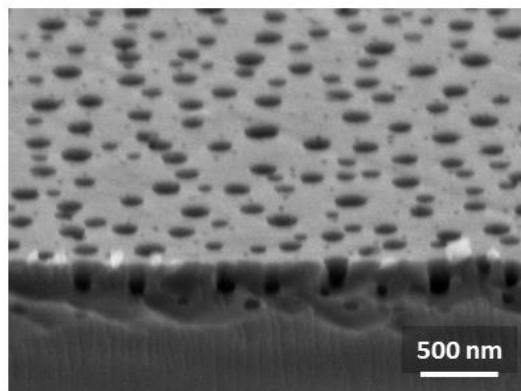


*Figure 5.19 Scanning electron microscope image of the NS Glass sample.*

The nanohole structure created from dewetted nanoparticles presents similar oleophobic behaviour as the structure from the Langmuir-Blodgett process. The samples were oleophilic right after the fabrication process, and after functionalisation of the surface using the same fluoropolymer, comparable results were obtained, as shown in Table 5.7.

*Table 5.7 Wetting properties of the subwavelength nanohole structure from dewetted nanoparticles*

|  | After fabrication | After SC1 Cleaning | After Fluorosilane | Flat $SiO_2$ sample After Fluorosilane |
|---|---|---|---|---|
| Oleic acid | CA = 40° | CA = 41° | CA = 116° | CA = 75° |
| Hexadecane | CA = 3° | CA = 3° | CA = 103° | CA = 65° |

*5.4.3.3 Mechanical resistance*

The same mechanical resistance test (1,000 crockmeter repetitions with a constant load pressure of 4,5N/cm$^2$ and microfiber standard crockmeter cloth) was performed to analyse the mechanical resistance of the smaller nanoholes.

a)



b)

| Before crockmeter test | | After crockmeter test | |
|---|---|---|---|
| Oleic acid | Hexadecane | Oleic Acid | Hexadecane |
| 116 ± 2 | 103 ± 3 | 117 ± 3 | 102 ± 5 |
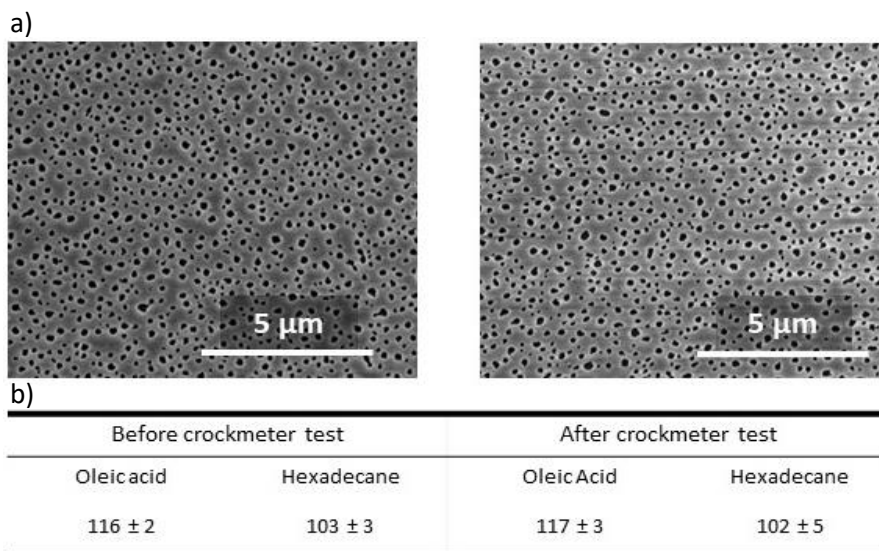
*Figure 5.20 Mechanical resistance test results after 1,000 crockmeter repetitions with a constant pressure of 4,5N/cm2. Scanning electron microscope images of the nanoholes before and after the crockmeter test (a) and wetting properties (oleic acid and hexadecane contact angles, in degrees) before and after the crockmeter test (b).*

As shown in Figure 5.20(a), SEM images indicate that the structure can withstand the crockmeter test, maintaining the same geometry with no sign of wear or damage. The wetting properties, shown in Figure 5.20(b), also remained constant, as did the total reflection measurements before and after the test (Figure 5.21). Moreover, the samples kept the same optical performance, proving their high mechanical resistance.
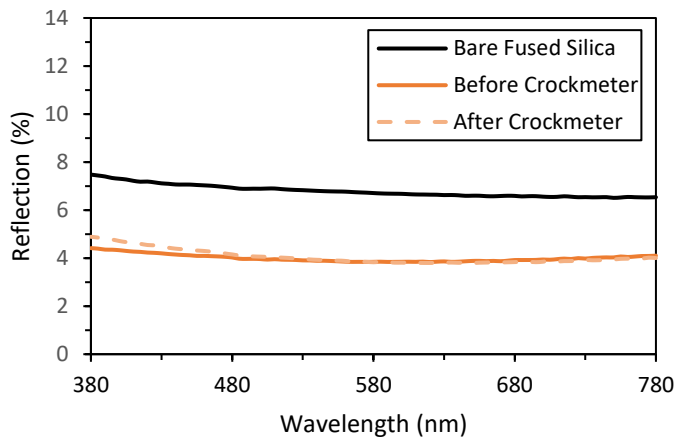


*Figure 5.21 Total reflection of the optimised nanostructured glass sample (NS Glass)  before (solid line) and after (dashed line) the crockmeter test.*

## 5.5  Conclusions

A new anti-reflective, transparent and oleophobic surface based on noninteracting cavities, without the need for re-entrant or overhang structures, has been proposed and demonstrated. The approach applies to transparent substrates, such as glass, provided that subwavelength nanometric-scale holes (cavities) are created. The porous surface of the nanoholes induces the AR effect, acting as a coating with an effective refractive index adequate to create a destructive interference with the reflected light rays. When the nanostructure has a subwavelength dimension, light scattering becomes negligible, thus preserving the directionality of the transmitted beams.  The phobic behaviour is attributed to the pressure generated by the air trapped in the holes (cavities) underneath the liquid and named as the partial wetting state. As shown in this chapter, the partial wetting nanoholes can be made using scalable techniques for large areas, and could have an impact on anti-smudge touch screens, automobile windshields, solar panels and other applications that require high transmission and self-cleaning properties. Two scalable methods have been presented in this

chapter. The Langmuir-Blodgett technique created a more periodic-like array of nanoholes but with a size limitation, while the dewetted particles allowed for the creation of smaller holes, which improved the optical properties yet maintained the wetting characteristics of the previous method. Both structures showed excellent mechanical resistance, making them attractive options in many different applications.

# 6

# Nanostructured Polyimide

## 6.1 Introduction

Highly transparent optical surfaces with anti-reflective (AR) properties have been extensively studied over recent years. The enhanced characteristics of such solutions have the potential to increase the performance of a wide range of optoelectronic devices, such as photovoltaic cells, photodetectors and display screens, among others. The demand for flexible devices has increased and is pushing the transparent optical surfaces industry towards polymeric flexible substrates. As mentioned in previous chapters, biomimetic structures inspired by nature can offer superior AR properties with added functionalities like self-cleaning behaviour[1,4,83,86,90–95,100,130]. However, most of the proposed techniques to modify the surface of polymers do not have enough resolution to reach the nanoscale or are not scalable to an industrial level[69–71,131–135]. For instance, electron-beam and nano-imprint lithography are very time-consuming and complex processing methods that cannot be applied to large surfaces.

This chapter proposes a new method to nanostructure thin polymeric films, using scalable techniques with high resolution (structures of less than 100nm diameter). The created nanometric hole structures are densely packed,

showing that the method can be employed as a tool to achieve resolutions (minimum features) that are comparable to or surpasses the results accomplished with more expensive and elaborate processes.

Nanostructured polyimide (PI) on glass substrates is introduced as a hybrid material easier to fabricate than other methods, as it obviates the need for a glass etching step, while still preserving similar AR and durability properties compared with nanostructured substrates discussed previously. PI was chosen due to its high transparency in the visible wavelength region and, also, its high chemical and mechanical resistance[136–138]. Metal dewetting was used to nanostructure the PI films. Metal dewetting has already been used for nanostructuring the surface of glass substrates[83,90,91,130], but this is the first time that it has been exploited to nano-pattern films of polymers such as PI. This technique has the advantage of being simple and scalable as it does not rely on time-consuming and sophisticated lithography steps. Nano-imprint technology is often used to create polymer nanostructures on a receiving substrate via moulding of an initially deposited film using a proper mask. Conversely, with this approach the Cu nano-mask is first defined on the substrate and then, secondly, the polymeric PI film is deposited. Finally, the nanostructure is created by simple etching of the Cu nano-mask.

The versatility of the current metal dewetting based nano-patterning method has been demonstrated by creating nanohole PI films on glass and indium tin oxide (ITO) coated glass substrates, leading to a combined effect of high transparency, low reflectivity and high conductivity, making it a suitable candidate for applications such as transparent heaters. Additionally, a numerical model of the hybrid substrate's optical properties has been developed, enabling an optimal design. The proposed structure and method, based on conventional spin-coating and lithography-free metal dewetting, can potentially create a low-cost pathway to nanostructure AR transparent substrates.

## 6.2 Fabrication Process

### 6.2.1 *Nanohole Patterning of Polyimide (PI) Film on Glass Substrates.*

In recent years, patterning techniques such as nano-imprint lithography (NIL) or micro-contact printing (μ-CP) have been explored for nanostructuring a wide range of polymers. Attempts to nanostructure a thin layer of PI on

different substrates have also been reported. Some of the crucial aspects to be considered when developing new fabrication methods are the resolution, cost, speed and repeatability of the technique. Nanostructuring via NIL shows fair resolution and throughput, but, despite this, NIL suffers from several drawbacks. If the PI curing is performed during the moulding step, lower processing temperatures can be used, but solvent degassing could occur, creating bubbles and damaging the structures. In addition, the demolding step can also distort the shape. If, instead, the NIL template is employed on a PI film that has already been cured, temperatures above glass transition are needed. These typically range from 300 to 500°C, which could be too high for many materials used in devices. Etching the PI layer using a previously NIL-nanostructured photoresist as a mask can also be considered. Nevertheless, this method is not preferable, as it usually requires additional etching steps or intermediate silica layers between the PI film and the photoresist.

Most of the current patterning alternatives for polymers involve a lithography step at some stage in the process, either to pattern photosensitive polyimides and photoresists or to fabricate the required mould for the imprint process. In this work, a cost-effective metal dewetting technique to form the initial nano-patterning mask is proposed, eliminating the need for additional steps.

The fabrication steps for nanostructuring PI on glass substrates are shown in Figure 6.1. Double-sided, optically polished, ultraviolet-grade fused silica glass substrates, with a thickness of 1mm and an area of 5cm square, were used. Initially, their surfaces were cleaned in acetone followed by ethanol in an ultrasonic bath for 10 minutes each. The substrates were then rinsed in deionised water and dried with nitrogen, which was followed by an oxygen plasma cleaning process for a further 10 minutes (PVA TePla 300 SemiAuto Plasma Asher). Ultrathin copper (Cu) film with a thickness of 15nm was then deposited on the flat glass surface using a magnetron sputtering system (ATC Orion 8, AJA International, Inc.) – Figure 6.1(a). The depositions were performed at a base pressure of $10^{-8}$ Torr, room temperature, 100W of DC-power and 25 standard cubic centimetres per minute (sccm) of pure Argon (Ar). The working pressure was $1.5 \times 10^{-3}$ Torr, the deposition rate was 0.166nm/s, and the target-substrate distance was 40cm. The samples were subjected to rapid thermal annealing (RTA) – Figure 6.1(b), having previously been blown with a nitrogen ($N_2$) gun to ensure that the surfaces were completely clear of small dust particles and pollutants that could alter the

dewetting process. Dewetting takes place because the surface energy of the ultrathin metal film is greater than the interfacial and surface energy of the underlying substrate. The RTA was carried out in a TsunamiTM RTP-600S system at a temperature of 700°C for 135 seconds, and high purity $N_2$ gas (1 atm pressure) was used to prevent oxidation of the metal film. The film's thickness and the dewetting parameters directly influence the size, height, and density of the formed Cu nanoparticles. After the RTA, diluted polyimide (CP1 Polyimide, Nexolve Materials) in N-methyl-2-pyrrolidone (NMP) was spin-coated over the sample, partially covering the metal dewetted nanoparticles – Figure 6.1(c). An APS (3-Aminopropyl)triethoxysilane) promoter was used to improve the PI layer's adhesion to the glass substrate[139]. By modifying the PI's concentration in the NMP solution and the spin coater parameters (G3P Spin Coater, Specialty Coating Systems), it is possible to control the thickness of the deposited film. Optimal results were achieved with a ratio of 1:3 of PI on NMP, with parameters of 6000 rpm and 90 seconds for the spin coating process. The curing of the polymeric film is critical to determine the final PI properties, with a two-step curing process being performed. First, the samples were cured at 100°C for 3 minutes and subsequently at 200 °C for 15 minutes, both steps being carried out on a hot plate (Cimarec Digital Hot Plate Stirrer, Thermo Scientific). After the curing process, the Cu nanoparticles were chemically etched with ammonium persulfate, resulting in a nanohole array structure being left on the surface of the PI film – Figure. 6.1(d).
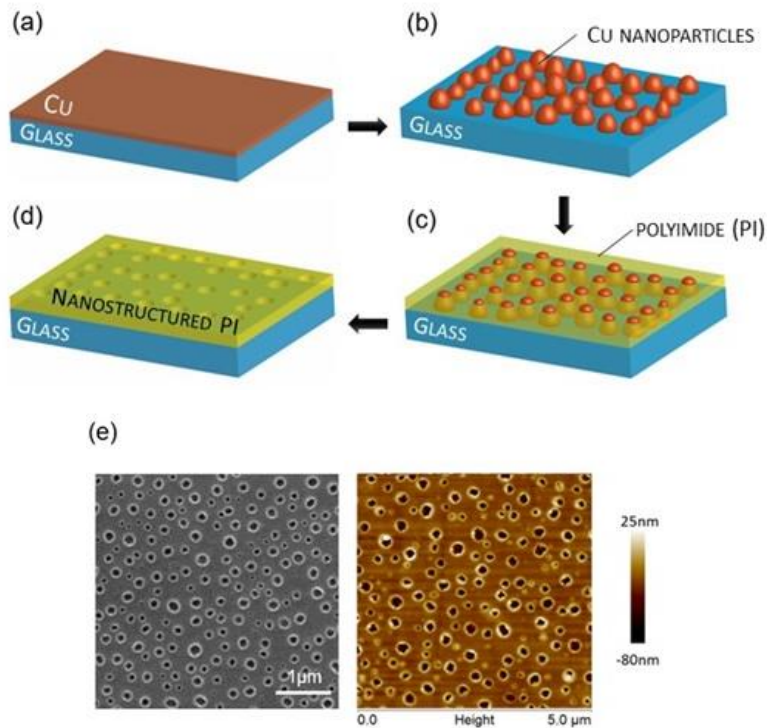
*Figure 6.1 Flow of the nanostructured polyimide fabrication process. An ultra-thin Cu film is deposited on a glass (fused silica) substrate by sputtering (a). Thermal dewetting creates Cu nano-particles (b) that are partially covered with spin coated polyimide (c). Finally, the Cu particles are removed by chemical etching, leading to a polyimide nanohole array (d). Scanning electron microscope (left) and atomic force microscope (right) images of the final polyimide nanohole array structure on glass (e).*

## 6.3 Simulations

Finite Element Method commercial software (COMSOL Multiphysics ®) was used to perform electromagnetic simulations. As discussed in the previous chapters, numerical calculations helped to study the proposed structures and quickly examine the optical effects of different designs to obtain the best possible results depending on the application requirements. The nanostructured PI on glass was simulated using periodic boundary conditions and modelled as a square cell with a central cavity. Parametric sweeps to optimise the structure were performed using dimensional analysis from SEM and profilometer measurements. Refractive index and absorption coefficients

of the PI, shown in Figure 6.2 (b.1), were calculated from the best fit from experimental transmission and reflection results for a flat (continuous) PI film on fused silica substrates. The fused silica refractive index plotted in Figure 6.2 (b.2) was taken from the Filmetrics.com refractive index database. The simulated nanocavity structure (3D model) with the software is represented in Figure 6.2 (a), the shape being a close approximation of the hole left after the removal of the dewetted nanoparticles.
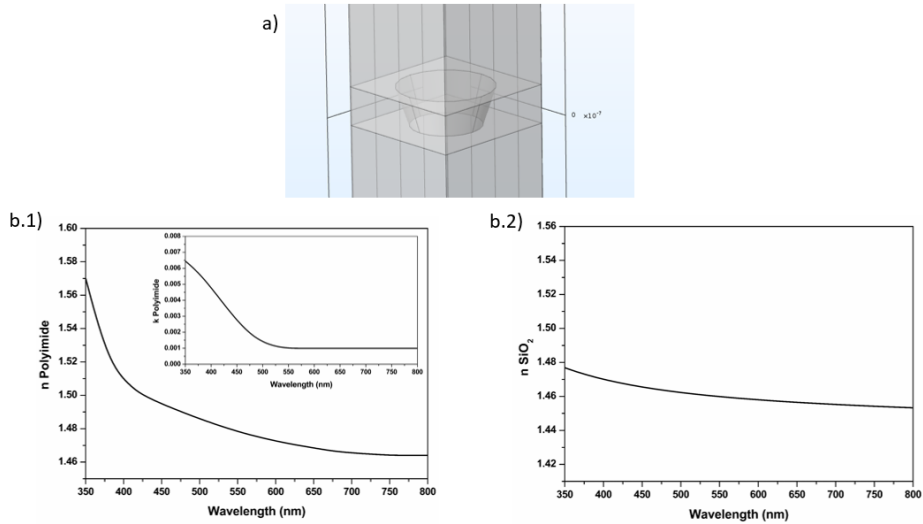


*Figure 6.2 Nanocavity structure simulated with COMSOL Multiphysics ® software (a). The shape is a close approximation of the hole left after removal of the dewetted nanoparticle. Refractive index and absorption coefficient (inset) of polyimide (b.1) and refractive index of fused silica substrate (b.2) used in the simulations.*

## 6.4 Optimisation

The PI thickness and the height of the metal nanoparticles are crucial factors in the success of creating nanostructures on PI films, and they also determine the depth of the cavities. If the metal nanoparticles are too short or the PI film too thick, the nanoparticles remain embedded in the film and cannot be removed by etching. The spin coating and the PI solutions were different for the two samples with different thicknesses shown in Figure 6.3, leading to sample (a) having the nanoparticles fully covered but not sample (b). After the same etching process, there was visual evidence that some Cu remained under the PI for sample (a). Due to its chemical resistance, PI can act as a barrier to the etchant and protects the Cu particles, which remain fully covered. From

scanning electron microscope (SEM) analysis, two different sample conditions can be seen: (i) sample where the spin-coated polyimide defined a thicker film, creating a protective cover that prevented the dewetted Cu from etching. In these regions, the nanoholes were not created successfully; (ii) sample where the polyimide evolved to create a thinner film, showing well-formed nanostructures, free of metal after the etching step. However, both parts had the same distribution (either of holes or Cu nanoparticles), demonstrating that it was the chemical etching of the nanoparticles that created the holes on the surface.

As discussed in previous chapters, the dewetted nanoparticles determine the size and distribution of the final nanostructures, particularly the nanoholes. Thus, it is crucial to evaluate the structure's optical response for different parametric combinations. Figure 6.4 shows the calculated average reflection for different sizes, densities and depths of the cavities. Once again, numerical calculations were used to optimise the fabrication process.
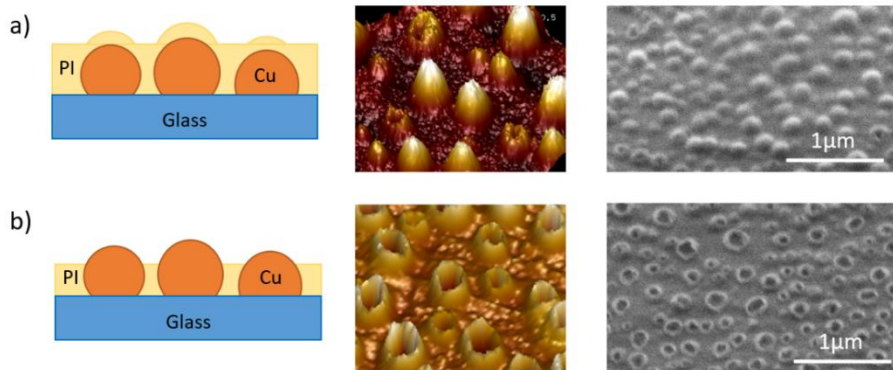


*Figure 6.3 Process control. Too small (low) dewetted Cu nanoparticles remain embedded inside the polyimide (PI) film and cannot be removed (a). Appropriate nanoparticles allow polyimide removal and formation of nanoholes (b). The samples are schematically represented (left) and characterized with an atomic force microscope (center) and a scanning electron microscope (right)*
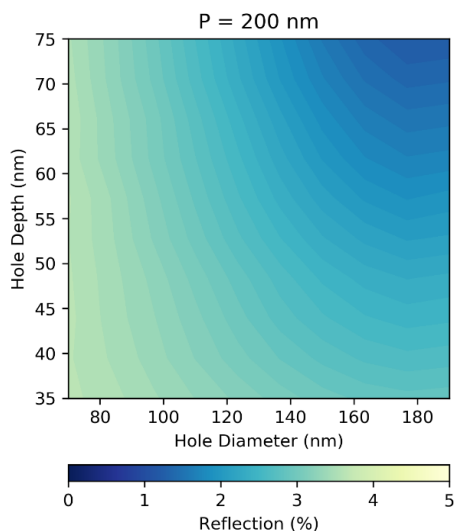
Figure 6.4 Simulated average reflection in the visible range (400-700nm) for different parametric combinations. Only one side was considered. Hole diameters from 70nm to 190nm and PI thickness from 35nm to 75nm were studied with a fixed period of 200nm.

The dewetting step and the PI's thickness were optimised according to the results of the simulations and the ease of removing the Cu nanoparticles with the ammonium persulfate. For optimal AR performance and low scattering, hole diameters from 130nm to 150nm were needed. By increasing the initial Cu film thickness to 15nm, larger nanoparticles were obtained (Figure 6.5) ensuring an adequate final nanohole diameter and the complete removal of the Cu.

a)                                    b)
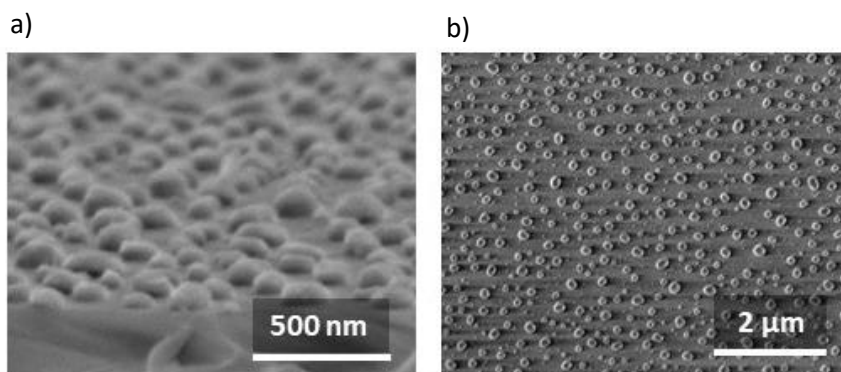


Figure 6.5 Scanning electron microscope images of a dewetted Cu film (15 nm thickness). Cross-section (a) and top view (b) of Cu nanoparticles.

## *6.5* Experimental Results

### 6.5.1 *Optical Performance*

Figure 6.6 shows the total transmission and reflection as a function of wavelength for bare glass, continuous PI and nanostructured PI on glass. All the samples had the same PI thickness (60 nm), determined from profilometry, and the fabrication variables of the nanostructure PI film are shown in Table 6.1. Due to the refractive index and absorption coefficient of PI, the addition of a continuous film reduced transmission and increased reflection of the coated fused silica substrate. After nanohole formation in the PI film, AR effects are clearly visible (Figure 6.6(b)), with transmission becoming higher than the initial fused silica substrate (Figure 6.6(a)). The incident light is reflected from both the top surface of the nanostructured PI film, and the interface between nanostructured PI film and the substrate. The reflected light beams interfere and, when the thickness of the PI film gets close to a quarter of the wavelength, the interference becomes destructive, thus minimising the reflection (inset of Figure 6.6(b)). The PI film has subwavelength nanostructures (nano-holes), leading to an effective refractive index, given by the volume ratio between air:PI. The effective refractive index determines the thickness that corresponds to the quarter-wave layer condition. Despite the fact that this condition is not completely achieved because of the lithographic limits of the PI thickness, the results are comparable with other polymer-based AR solutions[140–142] or nanostructured films on polymeric substrates[143], but without the need to use moulding or lithography processes.  In the future, full optimisation should be able to improve current performance even further.

*Table 6.1 Fabrication variables and average dimensions of the structure, measured with a scanning electron microscope.*

| Sample | Cu Film (nm) | RTP (°C) | Hole Diameter (nm) | Hole Depth (nm) |
|---|---|---|---|---|
| Nanostructured PI | 15 | 700 | 135 | 60 |

Results from full-wave electromagnetic simulations are also presented in Figure 6.6 in order to compare the measurements from the experimental samples with the theoretical model calculations. The average period (200 nm) and diameter (135 nm) of the nanohole PI structure were extracted from a statistical SEM analysis of the fabricated samples (Figure 6.7). As can be seen,

there is good agreement between experiment and simulation, which is essential for design optimisation.
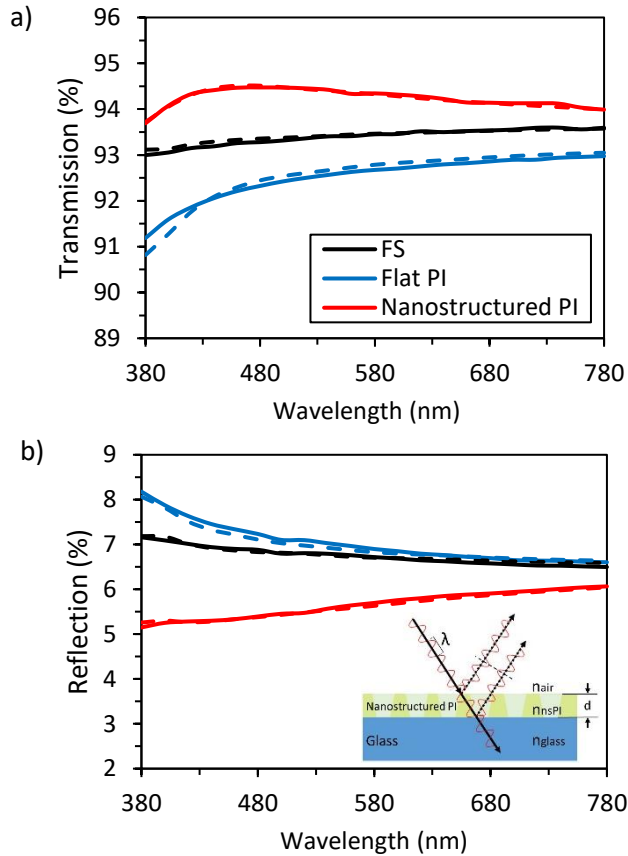


*Figure 6.6 Optical response of bare fused silica substrate (FS), flat (continuous) polyimide (Flat PI) and nanostructured polyimide (Nanostructured PI) on the same substrate. Measured direct transmission (a) and reflection (b) for the different structures. Experiment (continuous line) and simulation (dashed line). Note that only the front side is coated with PI and nanostructured PI. The inset shows a schematic view of the propagation of light rays through the nanostructured polyimide. The anti-reflective effect comes from the destructive interference created by the film, approximating a quarter-wave layer.*
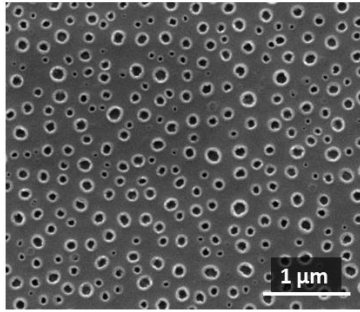
*Figure 6.7 Scanning electron microscope image of the nanostructured PI on a glass substrate.*

As shown in Figure 6.8, the AR response for different angles of incidence (AOI) was simulated for the nanostructured PI film on a fused silica substrate, and compared with a continue PI film of the same thickness, confirming that the one-sided reflection remains below about 7% up to an AOI of 60°.

A crucial parameter for optical surfaces is light scattering, usually quantified through the haze factor, and a low haze factor is required for many applications. For example, for high clarity requirements such as display sceen applications, it is preferable that haze is less than 0.1%. The average haze value and standard deviation for the proposed nanostructured PI on fused silica were 0.07%, very close to the instrument's detection limit. This confirms that reflected and transmitted lights are essentially direct, with minimal scattering. The decrease in transmission at shorter wavelengths is likely due to absorption in the PI layer.
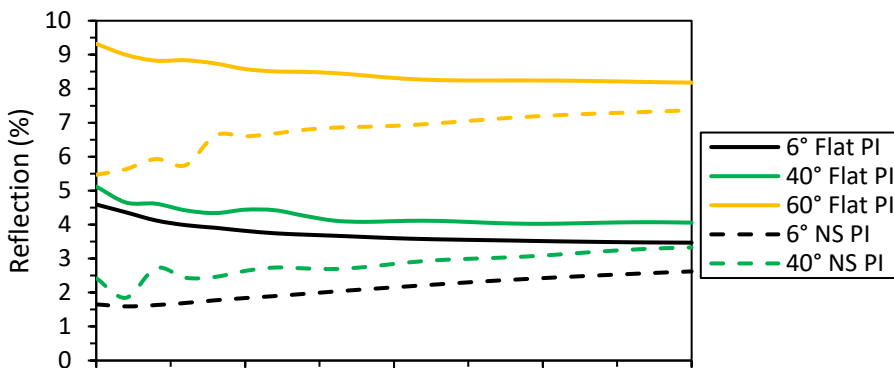


*Figure 6.8 Simulated angular dependence of the AR response with COMSOL Multiphysics® software of the nanostructured PI film on the fused silica substrate (NS PI) and a continuous PI film (Flat PI). One-sided reflection for different AOIs (6°, 40° and 60°). Note that the graphs in Figure 6.6 also included the flat back-side reflection.*

### 6.5.2  _Wettability_

The well-known Cassie-Baxter equation could describe the wetting property on the nanohole surface:

$$\cos\theta = f\cos\theta_1 + (1-f)\cos\theta_2 \qquad (1)$$

where $\theta$ is the contact angle of the composite state, f is the area fraction of the holes, and $\theta_1$ and $\theta_2$ are the Young contact angles on the hole and solid areas, respectively. As shown in Figure 6.9, the bare glass (fused silica) coated with continuous (flat) PI has a water contact angle of about $\theta_1 = 100°$.  After nanostructuring the polyimide film, the underlying substrate could be clean glass, for which the Young contact angle is lower. In the limiting case of ultra-clean glass ($\theta_2 = 0°$) the contact angle of the composite state according to equation (1) is $\theta \sim 77°$, corresponding to f = 0.33, which is the reason behind the reduction of the contact angle after the formation of the nanoholes. As in previous chapters, the surfaces were coated with a self-assemble monolayer fluorosilane. After the functionalisation step, the Young contact angle of the glass is $\theta_1 = 120°$, but there is uncertainty with respect to where the droplet meniscus resides in this configuration. However, the contact angles for the two limiting cases - (1) where meniscus fully wets the holes and (2) where meniscus is suspended on the holes - can be calculated, being 103° and 113°, respectively, according to equation 1. Note that larger contact angles are required to achieve super-hydrophobicity and, eventually, self-cleaning properties. In the future, this may be possible by increasing the void fraction of the current nanohole structure and the chemical affinity between the fluorosilane coating and the PI material.
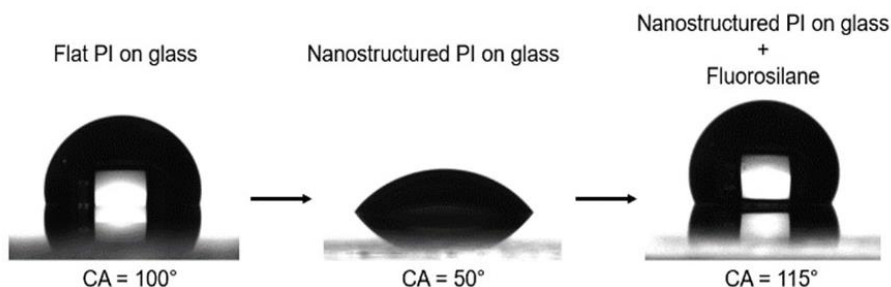


_Figure 6.9 Wetting characterisation. Comparison between bare glass (fused silica) substrate with flat polyimide (PI), nanostructured PI and nanostructured PI coated with fluorosilane._

### 6.5.3 _Mechanical Resistance_

Next, the mechanical durability of the nanostructured surface was investigated. Figure 6.10 shows the effect of a crockmeter test on the proposed hybrid PI glass nanostructured surface. As can be seen from comparing SEM images and the optical characterisation before and after more than 1,000 crockmeter repetitions with a constant load pressure of 4,5N/cm$^2$, the PI nanostructure remains practically unchanged. The proven surface durability is due to the well-known PI mechanical strength and the fact that the bonding force between the PI film and the fused silica substrate was increased by using an adhesion promoter (3-Aminopropyl) triethoxysilane (APTES). The mechanical resistance test indicates a strong adhesion between the nanostructured PI film and the substrate underneath, especially considering that nanostructuring reduces the available surface area for adhesion of the PI to the substrate and may also weaken the cohesive strength of the film. In the nanostructured PI on ITO coated glass substrate, the PI also acts as a protective layer for the ITO, maintaining its electrical conductivity. Besides being resistant, the PI film is mechanically flexible. Therefore, the proposed nanostructured PI film can easily be applied to flexible substrates, such as ultrathin glass, thereby achieving AR surfaces on a completely flexible platform.

a)

b)



c)
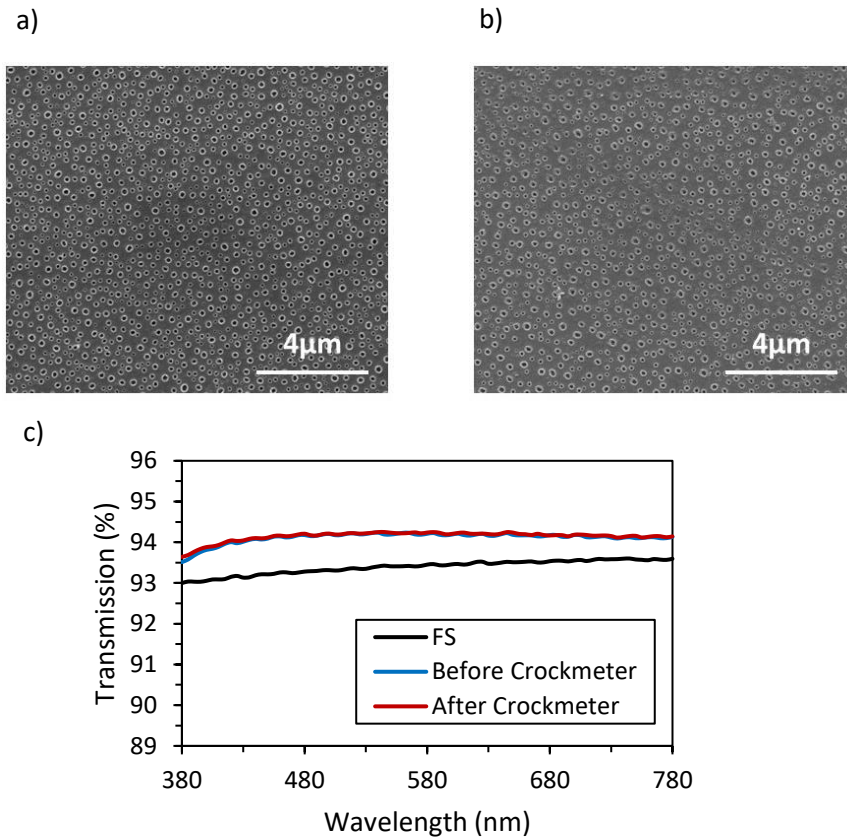


*Figure 6.10 Mechanical durability of the anti-reflective PI film on glass with a crockmeter. SEM images before (a) and after (b) more than 1000 repetitions carried out with standard 4.5N/cm² pressure using standard crockmeter cloth. The fact that the sample passes the test is also confirmed by optical transmission measurements (c).*

### 6.5.4    *Possible Applications*

The proposed hybrid-material surface nanostructuring process is versatile and could be applied to a large variety of substrate materials for use in different applications. Its use for ITO coated glass (fused silica) substrates is shown as a prototypical example. ITO-based transparent conductive surfaces are key in many optoelectronic devices where electrical signals need to be generated or collected with high optical transmission, for example, light-emitting diodes, solar cells, smart windows and liquid crystal displays. The nanostructuring of the PI film was carried out in the same way as described in the method section for the glass (fused silica) substrate, and the ITO thickness was 100 nm. As

shown in Figure 6.11, the AR effects are significant, leading to a greatly reduced reflection over almost the entire visible wavelength range and, correspondingly, a transmission larger than the initial ITO on glass substrates. In addition, the entire process essentially maintains the electrical conductivity of the ITO layer (lower than 20 ohm/sq).

The angular dependence of the AR response of the nanostructured PI film on fused silica substrates and on ITO on fused silica substrates was also simulated (Figure 6.12), and confirmed that the one-sided reflection remains below about 16% up to an AOI of 60°.
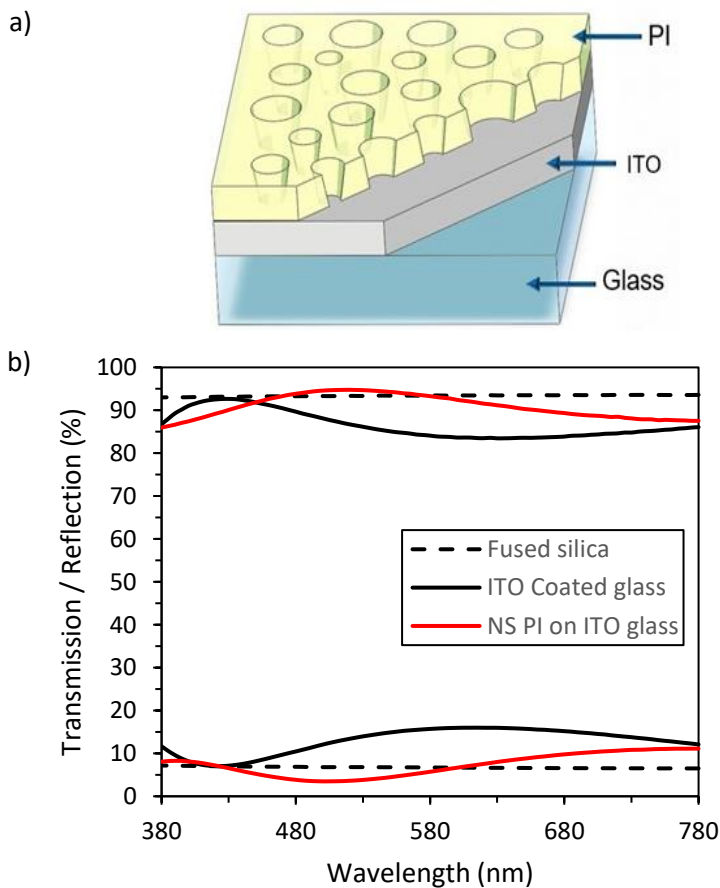


*Figure 6.11 Schematic illustration of the proposed nanostructured polyimide (NS PI) on an indium tin oxide (ITO) coated glass structure (a). Corresponding optical transmission and reflection. Measurements for glass (fused silica) and ITO coated glass substrates are also shown for comparison (b)*
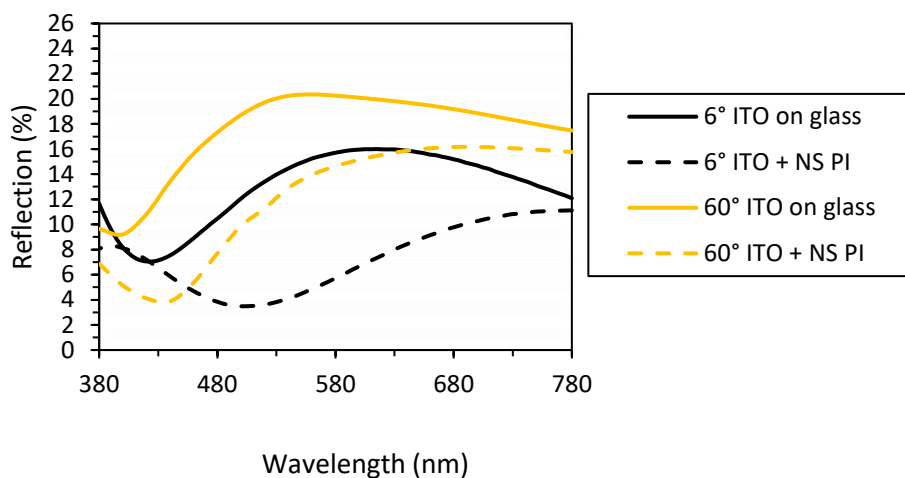
*Figure 6.12 Simulated angular dependence of the AR response with COMOSL Multiphysics® software of the nanostructured PI film on deposited ITO on the fused silica substrate. One-sided reflection for different AOIs (6° and 60°). Note that graphs in Figure 6.4 also included the flat back-side reflection*

## 6.6 Conclusions

A hybrid-material nanostructured optical surface, namely a polyimide film with nanohole geometry, which possesses significant antireflection properties, together with low scattering, high transparency and mechanical durability, has been demostated. It can be fabricated using inexpensive, lithography-free and scalable metal dewetting techniques. The combination of all these features make the newly developed optical surface relevant for a wide range of applications, such as windows for photovoltaic cells, photodetectors, display screens and optical components for remote sensing. As an example which could be utilised to fabricate transparent heaters, the proposed nanostructured polyimide film could effectively improve the optical performance of a commercially available transparent and conductive ITO coated glass substrate without affecting the electrical properties.

# 7

# Conclusions & Outlook

The performance of most optoelectronic devices relies on the efficiency of the light management of its surfaces. Combining improved optical properties with additional functionalities, such as self-cleaning, could have a significant impact in multiple applications, including display screens, solar cells and sensors. This thesis has been focused on the development of new designs and nanofabrication techniques to create multifunctional optical surfaces through cost-effective and reliable methods.

The main outcomes of the work carried out in this study are summarised below.

In Chapter 3, chemically strengthened glass was structured, mimicking the surface of a moth's eyes with an array of uniformly distributed nanopillars with heights of between 150nm and 400nm, designed to operate in different wavelength ranges. The method used was based on the dewetting phenomenon, where ultra-thin metal films can be transformed into nanoparticles following a rapid thermal annealing process. These particles were used as a mask in a dry etching process to pattern the glass surface. The refractive index gradient induced by the subwavelength dimensions and the conical shape of the nanopillars created produce an optimal anti-reflective (AR) effect, thus increasing the transmission while maintaining low levels of scattering (<0.1% in the visible region). Compared with commercially available

multilayer coatings, the most remarkable features are the broadband wavelength operation, and the improved AR properties at large angles of incidence (AOI) while keeping the reflection values below 0.5% (each face) up to an AOI of 40°. Moreover, by functionalising the surface of the nanostructured glass with self-assembled monolayer molecules, superhydrophobic or superhydrophilic states were successfully achieved. Additionally, the structure passed durability tests (crockmeter and weathering), proving its resistance against mechanical wear and extreme environmental conditions, and demonstrating its practical applicability.

Chapter 4 proposed a new multifunctional surface on glass substrates, based on a combination of antireflective multilayer coatings (ML) and self-cleaning bio-inspired nanostructures (NS). AR-ML coatings can be designed to operate in different wavelength ranges, from the ultraviolet to the near-infrared regions. Although their flat surface presents reasonable mechanical resistance against wear, they cannot achieve superhydrophobic behaviour. The aim of this work was to add nanostructures on the top layer maintaining the AR properties and providing self-cleaning capabilities. In fact, the experimental results, supported by theoretical studies, demonstrated that the AR effect was not only maintained, but actually improved by the NS, widening the operational wavelength ranges and giving better angular response, while bringing in new functionalities to the surface. The height of the nanostructure was kept as short as possible to maximise the mechanical durability while maintaining a superhydrophobic surface. The deposition of the different layers was performed using well-known industrial techniques such as sputtering, and the nanopillar fabrication followed the same method introduced in Chapter 3.

Transparent and oleophobic surfaces with nanocavities were presented in Chapter 5. Two novel nanofabrication methods, based on the Langmuir-Blodgett technique and the dewetting phenomenon, were developed to obtain subwavelength nanohole structures on glass substrates. Optically, the structures were optimised to operate in the visible region. The experimental results demonstrate remarkable anti-reflective properties created by the effective refractive index profile of the nanostructured layer. As a result, the optical transmission was also enhanced, and a full optimisation of the design was performed to maintain low scattering values and ensure the maximum clarity of the surfaces. In respect of the wetting characteristics, the phobic

behaviour of the surfaces was characterised with oleic acid and hexadecane, and is attributed to the pressure generated by the air trapped in the cavities underneath the liquid, and is considered a partial wetting state. In addition, the structure presents excellent mechanical resistance due to its geometry, which makes the proposed design and fabrication techniques interesting for many industrial applications.

Chapter 6 focused on organic materials, and a new technique to nanostructure thin films of polyimide (PI) was introduced. The surfaces of thin PI films were nanostructured with a nanohole geometry using cost-effective methods and based on dewetting ultra-thin metal films into nanoparticles. The feature size achieved was below 100nm, which indicates the high resolution of the technique, and samples of 5x5cm were nanostructured, showing good uniformity for large-area processing. As demonstrated in this chapter, the resulting structures not only improved the optical properties of non-structured films of PI, but, rather, the nanostructured films were able to act as an AR coating for the glass substrates, and even for transparent electrodes made of Indium Tin Oxide. In addition, PI is well known for its mechanical durability, and the structure showed good resistance against the abrasion tests performed. The combination of all these features makes this structure relevant for a wide range of applications, such as windows for photovoltaic cells, photodetectors and optical components for remote sensing. The method could also be used for other polymers, introducing new opportunities for flexible nanostructured surfaces, for example.

In summary, this thesis has presented diverse alternatives for the creation of multifunctional transparent materials through the modification of their surfaces at the nanoscale. Different nanostructure designs have been proposed in order to optimise the performance of different optoelectronic devices, with enhanced optical and wetting characteristics. The new nanofabrication techniques introduced in this study have been developed and fully optimised to be industrially feasible, and the successful results obtained have made the methods proposed patent-protected.

Despite the results achieved so far, and the continued efforts from the research community towards the development of new nanofabrication techniques for optical surfaces, there is still further room for improvement in several areas. Future work should focus on the study and implementation of nanostructures on flexible substrates, due to the increasing demand for

devices with such characteristics. Nanostructured curved surfaces are another field of great interest for their potential applicability. The effect of nanostructures on the performance of lenses is also something that should be investigated in depth. Moreover, further studies related to the mechanical resistance of nanostructures should be conducted, as this is one of the critical aspects for the implementation of such structures on touchable displays, for example. Methods to protect the structure or make it more durable would be of great importance for future applications.

# Bibliography

(1)     Parker, A. R.; Townley, H. E. Biomimetics of Photonic Nanostructures. *Nat. Nanotechnol.* **2007**, *2*, 347–353. https://doi.org/10.1038/nnano.2007.152.

(2)     Wilson, S. J.; Hutley, M. C. The Optical Properties of "Moth Eye" Antireflection Surfaces. *Opt. Acta Int. J. Opt.* **1982**, *29* (7), 993–1009. https://doi.org/10.1080/713820946.

(3)     Cai, J.; Qi, L. Recent Advances in Antireflective Surfaces Based on Nanostructure Arrays. *Mater. Horizons* **2015**, *2* (1), 37–53. https://doi.org/10.1039/c4mh00140k.

(4)     Bhushan, B.; Jung, Y. C. Natural and Biomimetic Artificial Surfaces for Superhydrophobicity, Self-Cleaning, Low Adhesion, and Drag Reduction. *Prog. Mater. Sci.* **2011**, *56* (1), 1–108. https://doi.org/10.1016/j.pmatsci.2010.04.003.

(5)     Ji, S.; Song, K.; Nguyen, T. B.; Kim, N.; Lim, H. Optimal Moth Eye Nanostructure Array on Transparent Glass towards Broadband Antireflection. *ACS Appl. Mater. Interfaces* **2013**, *5* (21), 10731–10737. https://doi.org/10.1021/am402881x.

(6)     Han, G.; Nguyen, T.-B.; Park, S.; Jung, Y.; Lee, J.; Lim, H. Moth-Eye Mimicking Solid Slippery Glass Surface with Icephobicity, Transparency, and Self-Healing. *ACS Nano* **2020**, *14* (8), 10198–10209. https://doi.org/10.1021/acsnano.0c03463.

(7)     Stavenga, D. G.; Foletti, S.; Palasantzas, G.; Arikawa, K. Light on the Moth-Eye Corneal Nipple Array of Butterflies. **2006**, No. December 2005, 661–667. https://doi.org/10.1098/rspb.2005.3369.

(8)     Gombert, A.; Bläsi, B. The Moth-Eye Effect — From Fundamentals to Commercial Exploitation. **2009**, *pp*, 79–102. https://doi.org/https://doi.org/10.1142/9789812837028_0004.

(9)     Bernhard, C. G. Strukturelle Und Funktionelle Adaptation in Einem Visuellen System. *Endeavour* **1967**, *26* (pp), 79–84.

(10)    Clapham, P.B.;Hutley, M. C. Reduction of Lens Reflexion by the "Moth Eye" Principle. *Nature1* **1973**, *244* (pp), 281–282. https://doi.org/https://doi.org/10.1038/244281a0.

(11)    Vukusic, P.;Sambles, J. R. Photonic Structures in Biology. *Nature* **2003**, *424* (pp), 852–855. https://doi.org/https://doi.org/10.1038/nature01941.

(12)    Vukusic, P; Sambles, J.R.;Wootton, R. J. Quantified Interference and Diffraction in Single Morpho Butterfly Scales. *Proc. R. Soc. Biol. Sci.* **1999**, *21* (pp), 1403–1411. https://doi.org/https://doi.org/10.1098/rspb.1999.0794.

(13)    Siddique, R. H.; Diewald, S.; Leuthold, J.; Holscher, H. Theoretical and Experimental Analysis of the Structural Pattern Repsonsible for the Iridescence of Morpho Butterflies. *Opt. Express* **2013**, *21* (pp), 14351–14361. https://doi.org/https://doi.org/10.1364/OE.21.014351.

(14)    Gao, L.; McCarthy, T. J. The "Lotus Effect" Explained: Two Reasons Why Two Length Scales of Topography Are Important. *Langmuir* **2006**, *22* (7), 2966–2967. https://doi.org/10.1021/la0532149.

(15)    Ensikat, H. J.; Ditsche-Kuru, P.; Neinhuis, C.; Barthlott, W. Superhydrophobicity in Perfection: The Outstanding Properties of the Lotus Leaf. *Beilstein J. Nanotechnol.* **2011**, *2* (1), 152–161. https://doi.org/10.3762/bjnano.2.19.

(16)    Barthlott, W.; Neinhuis, C. Purity of the Sacred Lotus, or Escape from Contamination in Biological Surfaces. *Planta* **1997**, *202* (1), 1–8. https://doi.org/10.1007/s004250050096.

(17)    Rayleigh, J. S. On Reflection of Vibrations. *Proc. London Math. Soc.* **1880**, *s1-11*, 51–56.

(18)    Born, M.; Wolf, E. *Principles Of Optics*, 4th ed.; Pergamon Press: Oxford, 1970.

(19)    Dobrowolski, J. A.; Poitras, D.; Ma, P.; Vakil, H.; Acree, M. Toward Perfect Antireflection Coatings: Numerical Investigation. *Appl. Opt.* **2002**, *41* (16), 3075. https://doi.org/10.1364/AO.41.003075.

(20)    Keshavarz Hedayati, M.; Elbahri, M. Antireflective Coatings: Conventional Stacking Layers and Ultrathin Plasmonic Metasurfaces, A Mini-Review. *Materials (Basel).* **2016**, *9(6)*, 497. https://doi.org/https://doi.org/10.3390/ma9060497.

(21)    Shimomura, H.; Gemici, Z.; Cohen, R. E.; Rubner, M. F. Layer-by-Layer-Assembled High-Performance Broadband Antireflection Coatings. *ACS Appl. Mater. Interfaces* **2010**, *2* (3), 813–820. https://doi.org/10.1021/am900883f.

(22)     Steck, D. A. *Thin Films*; 2015.

(23)     Lee, S. E., Choi, S. W., and Yi, J. Double-Layer Anti-Reflection Coating Using MgF2 and CeO2 Films on a Crystalline Silicon Substrate. *Thin Solid Films* **2000**, *376* (pp), 208–213. https://doi.org/https://doi.org/10.1016/S0040-6090(00)01205-0.

(24)     Raut, H. K.; Ganesh, V. A.; Nair, A. S.; Ramakrishna, S. Anti-Reflective Coatings: A Critical, in-Depth Review. *Energy Environ. Sci.* **2011**, *4* (10), 3779–3804. https://doi.org/10.1039/c1ee01297e.

(25)     Buskens, P.; Burghoorn, M.; Mourad, M. C. D.; Vroon, Z. Antireflective Coatings for Glass and Transparent Polymers. *Langmuir* **2016**, *32* (27), 6781–6793. https://doi.org/10.1021/acs.langmuir.6b00428.

(26)     Khan, S. B.; Wu, H.; Huai, X.; Zou, S.; Liu, Y.; Zhang, Z. Mechanically Robust Antireflective Coatings. *Nano Res.* **2018**, *11* (3), 1699–1713. https://doi.org/10.1007/s12274-017-1787-9.

(27)     Garlisi, C.; Trepci, E.; Li, X.; Al Sakkaf, R.; Al-Ali, K.; Nogueira, R. P.; Zheng, L.; Azar, E.; Palmisano, G. Multilayer Thin Film Structures for Multifunctional Glass: Self-Cleaning, Antireflective and Energy-Saving Properties. *Appl. Energy* **2020**, *264* (February). https://doi.org/10.1016/j.apenergy.2020.114697.

(28)     J.-Q. Xi, Martin F. Schubert, Jong Kyu Kim, E. Fred Schubert, Minfeng Chen, Shawn-Yu Lin, W. L. & J. A. S. Optical Thin-Film Materials with Low Refractive Index for Broadband Elimination of Fresnel Reflection. *Nat. Photonics* **2007**, *1*, 176–179. https://doi.org/https://doi.org/10.1038/nphoton.2007.26.

(29)     Xi, J.; Schubert, Q.; Martin, F.; Kim, J. K.; Schubert, E. F.; Chen, M.; Lin, S. Y.; Liu, W.; Smart, J. A. Optical Thin-Film Materials with Low Refractive Index for Broadband Elimination of Fresnel Reflection. *Nat. Photonics* **2007**, *1* (3), 176–179. https://doi.org/10.1038/nphoton.2007.26.

(30)     Lohmüller, T.; Helgert, M.; Sundermann, M.; Brunner, R.; Spatz, J. Biomimetic Interfaces for High-Performance Optics in the Deep-UV Light Range,. *Nano Lett.* **2008**, *8* (pp), 1429–1433. https://doi.org/https://doi.org/10.1021/nl080330y.

(31)     Lohmüller, T.; Brunner, R.; Spatz, J. P. Improved Properties of Optical Surfaces by Following the Example of the 'Moth Eye.' *InTech* **2010**, 451–466. https://doi.org/10.5772/8782.

(32)     Brunner, R.; Sandfuchs, O.; Pacholski, C.; Morhard, C.; Spatz, J. Lessons from Nature: Bio-Mimetic Subwavelength Structures for High-Performance OpticsNo Title. *Laser Phot. Rev* **2011**, *6* (pp), 641–659. https://doi.org/https://doi.org/10.1002/lpor.201100011.

(33)     Ko, D.-H., Tumbleston, J. R., Henderson, K. J., Euliss, L. E., DeSimone, J. M., Lopez, R., and Samulski, E. T. Biomimetic Microlens Array with Antireflective 'Moth-Eye' Surface. *Soft Matter* **2011**, *7* (pp), 6404–6407. https://doi.org/DOI https://doi.org/10.1039/C1SM05302G.

(34)     Auzelyte, V.; Flauraud, V.; Cadarso, V. J.; Kiefer, T.; Brugger, J. Biomimetic Soft Lithogra-Phy on Curved Nanostructured Surfaces. *Microelectron. Eng.* **2010**, *97* (pp), 269–271. https://doi.org/https://doi.org/10.1016/j.mee.2012.03.013.

(35)     Rao, J., Winfield, R., and Keeney, L. Moth-Eye-Structured Light-Emitting Diodes. *Opt. Commun.* **2010**, *283* (pp), 2446–2450. https://doi.org/doi:10.1016/j.optcom.2010.01.056.

(36)     Lohmüller, T.; Aydin, D.; Schwieder, M.; Morhard, C.; Louban, I.; Pacholski, C.; Spatz, J. P. Nanopatterning by Block Copolymer Micelle Nanolithography and Bioinspired Applications. **2011**, No. March, 27–29. https://doi.org/10.1116/1.3536839.

(37)     Southwell, W. H. Pyramid-Array Surface-Relief Structures Producing Antireflection Index Match-Ing on Optical Surfaces. *J. Opt. Soc. Am.* **1991**, *8* (pp), 549–553. https://doi.org/https://doi.org/10.1364/JOSAA.8.000549.

(38)     Frederick M. Fowkes. Attractive Forces at Interfaces. *Ind. Eng. Chem.* **1964**. https://doi.org/https://doi.org/10.1021/ie50660a008.

(39)     Kendall K.L.; Johnson, K. .; Roberts, A. D. Surface Energy and the Contact of Elastic Solids. In Proceedings of the Royal Society of London A: Mathematical, Physical and Engineering Sciences. *R. Soc.* **1971**, *324*, 301–313. https://doi.org/10.1098/rspa.1971.0141.

(40)     F.A. Cotton; G. Wilkinson; P.L. Gaus. *Basic Inorganic Chemistry*; 1976.

(41)     Fort, P; Roura, J. Local Thermodynamic Derivation of Young's Equation. *J. Colloid Interface Sci.* **2004**, *272* (2), 420–429. https://doi.org/10.1016/j.jcis.2004.01.028.

(42)     L. Feng; S. Li; Y. Li; H. Li; L. Zhang; J. Zhai; Y. Song; B. Liu; L. Jiang. Super-Hydrophobic Surfaces: From Natural to Artificial. *Adv. Mater.* **2002**, *14* (24), 1857–1860. https://doi.org/10.1002/adma.200290020.

(43) Yuehua, Y.; Randall, L. Contact Angle and Wetting Properties. *Surf. Sci.* **2013**. https://doi.org/10.1007/978-3-642-34243-1_1.

(44) Young, T. An Essay on the Cohesion of Fluids. Philosophical Transactions of the Royal Society of London. *Philos. Trans. R. Soc. London* **1805**, *95*, 65. https://doi.org/10.1098/rstl.1805.0005.

(45) Yixiong, L.; German, R. M. Contact Angle and Solid-Liquid-Vapor Equilibrium. *Acta Mater.* **1996**, *44* (4), 1657–1663. https://doi.org/10.1016/1359-6454(95)00259-6.

(46) Gerald, H. M. Thermodynamics of Surfaces and Interfaces: Concepts in Inorganic Materials. *Cambridge Univ. Press* **2014**. https://doi.org/10.1017/CBO9781139047029.

(47) Xiu, Y. *Fabrication of Surface Micro-and Nanostructures for Superhydrophobic Surfaces in Electric and Electronic Applications.*; 2008.

(48) Li, X.; Reinhoudt, D.; Crego-Calama, M. What Do We Need for a Superhydrophobic Surface? A Review on the Recent Progress in the Preparation of Superhydrophobic Surfaces. *R. Soc. Chem.* **2007**. https://doi.org/10.1039/B602486F.

(49) Nakajima, A.; Hashimoto, K.; Watanabe., T. Recent Studies on Superhydrophobic Films. *Monatshefte für Chemie/Chemical Mon.* **2001**, *132* (1), 31–41.

(50) Whyman, G.; Bormashenko, E.; Tamir, S. The Rigorous Derivation of Young, Cassie–Baxter and Wenzel Equations and the Analysis of the Contact Angle Hysteresis Phenomenon. *Chem. Phys. Lett.* **2008**, *450* (4), 355–359. https://doi.org/10.1016/j.cplett.2007.11.033.

(51) Quere, A. L. and D. Superhydrophobic States. *Nat. Mater.* **2003**, *2* (7), 457–460. https://doi.org/10.1038/nmat924.

(52) Fort, P.; Roura, J. Comment on Effects of the Surface Roughness on Sliding Angles of Water Droplets on Superhydrophobic Surfaces. *Langmuir* **2002**, *18* (2), 566–569. https://doi.org/10.1021/la991660o.

(53) Friedrich-wilhelms, R. Micro- , Nano- and Hierarchical Structures for Superhydrophobicity , Self-Cleaning and Low Adhesion. **2009**, No. March, 1631–1672. https://doi.org/10.1098/rsta.2009.0014.

(54) De Gennes, P. G.; Brochard-Wyart, F.; Quere, D. Capillarity and Wetting Phenomena: Drops, Bubbles, Pearls, Waves. *Springer Sci. Bus. Media*

**2013**. https://doi.org/10.1007/978-0-387-21656-0.

(55)   Wenzel, R. N. Surface Roughness and Contact Angle. *Ind. Eng. Chem* **1936**, *No. 28*, 988–994. https://doi.org/10.1021/ie50320a024.

(56)   Cassie, A. B.; Baxter, S. Wettability of Porous Surface. *Trans. Faraday Soc.* **1944**, *40*, 546–551. https://doi.org/10.1039/TF9444000546.

(57)   Han, Z. W.; Wang, Z.; Feng, X. M.; Li, B.; Mu, Z. Z.; Zhang, J. Q.; Niu, S. C.; Ren, L. Q. Antire Fl Ective Surface Inspired from Biology : A Review. **2016**, *2* (5988), 137–150. https://doi.org/10.1016/j.bsbt.2016.11.002.

(58)   Nishimoto, S.; Bhushan, B. Bioinspired Self-Cleaning Surfaces with Superhydrophobicity, Superoleophobicity, and Superhydrophilicity. *RSC Adv.* **2013**, *3* (3), 671–690. https://doi.org/10.1039/c2ra21260a.

(59)   Oh, S. S.; Choi, C. G.; Kim, Y. S. Fabrication of Micro-Lens Arrays with Moth-Eye Antireflective Nanostructures Using Thermal Imprinting Process. *Microelectron. Eng.* **2010**, *87* (11), 2328–2331. https://doi.org/10.1016/j.mee.2010.03.012.

(60)   Jiang, L.; Zhao, Y.; Zhai, J. A Lotus-Leaf-like Superhydrophobic Surface: A Porous Microsphere/Nanofiber Composite Film Prepared by Electrohydrodynamics. *Angew. Chemie Int. Ed.* **2004**, *43* (33), 4338–4341. https://doi.org/10.1002/anie.200460333.

(61)   Ohring, M. *Materials Science of Thin Films - 2nd Edition*; 2001.

(62)   Cai, J.; Qi, L. Recent Advances in Antireflective Surfaces Based on Nanostructure Arrays. *Mater. Horizons* **2015**, *2* (1), 37–53. https://doi.org/10.1039/c4mh00140k.

(63)   Glass, R.; Martin, M.; Spatz, J. P. Block Copolymer Micelle Nanolithography. **2003**, *14*, 1153–1160.

(64)   Chao, Y.; Chen, C.; Lin, C.; Dai, Y.; He, J. Antireflection Effect of ZnO Nanorod Arrays. **2010**, 8134–8138. https://doi.org/10.1039/c0jm00516a.

(65)   Chen, Y. Review Nanofabrication : Conventional and Nonconventional Methods Miniaturization. **2001**. https://doi.org/https://doi.org/10.1002/1522-2683(200101)22:

(66)   Chang, Y.; Liu, R.; Fang, S. EUV and E-Beam Manufacturability : Challenges and Solutions Categories and Subject Descriptors. https://doi.org/10.1145/2744769.2747925.

(67) Seo, J.; Park, J. H.; Ma, Z.; Choi, J.; Ju, B. Nanopatterning by Laser Interference Lithography : Applications to Optical Devices. No. Il. https://doi.org/10.1166/jnn.2014.9199.

(68) Farhoud, M.; Ferrera, J.; Lochtefeld, A. J.; Murphy, T. E.; Schattenburg, M. L.; Carter, J.; Ross, C. A.; Smith, H. I. Fabrication of 200nm Period Nanomagnet Arrays Using Interference Lithography and a Negative Resist. *J. Vac. Sci. Technol.* **1999**, *17* (6), 3182–3185. https://doi.org/10.1116/1.590976.

(69) Zhou, W.; Min, G.; Zhang, J.; Liu, Y.; Wang, J.; Zhang, Y.; Sun, F. Nanoimprint Lithography: A Processing Technique for Nanofabrication Advancement. *Nano-Micro Lett.* **2011**, *3* (2), 135–140. https://doi.org/10.1007/bf03353663.

(70) Chou, S. Y. Nanoimprint Lithography. *J. Vac. Sci. Technol. B* **1996**. https://doi.org/10.1116/1.588605.

(71) Cui, B.; Cortot, Y.; Veres, T. Polyimide Nanostructures Fabricated by Nanoimprint Lithography and Its Applications. *Microelectron. Eng.* **2006**, *83* (4-9 SPEC. ISS.), 906–909. https://doi.org/10.1016/j.mee.2006.01.014.

(72) Thompson, C. V. Solid-State Dewetting of Thin Films. **2012**. https://doi.org/10.1146/annurev-matsci-070511-155048.

(73) Leroy, F.; Borowik, L.; Cheynis, Y.; Almadori, S.; Trautmann, M.; Berbe, J. C.; Muller, P. How to Control Solid State Dewetting: A Short Review. *Surf. Sci. Rep.* **2016**, *71* (2), 391–409. https://doi.org/10.1016%2Fj.surfrep.2016.03.002.

(74) Thompson, C. V. Solid-State Dewetting of Thin Films. *Annu. Rev. Mater. Res.* **2012**, *42*, 399–434. https://doi.org/10.1146/annurev-matsci-070511-155048.

(75) Thompson, L.F. Wilson, C.G. Bowden, M. J. *Introduction to Microlithography*; 1994.

(76) Metwalli, E.; Pantano, C. . Reactive Ion Etching of Glasses: Composition Dependence. *Nucl. Instruments Methods Phys. Res. Sect.* **2003**, *207* (1), 21–27. https://doi.org/10.1016/S0168-583X(03)00517-2.

(77) Wilkinson, C. D. W.; Rahman, M. Dry Etching and Sputtering. *Philos. Trans. R. Soc. A Math. Phys. Eng. Sci.* **2004**, *362* (1814), 125–138. https://doi.org/10.1098/rsta.2003.1307.

(78)    Abe, H. Leclerc, M.A. Fujiwara, N. Developments of Plasma Etching Technology for Fabricating Semiconductor Devices. *Jpn. J. Appl. Phys.* **2008**, *47* (3), 1435–1455. https://doi.org/10.3390/mi12080991.

(79)    Ganesh, V. A.; Hemant Kumar Raut, A.; Naira, S.; Ramakrishna, S. A Review on Self-Cleaning Coatings. *J. Mater. Chem. A* **2011**, *21*, 16304–16322. https://doi.org/10.1039/C1JM12523K.

(80)    Brassard, J.; Sarkar, D. K.; Perron, J. Fluorine Based Superhydrophobic Coatings. **2012**, 453–464. https://doi.org/10.3390/app2020453.

(81)    IMARC group https://www.imarcgroup.com/flat-glass-market.

(82)    Hedayati, M. K.; Elbahri, M. Antireflective Coatings: Conventional Stacking Layers and Ultrathin Plasmonic Metasurfaces, a Mini-Review. *Materials (Basel).* **2016**, *9* (6). https://doi.org/10.3390/ma9060497.

(83)    Infante, D.; Koch, K. W.; Mazumder, P.; Tian, L.; Carrilero, A.; Tulli, D.; Baker, D.; Pruneri, V. Durable, Superhydrophobic, Antireflection, and Low Haze Glass Surfaces Using Scalable Metal Dewetting Nanostructuring. *Nano Res.* **2013**, *6* (6), 429–440. https://doi.org/10.1007/s12274-013-0320-z.

(84)    Zhang, D.; Gökce, B.; Barcikowski, S. Laser Synthesis and Processing of Colloids: Fundamentals and Applications. *Chem. Rev.* **2017**, *117* (5), 3990–4103. https://doi.org/10.1021/acs.chemrev.6b00468.

(85)    Lohani, B.; Ghosh, S. Airborne LiDAR Technology: A Review of Data Collection and Processing Systems. *Proc. Natl. Acad. Sci. India Sect. A Phys. Sci. Vol.* **2017**, *89*, 567–579. https://doi.org/10.1007/s40010-017-0435-9.

(86)    Han, Z. W.; Wang, Z.; Feng, X. M.; Li, B.; Mu, Z. Z.; Zhang, J. Q.; Niu, S. C.; Ren, L. Q. Antireflective Surface Inspired from Biology : A Review. **2016**, *2* (5988), 137–150. https://doi.org/10.1016/j.bsbt.2016.11.002.

(87)    Jeevahan, J.; Chandrasekaran, M.; Joseph, G. B.; Durairaj, R. B.; Mageshwaran, G. Superhydrophobic Surfaces : A Review on Fundamentals , Applications , and Challenges. *J. Coatings Technol. Res.* **2018**, *15* (2), 231–250. https://doi.org/10.1007/s11998-017-0011-x.

(88)    Scarratt, L. R. J.; Steiner, U.; Neto, C. A Review on the Mechanical and Thermodynamic Robustness of Superhydrophobic Surfaces. *Adv. Colloid Interface Sci.* **2017**, *246* (May), 133–152. https://doi.org/10.1016/j.cis.2017.05.018.

(89)    Born, M.; Wolf, E. *Principles Of Optics*; Perfamon Press, 1970.

(90)    Mazumder, P.; Jiang, Y.; Baker, D.; Carrilero, A.; Tulli, D.; Infante, D.; Hunt, A. T.; Pruneri, V. Superomniphobic, Transparent, and Antireflection Surfaces Based on Hierarchical Nanostructures. *Nano Lett.* **2014**. https://doi.org/10.1021/nl501767j.

(91)    Tulli, D.; Hart, S. D.; Mazumder, P.; Carrilero, A.; Tian, L.; Koch, K. W.; Yongsunthon, R.; Piech, G. A.; Pruneri, V. Monolithically Integrated Micro- and Nanostructured Glass Surface with Antiglare, Antire Fl Ection, and Superhydrophobic Properties. **2014**, 11198–11203. https://doi.org//10.1021/am5013062.

(92)    Liapis, A. C.; Rahman, A.; Black, C. T. Self-Assembled Nanotextures Impart Broadband Transparency to Glass Windows and Solar Cell Encapsulants. *Appl. Phys. Lett.* **2017**, *111* (18). https://doi.org/10.1063/1.5000965.

(93)    Pan, Z.; Cheng, F.; Zhao, B. Bio-Inspired Polymeric Structures with Special Wettability and Their Applications : An Overview. **2017**, 32–39. https://doi.org/10.3390/polym9120725.

(94)    Chen, J. Y.; Chang, W. L.; Huang, C. K.; Sun, K. W. Biomimetic Nanostructured Antireflection Coating and Its Application on Crystalline Silicon Solar Cells. *Opt. Express* **2011**, *15* (14411–14419). https://doi.org/10.1364/OE.19.014411.

(95)    Diao, Z.; Hirte, J.; Chen, W.; Spatz, J. P. Inverse Moth Eye Nanostructures with Enhanced Antireflection and Contamination Resistance. *ACS Omega* **2017**, *2* (8), 5012–5018. https://doi.org/10.1021/acsomega.7b01001.

(96)    Park, K. C.; Choi, H. J.; Chang, C. H.; Cohen, R. E.; McKinley, G. H.; Barbastathis, G. *Nanotextured Silica Surfaces with Robust Superhydrophobicity and Omnidirectional Broadband Supertransmissivity*; 2012; Vol. 6. https://doi.org/10.1021/nn301112t.

(97)    Rombaut, J.; Fernandez, M.; Mazumder, P.; Pruneri, V. Nanostructured Hybrid-Material Transparent Surface with Antireflection Properties and a Facile Fabrication Process. *ACS Omega* **2019**, *4* (22), 19840–19846. https://doi.org/10.1021/acsomega.9b02775.

(98)    Bhushan, B.; Nosonovsky, M. The Rose Petal Effect and the Modes of Superhydrophobicity. *Philos. Trans. R. Soc. A Math. Phys. Eng. Sci.* **2010**, *368* (1929), 4713–4728.

https://doi.org/10.1098/rsta.2010.0203.

(99)   Chen, F.; Zhang, D.; Yang, Q.; Wang, X.; Dai, B.; Li, X.; Hao, X.; Ding, Y.;
       Si, J.; Hou, X. Anisotropic Wetting on Microstrips Surface Fabricated by
       Femtosecond   Laser.   *Langmuir*   **2011**,   *27*   (1),   359–365.
       https://doi.org/10.1021/la103293j.

(100)  Rombaut, J.; Maniyara, R. A.; Bellman, R. A.; Acquard, D. F.; Baca, A. S.;
       Osmond, J.; Senaratne, W.; Quesada, M. A.; Baker, D.; Mazumder, P.;
       Pruneri,  V.  Antireflective  Transparent  Oleophobic  Surfaces  by
       Noninteracting Cavities. *ACS Appl. Mater. Interfaces* **2018**, *10*, 43230–
       43235. https://doi.org/10.1021/acsami.8b15507.

(101)  Peng, J.; Zhao, X.; Wang, W.; Gong, X. Durable Self-Cleaning Surfaces
       with Superhydrophobic and Highly Oleophobic Properties. *Langmuir*
       **2019**. https://doi.org/10.1021/acs.langmuir.9b01507.

(102)  Zhang, K.; Li, Z.; Maxey, M.; Chen, S.; Karniadakis, G. E. Self-Cleaning of
       Hydrophobic  Rough  Surfaces  by  Coalescence-Induced  Wetting
       Transition.   *Langmuir*   **2019**,   *35*   (6),   2431–2442.
       https://doi.org/10.1021/acs.langmuir.8b03664.

(103)  Nakajim, A.; Fujishima, A.; Hashimoto, K.; Watanabe, T. Preparation of
       Transparent  Superhydrophobic  Boehmite  and  Silica  Films  by
       Sublimation of Aluminum Acetylacetonate. *Adv. Mater.* **1999**, *11* (16),
       1365–1368. https://doi.org/10.1002/(SICI)1521-4095(199911).

(104)  Xu, L.; He, J. Fabrication of Highly Transparent Superhydrophobic
       Coatings from Hollow Silica Nanoparticles. *Langmuir* **2012**, *28* (19),
       7512–7518. https://doi.org/10.1021/la301420p.

(105)  Sun, Y.; Wang, L.; Gao, Y.; Guo, D. Preparation of Stable
       Superamphiphobic Surfaces on Ti-6Al-4V Substrates by One-Step
       Anodization.   *Appl.   Surf.   Sci.*   **2014**,   *324*,   825–830.
       https://doi.org/10.1016/j.apsusc.2014.11.047.

(106)  Tsujii, K.; Yamamoto, T.; Onda, T.; Shibuichi, S. Super Oil-Repellent
       Surfaces. *Angew. Chemie Int.* **1997**, *36* (9), 1011–1012.
       https://doi.org/10.1002/anie.199710111.

(107)  Shibuichi, S.; Yamamoto, T.; Onda, T.; Tsujii, K. Super Water- and Oil-
       Repellent Surfaces Resulting from Fractal Structure. *J. Colloid Interface
       Sci.* **1998**, *208* (1), 287–294. https://doi.org/10.1006/jcis.1998.5813.

(108)  H, Z.; Ma, M.; Lan, X.; Chen, F.; Wang, K.; Deng, H.; Zhang, Q.; Fu, Q.
       Fabrication of a Transparent Superamphiphobic Coating with Improved

Stability. *Soft Matter2* **2011**, *7* (14), 6435. https://doi.org/10.1039/C1SM05574G.

(109) Tuteja, A.; Choi, W.; Ma, M.; Mabry, J. M.; Mazzella, S. A.; Rutledge, G. C.; Mckinley, G.; H.; Cohen, R. E. Designing Superoleophobic Surfaces. *Sci. Reportscience* **2007**, *No. Decemb*, 1618–1623. https://doi.org/10.1126/science.1148326.

(110) Cao, L.; Hu, H.-H.; Gao, D. Design and Fabrication of Micro-Textures for Inducing a Superhydrophobic Behavior on Hydrophilic Materials. *Langmuir* **2007**, *23* (8), 4310–4314. https://doi.org/10.1021/la063572r.

(111) Im, M.; Im, H.; Lee, J.-H.; Yoona, J.-B.; Choi, Y.-K. A Robust Superhydrophobic and Superoleophobic Surface with Inverse-Trapezoidal Microstructures on a Large Transparent Flexible Substrate. *Soft Matter* **2010**, *6* (7), 1401–1404. https://doi.org/10.1039/B925970H.

(112) Zhu, X.; Zhang, Z.; Ren, G.; Men, X.; Ge, B.; Zhou, X. Designing Transparent Superamphiphobic Coatings Directed by Carbon Nanotubes. *J Colloid Interface Sci.* **2014**, *421*, 141–145.

(113) Deng, X.; Mammen, L.; Butt, H.-J.; Vollmer, D. Candle Soot as a Template for a Transparent Robust Superamphiphobic Coating. *Science (80-. ).* **2012**, *335* (6064), 67–70. https://doi.org/10.1126/science.1207115 Free article.

(114) Kang, S. M.; Kim, S. M.; Kim, H. N.; Kwak, M. K.; Tahk, D. H.; Suh, K. Y. Robust Superomniphobic Surfaces with Mushroom-like Micropillar Arrays. *Soft Matter* **2012**, *8* (33), 8563. https://doi.org/10.1039/C2SM25879J.

(115) Ganesh, V. A.; Dinachali, S. S.; Raut, H. K.; Walsh, T. M.; Nair, S.; Ramakrishna, S. Electrospun SiO2 Nanofibers as a Template to Fabricate a Robust and Transparent Superamphiphobic Coating. *RSC Adv.* **2013**, *3* (12), 3819. https://doi.org/10.1039/C3RA22968H.

(116) Le, S. G.; Ham, D. S.; Lee, D. Y.; Bong, H.; Cho, K. Transparent Superhydrophobic/Translucent Superamphiphobic Coatings Based on Silica-Fluoropolymer Hybrid Nanoparticles. *Langmuir* **2013**, *29* (48), 15051–15057. https://doi.org/10.1021/la404005b.

(117) Fukada, K.; Nishizaw, S.; Shiratori, S. Antifouling Property of Highly Oleophobic Substrates for Solar Cell Surfaces. *J. Appl. Phys.* **2014**, *115*

(10). https://doi.org/10.1063/1.4868316.

(118) Deng, X.; Schellenberger, F.; Papadopoulo, P.; Vollmer, D.; Butt, H.-J. Liquid Drops Impacting Superamphiphobic Coatings. *Langmuir* **2013**, *29* (25), 7847–7856. https://doi.org/10.1021/la401120j.

(119) Brown, P.; Bhushan, B. Mechanically Durable, Superomniphobic Coatings Prepared by Layer-by-Layer Technique for Self-Cleaning and Anti-Smudge. *J Colloid Interface Sci.* **2015**, *456*, 210–218. https://doi.org/10.1016/j.jcis.2015.06.030.

(120) Yuan, L.; Wu, T.; Zhang, W.; Ling, S.; Xiang, R.; Gui, X.; Zhua, Y.; Tang, Z. Engineering Superlyophobic Surfaces on Curable Materials Based on Facile and Inexpensive Microfabrication. *J. Mater. Chem. A2* **2014**, *2* (19), 6952–6959. https://doi.org/10.1039/C4TA00672K.

(121) Tuteja, A.; Choi, W.; Mabry, J. M.; McKinley, G. H.; Cohen, R. E. Robust Omniphobic Surfaces. *Proc. Natl. Acad. Sci.* **2008**, *105* (47), 18200–18205. https://doi.org/10.1073/pnas.0804872105.

(122) Cao, L.; Hu, H. A.; Gao, D. Design and Fabrication of Micro-Textures for Inducing a Superhydrophobic Behavior on Hydrophilic Materials. *Langmuir* **2007**, *23* (8), 4310–4314. https://doi.org/10.1021/la063572r.

(123) Hsieh, C.T.; Chen, J.M; Kuo, R.R.; Lin, T.S.; Wu, C. F. Influence of Surface Roughness on Water -and Oil - Repellent Surfaces Coated with Nanoparticles. *Appl. Surf. Sci.* **2005**, *240*, 318–326. https://doi.org/10.1016/j.apsusc.2004.07.016.

(124) Choi, H. J.; Choo, S.; Shin, J. H.; Kim, K. I.; Lee, H. Fabrication of Superhydrophobic and Oleophobic Surfaces with Overhang Structure by Reverse Nanoimprint Lithography. *J. Phys. Chem.* **2013**, *117* (46), 24354–24359. https://doi.org/10.1021/jp4070399.

(125) Brown, P. S.; Bhushan, B. Durable, Superoleophobic Polymer-Nanoparticle Composite Surfaces with Re-Entrant Geometry via Solvent-Induced Phase Transformation. *Sci. Rep.* **2016**, *6* (February), 1–11. https://doi.org/10.1038/srep21048.

(126) Kim, J.; Lin, P.; Kim, W. S. Mechanically Robust Super-Oleophobic Stamp for Direct Stamping of Silver Nanoparticle Ink. *Thin Solid Films* **2012**, *520* (13), 4339–4343. https://doi.org/10.1016/j.tsf.2012.02.070.

(127) Dufour, R.; Perry, G.; Harnois, M.; Coffinier, Y.; Thomy, V.; Senez, V.; Boukherroub, R. From Micro to Nano Reentrant Structures: Hysteresis

on Superomniphobic Surfaces. *Colloid Polym. Sci.* **2013**, *219* (2), 409–415. https://doi.org/10.1007/s00396-012-2750-7.

(128) Chen, L.; Guo, Z. Outmatching Superhydrophobicity: Bio-Inspired Re-Entrant Curvature for Mighty Superamphiphobicity in Air. *J. Mater. Chem.* **2017**, *No.* (February), 14480–14507. https://doi.org/10.1039/C7TA03248J.

(129) Pesse, A. V.; Warrier, G. R.; Dhir, V. K. An Experimental Study of the Gas Entrapment Process in Closed-End Microchannels. *J. Heat Mass Transf.* **2005**, *48* (25–26), 5150–5165. https://doi.org/10.1016/2005.07.020.

(130) Rombaut, J.; Martínez, S.; Matera, U. M.; Mazumder, P.; Pruneri, V. Antireflective Multilayer Surface with Self-Cleaning Subwavelength Structures. *ACS Photonics* **2021**. https://doi.org/10.1021/acsphotonics.0c01909.

(131) Gonzalez-Martinez, I. G.; Bachmatiuk, A.; Bezugly, V.; Kunstmann, J.; Gemming, T.; Liu, Z.; Cuniberti, G.; Rümmeli, M. H. Electron-Beam Induced Synthesis of Nanostructures: A Review. *Nanoscale* **2016**, *8* (22), 11340–11362. https://doi.org/10.1039/c6nr01941b.

(132) Matsui, S. Nanostructure Fabrication Using Electron Beam and Its Application to Nanometer Devices. *Proc. IEEE* **1997**, *85* (4), 629–643. https://doi.org/10.1109/5.573752.

(133) Nie, Z.; Kumacheva, E. Patterning Surfaces with Functional Polymers. *Nat. Mater.* **2008**, *7*, 277–290. https://doi.org/10.1038/nmat2109.

(134) Fukukawa, K.; Ueda, M. Recent Progress of Photosensitive Polyimides. *Polym. J.* **2008**, *40* (4), 281–296. https://doi.org/10.1295/polymj.pj2007178.

(135) Chiu, C. Y.; Lee, Y. C. Fabrication of Polyimide Micro/Nano-Structures Based on Contact-Transfer and Mask-Embedded Lithography. *J. Micromechanics Microengineering* **2009**, *19* (10). https://doi.org/10.1088/0960-1317/19/10/105001.

(136) Liaw, D. J.; Wang, K. L.; Huang, Y. C.; Lee, K. R.; Lai, J. Y.; Ha, C. S. Advanced Polyimide Materials: Syntheses, Physical Properties and Applications. *Prog. Polym. Sci.* **2012**, *37* (7), 907–974. https://doi.org/10.1016/j.progpolymsci.2012.02.005.

(137) Xu, C. L.; Wang, Y. Z. Durability, Anti-Corrosion and Self-Clean in Air/Oil of a Transparent Superhydrophobic Polyimide Film. *Appl. Mater. Today* **2018**, *10*, 18–23. https://doi.org/10.1016/j.apmt.2017.11.008.

(138)  Cosutchi, A. I.; Hulubei, C.; Dorohoi, D. O.; Neagu, M.; Ioan, S. Optical Surface Properties of Polyimides Cross-Linked Thin Film. *Rom. Reports Phys.* **2008**, *53* (5–6), 755–760.

(139)  Marchena, M.; Wagner, F.; Arliguie, T.; Zhu, B.; Johnson, B. .; Fernandez, M.; Chen, T. L.; Chang, T.; Lee, R.; Pruneri, V.; Mazumder, P. Dry Transfer of Graphene to Dielectrics and Flexible Substrates Using Polyimide as a Transparent and Stable Intermediate Layer. *2D Mater* **2018**, *5* (035022). https://doi.org/10.1088/2053-1583/aac12d.

(140)  Cho, J.-H.; Park, J.-H.; Lee, M.-H.; Song, H.-K.; Lee, S.-Y. A Polymer Electrolyte-Skinned Active Material Strategy toward High-Voltage Lithium Ion Batteries. A Polyimide-Coated LiNiO.0Mn1.5O4 Spnel Cathode Material Case. *Energy Environ. Sci.* **2012**, *5* (7124). https://doi.org/10.1039/C2EE03389E.

(141)  Zhang, J.; Shen, S.; Dong, X. X.; Chen, L. S. Low-Cost Fabrication of Large Area Sub- Wavelength Anti-Reflective Structures on Polymer Film Using a Soft PUA Mold. *Opt. Express* **2014**, *22*, 1842–1851. https://doi.org/10.1364/OE.22.001842.

(142)  Daglar, B.; Khudiyev, T.; Demirel, G. B.; Buyukserin, F. .; Bayindir, M. Soft Biomimetic Tapered Nanostructures for Large-Area Antireflective Surfaces and SERS Sensing. *J. Mater. Chem.* **2013**, *1* (7842–7848). https://doi.org/10.1039/C3TC31616E.

(143)  Ai, L.; Zhang, J.; Li, X.; Zhang, X.; Lu, Y.; Song, W. Universal Low-Temperature Process for Preparation of Multifunctional High-Performance Antireflective Mesoporous Silica Coatings on Transparent Polymeric Substrates. *ACS Appl. Mater. Interfaces* **2018**, *10* (4993). https://doi.org/10.1021/acsami.7b17584.